# Coherent Azimuth Ambiguity Removal from Along-Track Interferometric Synthetic Aperture Radar Data for the Harmony Mission

Scientific thesis to achieve the degree

Master of Science

at the Department of Electrical and Computer Engineering
of the Technical University of Munich.


| | |
|---|---|
| **Supervised by** | Dr. Marc Rodriguez-Cassola<br>DLR Microwaves and Radar Institute |
| **Examined by** | Dr.-Ing. Uwe Siart<br>TUM Chair of High-Frequency Engineering |
| **Submitted by** | Dominik Richter<br>Münchener Straße<br>82234 Weßling |
| **Date of submission** | 05.04.2022 |

# Contents

# Abbreviations

| | |
|---|---|
| **AASR** | azimuth-ambiguity-to-signal-ratio |
| **ATI** | along-track interferometry |
| **CASR** | complex azimuth-ambiguity-to-signal-ratio |
| **DCA** | Doppler centroid anomaly |
| **DFT** | discrete Fourier transform |
| **DRA** | dual receive antenna |
| **DPCA** | displaced phase center antenna |
| **MSE** | mean square error |
| **CRB** | Cramér-Rao bound |
| **IIR** | infinite impulse response |
| **IRF** | impulse response function |
| **LMMSE** | linear minimum mean square error |
| **ML** | maximum likelihood |
| **MUSIC** | multiple signal classification |
| **MVDR** | minimum variance distortionless response |
| **NESN** | noise equivalent sigma nought |
| **POSP** | principle of stationary phase |
| **SRTM** | shuttle radar topography mission |
| **TanDEM-X** | TerraSAR-X add-on for digital elevation measurement |
| **TOPS** | terrain observation by progressive scans |
| **PRF** | pulse repetition frequency |
| **RCM** | range cell migration |
| **RCS** | radar cross section |
| **SAR** | synthetic aperture radar |
| **SNR** | signal-to-noise-ratio |

# Abstract

Coherent azimuth ambiguities in interferometric synthetic aperture radar (InSAR) can be a major systematic error source if accompanied by a low suppression capability. They induce biases in the interferometric phase, which limits the achievable performance and hence, degrades the viability of remote sensing data for scientific usage.

This work derives, evaluates and compares algorithms to remove the effect of coherent azimuth ambiguities on 2- and 3-channel along-track interferometry (ATI). The interferometric performance is evaluated under the assumption of identically independently distributed data, which is simulated using a simplified one-dimensional (azimuth) InSAR channel model with coherent ambiguities. This linear time-invariant InSAR channel is further described analytically to ease the development of removal algorithms.

The InSAR channel configuration bases on the future Earth Explorer 10 "Harmony" mission, which exhibits a low azimuth ambiguity suppression capability. The mission goal is to observe ocean and sea surface currents to refine global Earth system models. To simulate ocean and sea surface scenes, a frozen multiplicative noise model is used, where parameters of interest are described from empirical data in different sea states.

One investigated algorithm on interferogram level (2 channels) minimizes the mean square error (MSE) of the interferometric estimate by means of a linear function of interferometric looks on the scene. The work derives this linear estimator from the previously found analytical channel model. It achieves removal of the effect of coherent azimuth ambiguities at a slight degradation of overall interferometric performance.

It is further compared, which improvement of the Cramér-Rao bound (CRB) is made by an additional third channel. Using this third channel, the suppression capability of two well-known algorithms from harmonic analysis are evaluated. Both algorithms — minimum variance distortionless response (MVDR), also known as Capon's beamformer, and multiple signal classification (MUSIC) — achieve suppression of the effect of coherent ambiguities, but, residual biases pose a limit on the minimum achievable performance.

# Zusammenfassung

Kohärente Ambiguitäten in Azimuth-Richtung können dominante Fehlerquellen in interferometrischem Synthetic Aperture Radar (InSAR) sein, falls das System keine ausreichend gute Unterdrückung dieser Ambiguitäten aufweist. Sie erzeugen einen systematischen Fehler in der gemessenen interferometrischen Phase, wodurch sich die erzielbare Performance des Systems und die Brauchbarkeit der Messungen für wissenschaftliche Zwecke verringert.

Diese Arbeit entwirft, bewertet und vergleicht Algorithmen zur Entfernung des Effekts von kohärenten Azimuth Ambiguitäten für along-track interferometrische (ATI) Systeme mit zwei und drei Kanälen. Die Bewertung erfolgt mit gleich verteilten, interferometrischen Daten eines vereinfachten Systemmodells. Zur Entwicklung der Algorithmen wird dieses lineare zeitinvariante Modell analytisch beschrieben.

Das zugrundeliegende Modell repräsentiert die zukünftige Earth Explorer 10 "Harmony" Mission, welche eine ungenügende Unterdrückung von Azimuth Ambiguitäten bietet. Mit dieser Mission sollen Ozean- und Meeresströmungen für die Verbesserung von Erdsystemmodellen gemessen werden. Die Ozean- und Meeresoberflächen werden mit einem eingefrorenen multiplikativen Rauschmodell simuliert, wobei die zu observierenden Parameter aus empirischen Daten stammen.

Ein entworfener Algorithmus entfernt Azimuth Ambiguitäten auf Interferogram-Ebene, durch Kombinierung von Interferogrammen unter Minimierung des mittleren quadratischen Fehlers. Dies entfernt Ambiguitäten bei leichter Verschlechterung der gesamten interferometrischen Performance.

Weiterhin wird untersucht, welche Verbesserung der Cramér-Rao Bound (CRB) ein dritter Kanal gegenüber zwei Kanälen bringt. Mehrere Kanäle ermöglichen den Einsatz von minimum variance distortionless response (MVDR) und multiple signal classification (MUSIC) zur Schätzung der interferometrischen Phase und Entfernung von Bias durch kohärente Ambiguitäten. Die Algorithmen erzielen eine Unterdrückung des Effekts, aber ein restlicher Bias limitiert die erreichbare minimale Performance.

# 1 Introduction

The hydrosphere of the Earth is a highly dynamic global system which works as heat reservoir for solar energy and as source of atmospheric moisture [Cra11, p. 1]. Each mechanism of storing, conveying and releasing energy needs to be fully understood to determine the overall influence on Earth's weather and climate [Doh10; Cra11]. Oceanographic and hydrological research depends on the observation, measurement and quantification of local phenomenons in the hydrosphere to refine global Earth system models and reduce their projection uncertainties [Rom20, p. 29].

With Seasat in 1978, the first space-borne mission dedicated to remote sensing of Earth's oceans was realized [Cra11; Pae20]. It carried a synthetic aperture radar (SAR), whose capabilities allowed to observe surfaces of large and remote areas — such as oceans — with only minor weather and sun depending limitations [Cra11, pp. 3–46]. Following missions continued to explore different techniques of SAR remote sensing. A few relevant for the purpose of this work are the shuttle radar topography mission (SRTM), which realized the first single-pass interferometric measurements from space, and the twin satellite formation of the TerraSAR-X add-on for digital elevation measurement (TanDEM-X) mission with, among others, an along-track interferometry (ATI) mode [Pae20]. First interferometric measurements where performed simply by comparing a time series of images from the same area [Bam98]. Single-pass interferometry gives the opportunity to measure surface deformations from the two-dimensional SAR images within one pass over the interrogated area, which mitigates inevitable atmospheric influences from ionosphere and troposphere during repeated passes [Que86]. For sensing the surface deformation of fast motions, i.e. ocean currents and waves, a very short interval between images is required [Pae20]. The single-pass ATI mode of TanDEM-X was the first space-borne mission to operate at very short time intervals, which allows the observation of such highly-dynamic motions via interferometry [Gol87; Pae20]. From the acquired measurement data by TanDEM-X it was shown, that ATI is the most accurate technique in comparison with Doppler centroid anomaly (DCA) and dual receive antenna (DRA) [Rom14; Lóp21].

Harmony — the future Earth Explorer 10 mission — will increase the capabilities of a Sentinel-1 satellite by formation flights as depicted schematically in Fig. 1.1 [Rom20]. During the mission, two identical and passive Harmony satellites will accompany the active Sentinel-1, forming a bistatic setup. The total mission phase divides into a stereo and an across-track phase. Only the stereo phase is further considered, because ATI will be performed during this phase to retrieve two-dimensional ocean and sea motion. The separation of Sentinel-1 and one Harmony satellite is designed such that the sensitivity to surface deformations using data from all three satellites is equal in north-south and east-west direction. The mission goal is to observe air-sea interactions, cyclones and ocean processes, from ocean surface motion measurements with an overall maximum estimation error of 20 $^{cm}/_{s}$ [Rom20, p. 39]. For comparison, Sentinel-1 achieves an accuracy of 29 $^{cm}/_{s}$ [ESA17].

Current evolution of future satellite SAR missions tends towards more, cheaper and smaller satellites [Pae20, pp. 13–23]. Their goals is to incorporate faster revisit times, more look angles and larger time series in one pass [Pae20]. Although, the Harmony satellites are not "so small", but they still share similar features of small satellites: Firstly, a formation flight that provides bistatic measurement data,

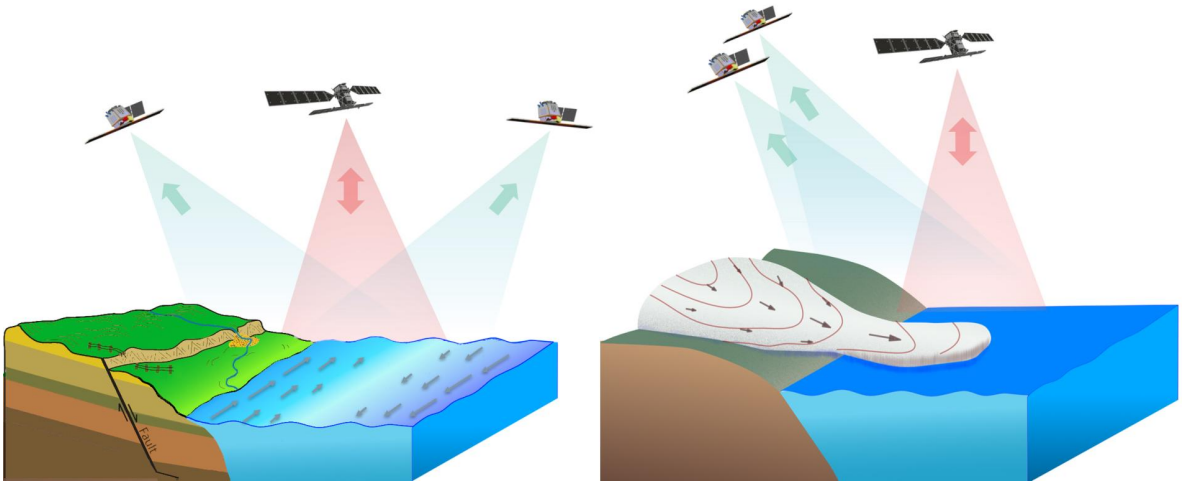


**Fig. 1.1:** Two passive Harmony satellites in stereo (left) and across-track (right) flight formation with an active Sentinel-1 satellite to observe small-scale motion and deformation of the Earth's surface, reprinted with permission: Harmony Mission Advisory Group, 2021.

secondly, a shrinking of antenna sizes, that results from a trade-off between ATI sensitivity, space limitations and mechanical feasibility [Rom20, p. 50]. Each Harmony satellite will carry three antennas, where data acquired by all three antennas may be used for performing ATI. The current antenna designs are smaller, i.e., compared to the antenna on Sentinel-1, which has a length in azimuth of about 12 m and the largest antenna on Harmony is designed to have a length in azimuth of about 4 m [Rom20, pp. 57–59]. The antenna however, is a vital part of a SAR system, because its antenna pattern works as an anti-aliasing filter of Doppler frequencies [Li83]. It was shown, aliases — also called azimuth ambiguities — will bias the measurements if they are coherent [Vil12]. Coherent azimuth ambiguities behave just as the true not-aliased data, resulting in an unwanted focusing and correlation between images and finally a systematic error. The coherent condition for ambiguities holds in the case of the Harmony mission and the effect of biasing by those aliases must be considered [Zon22]. To achieve the required accuracy for scientific usage of the measurements, the effect of those biases must be mitigated [Zon22]. Unlike random errors from non-coherent thermal noise, biases can not be reduced by performing averaging, i.e. multi-look processing or boxcar-averaging [Por76; Tou94]. Hence, other algorithms are necessary to remove the systematic error and to fulfill the scientific requirements of the Harmony mission.

The main goal of this thesis is the development and evaluation of algorithms to remove the effect of biases by coherent azimuth ambiguities for ATI systems. However, the algorithms are not constrained to solely ATI systems. A use-case of those algorithms is the Harmony mission [Rom20], which defines the overall SAR geometry and system parameters used during this work. The mission will not only provide a single interferogram (2 channels), but up to three independent channels. Prospective algorithms must be phase-preserving and may leverage multiple channels, but only three channels are relevant for performance assessment. As part of the Phase-0/A system study of the mission, the analysis and verification of the developed algorithms contributes to the assessment of interferometric performance of the whole system.

Within this work, only the stripmap SAR scanning mode with fixed antenna pointing direction is considered. However, the Harmony mission requires algorithms to work also on other scanning modes, especially those, which enable wider swaths as ScanSAR or terrain observation by progressive scans (TOPS) [Rom20]. During the work, those modes are referenced but not explained in detail. Further readings on SAR scanning modes may be found in the literature [Cum05; De 06].

## 1.1 Review of Literature on Azimuth Ambiguity Suppression and Removal

Azimuth ambiguities — or in general ambiguities — have been perceived much consideration with respect to image quality, i.e. increased noise level or "ghosts signatures" of strong targets [Bay75; Li83; Ran87; Mor93]. I.e., ship detection must deal with ghosts, which are clearly visible on the low scattering sea clutter. Ghost suppression algorithms usually benefit from the point-like highly reflective metallic structures on ships [Vel14], which are not applicable to ocean and sea surface scattering measurements.

Minimizing the noise level contribution of *incoherent* azimuth ambiguities is usually considered in the system design process [Wol17]. The Harmony mission faces several constraints, i.e. pulse repetition frequency (PRF), transmit antenna size and antenna pattern shape or orbit height, which are defined by the Sentinel-1 satellite [Rom20]. Furthermore, such system design approaches are only reducing the effect of biases, but are not completely removing them. Note, the different usage of *suppression* and *removal* in the scope of this work, where the former describes a reduction and the latter a complete removal of coherent ambiguity biases.

Phase preserving algorithms may use a transfer function to suppress the effect of ambiguities. For instance, a de-convolving transfer function may be applied [Mor93]. This processing scheme requires the ambiguous frequencies to be correlated with the main signal frequencies, which is only fulfilled for point-like scatterers. The algorithm fails for fully developed speckle, observed usually on oceans, seas and lakes, because there exists no inter-frequency correlation that can be leveraged [Mor93; Mon05].

A different approach for distributed targets and scenes evaluates the eigenvalue spectrum entropy in the Doppler spectrum to identify and mask Doppler frequencies, that are predominantly disturbed by ambiguities [Liu19]. By neglecting such frequencies, the power of ambiguities is reduced, but also useful energy from the true signal is discarded. One could have leveraged this power to improve measurement accuracy. A similar technique uses an adaptive Wiener filter to de-emphasize frequencies containing high aliased power [Mon05]. Both algorithms minimize the ambiguous energy within the image, but this still yields biases in presence of coherent azimuth ambiguities, because ambiguities have neither been de-correlated nor biases have been considered in the algorithm formulation.

The first algorithm to consider and remove biases is the infinite impulse response (IIR) equalizer, which is also the first algorithm to be applied on interferogram level [López19a]. Biases can on average be removed by recursively subtracting weighted and shifted versions of the interferogram from itself. In simplified terms, the weights are complex factors that denote the ratio of ambiguity to main signal in the interferogram [López19a]. If those weights are not precisely known, then residual biases will remain. It is shown in this work, that these weights are varying over the imaged swath. Hence, the algorithm needs to estimate the weights as well [López19a]. The shifts of ambiguities are a well-known value [Ran87], but introduce further dependencies on the algorithm. To remove biases completely, it is required that ambiguities and main signal have identical interferometric properties, i.e. expected values. However, the imaged scene is highly-dynamic and the interferometric signature changes over time.

The scene might be accelerating during overflight, i.e. inherent orbital movement of particles in waves[1] [Has85] or air-sea interactions [Has85; War13]. Additional changes of interferometric properties occur inherently, because of breaking waves or a generally finite coherence time. Coherence time is defined from the width of auto-correlation function of the scattered signal over time and is limited due to the random-like movement of capillary waves on the surface [Car94]. Capillary waves introduce surface roughness, which form a main contribution to the radar scattering coefficient [Has85; War13]. Beyond coherence time of the surface, the scattering contribution has changed significantly and identical interferometric properties may not be assumed. Measurements at L-band (1248.75 MHz) showed a coherence time of 60 ms to 210 ms for ocean and sea surfaces [Car94; She93]. The IIR equalizer requires the interferometric scene to be stable and coherent also beyond one synthetic aperture time of 158 ms, because ambiguities are delayed due to the physical shifts of each ambiguity. The delay per ambiguity in the Harmony mission is 678 ms, which exceeds those common coherence times. The effect of scene dynamics was not yet analyzed, because it requires real data to show the effect [Lóp19a]. In this work, possible algorithms are restricted to data measured in one synthetic aperture time and information form the ambiguous positions are neglect. The influence of scene dynamics are hereby reduced to an unavoidable minimum.

## 1.2 Outline

This work starts with reviewing the imaging theory of SAR in Chapter 2, which leads to a simulation model for one-dimensional bistatic interferometric data with coherent ambiguities. Furthermore, expressions for the system sensitivity with respect to surface velocities and for the ratio of coherent ambiguity to signal on interferogram level are derived. The simulation model and the interferometric metrics form the basis of the following chapters.

The Chapter 3 describes the applied method for evaluation of the interferometric performance using the simulation model from Chapter 2 and prior assumptions on the quantities to be measured. It concludes by analyzing and verifying the simulation model with respect to the theoretical effect of coherent azimuth ambiguities.

In Chapter 4 and 5, different algorithms on interferogram level (2 channels) and with multiple channels (> 2) are derived, respectively. The algorithm performance is analyzed and compared to the IIR equalizer as well as the unbiased optimum lower estimation bound, called Cramér-Rao bound (CRB). This requires knowledge of the CRB for multi-channel interferometry, which is analytically derived beforehand from a multi-variate circular complex Gaussian data model. The algorithms are applied to simulated data using the model from Chapter 2.

The closing Chapter 6 compares the results obtained for each algorithm from Chapter 4 and 5. Finally, a conclusion is drawn and an outlook on future research and development steps is given.

1 A helpful visualization of orbital particle motion in waves might be found online: https://rwu.pressbooks.pub/webboceanography/chapter/10-1-wave-basics/

# 2 Theory of SAR and Interferometry

SAR is a coherent radar system, that leverages the Doppler effect and high bandwidth pulses to obtain reflectivity and distance information from large areas with a high resolution [Cum05]. An exemplary drawing of a simplified rectilinear SAR acquisition geometry shows Fig. 2.1. A space- or aircraft is moving along its track in $x$-direction, therefore called along-track or azimuth coordinate, and interrogates the scene using high bandwidth pulses and its broadside looking antenna. The range or cross-track direction $R$ denotes the distance from antenna to scene. The received high bandwidth pulses are compressed to achieve high resolution in the range direction. Additionally, the recorded coherent (compressed) pulses might be focused in azimuth or along-track direction to form a large synthetic aperture and achieve high resolution in the second image dimension as well. A more detailed introduction to the concepts of compression, focusing and high resolution may be found in the literature [Cum05, pp. 113–155][Tom78; Bam98].

This chapter summarizes the basics required to simulate a simple one-dimensional azimuth SAR channel. The simple model is then adapted to describe multi-channel bistatic SAR systems and acquisition of interferometric data. It also introduces the sensitivity of ATI with respect to surface motion. Each section depends on the acquisition geometry and satellite design, which is now introduced.

## 2.1 Simplified Rectilinear Geometry of Harmony Mission

ATI is performed on data acquired with Harmony satellites in stereo configuration with a Sentinel-1 [Tor17] satellite [Lóp19b], visualized in Fig. 1.1. This work focuses on one bistatic configuration, i.e. Sentinel-1 and Harmony in aft position as schematically depicted in Fig. 2.1. The separation of Sentinel-1 and each Harmony satellite denotes $x_0$, and is in the order of 350 km [Rom20, p. 34]. A rectilinear geometry is used to simplify the modeling procedures, but actually, the satellites will orbit in a height of about 700 km above nadir around Earth.

The actual curved geometry makes simulation of SAR data for evaluation of the interferometric performance unnecessarily complicated and is therefore neglected. The same holds for Earth's curvature and rotation. A detailed description of the real geometry can be found in literature [Cum05, pp. 120–129] [Tom78]. The rectilinear geometry infers that velocity of satellites $v_{\mathrm{Sat}}$ and velocity of the beam on ground $v_{\mathrm{Gr}}$ are equal. In an orbital geometry, $v_{\mathrm{Gr}}$ is smaller than $v_{\mathrm{Sat}}$, because the angular velocity of the orbiting satellite is constant and the Earth's radius is smaller than the orbit radius. This has an influence on the observed Doppler shift in real scenarios [Cum05, p. 126]. Hence, all calculations of Doppler shift within this work only hold for the presented rectilinear geometry.

The current satellite design of one of the Harmony companions proposes an antenna configuration as shown in Fig. 2.2 [Rom20, p. 58]. It consists of two main antennas in fore and aft direction and a smaller middle antenna. With all three antennas being smaller in azimuthal length than the transmitting antenna on Sentinel-1. The figure further shows the phase centers of the antennas with their inter-antenna spacing, called the physical along-track baseline $B_{\mathrm{ATI},ij}$.

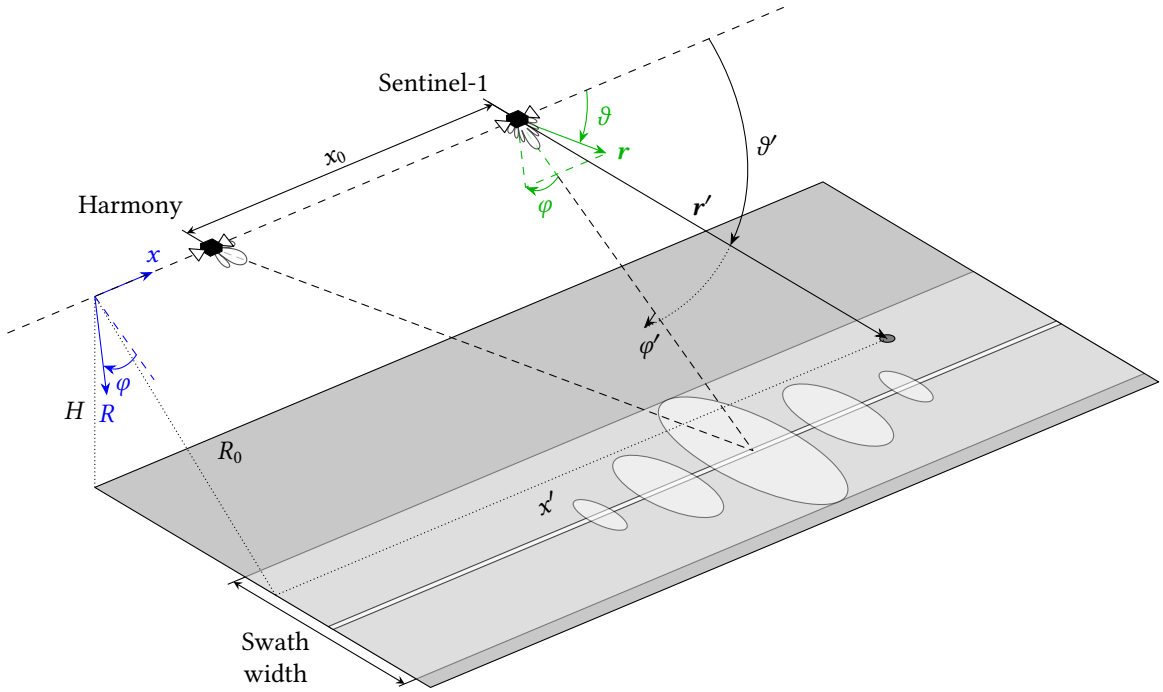


**Fig. 2.1:** Simplified SAR geometry for a point target as used in the Harmony mission. A local spherical coordinate system (green) and a global cylindrical SAR coordinate system (blue) are used. The footprint on ground is only given for antenna onboard of Sentinel-1.

The observed Doppler shift with fore and aft antenna for a point target

$$f_{\mathrm{D},1}(t, x_0) = -\frac{1}{\lambda}\frac{\mathrm{d}}{\mathrm{d}t}\left(r'^{(\mathrm{S})} + r'^{(\mathrm{H})}\right) \tag{2.1}$$

$$f_{\mathrm{D},3}(t, x_0 + B_{\mathrm{ATI},13})\,, \tag{2.2}$$

where $r'^{(\mathrm{S})}$ and $r'^{(\mathrm{H})}$ denote distances between satellite phase centers and point target, is illustrated in Fig. 2.3. The point target is maximally illuminated by Sentinel-1 at time $t = 0\,\mathrm{s}$. Due to the squinted observation from the Harmony satellite, this point target is perceived with a so called Doppler centroid $f_{\mathrm{DC},1} = f_{\mathrm{D},1}(t = 0\,\mathrm{s}, x_0)$ of 52.605 kHz, whereas the Doppler centroid for the monostatic SAR acquisition of Sentinel-1 is 0 Hz. Between the fore and aft channel there is a small delay in the Doppler frequency history visible. This delay results from the physical separation of the antennas and determines the sensitivity of the ATI system to surface motion.

## 2.2 Sensitivity of Along-Track Interferometry

The sensitivity of an interferometric system is a necessary metric to relate the measured interferometric phase to the observed physical quantity of surface displacement or motion. To avoid systematic errors on inverting the interferometric phase, a detailed analysis of the sensitivity of the Harmony mission in stereo formation is conducted. In ATI, the sensitivity depends on the time difference (baseline) that separates two consecutive acquisitions [Gol87]. Given the Doppler history of both channels, i.e.

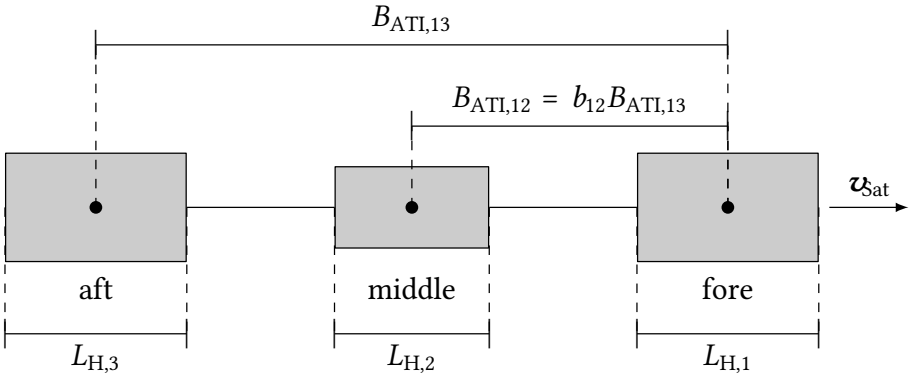


**Fig. 2.2:** Schematic drawing of antenna configuration onboard of one of the Harmony satellites with measures.

in Fig. 2.3, one finds the delay as time difference between equal Doppler frequencies. One must use equal Doppler frequencies to have a common spectral support for both acquisitions. Otherwise, the acquired data for interferometric processing of distributed targets looses coherence and interferometric performance, i.e., compare [Gat94]. Using a local linearization of the Doppler frequency history of the second channel at the time of processed Doppler centroid $t_{\mathrm{S}}$, the time difference is approximately

$$\Delta t \approx \frac{\Delta f_{\mathrm{D}}}{\left.\frac{\partial f_{\mathrm{D},3}(t)}{\partial t}\right|_{t=t_{\mathrm{S}}}} = \frac{f_{\mathrm{DC}} - f_{\mathrm{D},3}(t_{\mathrm{S}})}{\left.\frac{\partial f_{\mathrm{D},3}(t)}{\partial t}\right|_{t=t_{\mathrm{S}}}} . \tag{2.3}$$

With a difference in Doppler frequency $\Delta f_{\mathrm{D}}$ of −1.285 Hz and a Doppler rate on channel 3 of −2212.01 $^{\mathrm{Hz}}/_{\mathrm{s}}$, which is the sum of the Doppler rate by Sentinel-1 at $t = 0$ s and by channel 3 at $t = -x_0/v_{\mathrm{Sat}}$ taken from Fig. 2.4, one may expect a delay of 580.92 µs. This time delay is less than the delay of 657.89 µs as discussed in the literature [Gol87]. The loss of sensitivity by a factor of 0.883 occurs due to the highly squinted bistatic geometry and is analyzed in this section.

The stereo Harmony setup measures the surface velocity with the fore and aft companion satellite under different viewing angles, which allows to infer the two-dimensional component of the surface velocity [Lóp19b]. This work considers only one companion satellite, i.e. trailing (aft) Harmony, which measures the surface velocity projected into the plane spanned by Sentinel-1, Harmony and the target using (short) ATI [Gol87]. ATI uses the phase difference of two temporally delayed complex SAR images to find the displacement of scatterers during this time interval. The phase of each image sample is given by the total propagation delay between transmitter and receiver and the phase of the target. The phase of the target is common to both images and therefore removed during interferometric combination [Bam98]. The propagation delay depends on the distance between Sentinel-1's and Harmony's phase centers and the target

$$r\left(x', x, x_0, R_0\right) = r'^{(\mathrm{S})} + r'^{(\mathrm{H})} = \sqrt{(x' - x)^2 + R_0^2} + \sqrt{(x_0 - x + x')^2 + R_0^2}\,, \tag{2.4}$$

where $x'$ is the position of a point scatterer, $x$ denotes the position of Sentinel-1 and $R_0$ the distance in range of the scatterer.

The projected surface velocity is split into two orthogonal components along azimuth and along range to find the sensitivity per component and later for the total velocity vector. The analysis starts

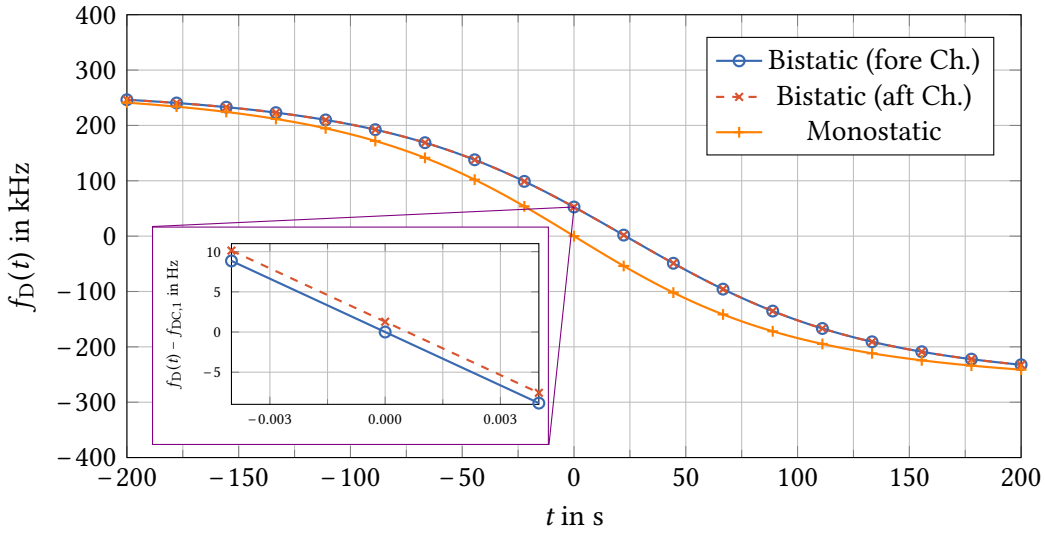


**Fig. 2.3:** Instantaneous Doppler frequency received at trailing Harmony satellite from point target, Sentinel-1 has shortest distance to point target at $t_S = 0.0\,\text{s}$, Harmony satellite has shortest distance to point target at $t_H = 46.1\,\text{s}$, zero Doppler frequency is seen at $(t_S + t_H)/2 = 23.03\,\text{s}$. Harmony operates in a highly squinted configuration, with a Doppler centroid of 52.605 kHz. Monostatic curve shows Doppler frequency as perceived solely by Sentinel-1.

with the velocity component in range, where the range coordinate is defined by the global coordinate system as shown in Fig. 2.1. For the first Harmony antenna, the distance to a point target positioned at $x' = 0\,\text{m}$ is

$$r_1(0, v_{\text{Sat}}t, x_0, R_0 + v_r t)\,, \tag{2.5}$$

where $v_r$ denotes the radial velocity of the point target. The third antenna on Harmony, which forms channel 3, has a distance

$$r_3(0, v_{\text{Sat}}t, x_0 + B_{\text{ATI},13}, R_0 + v_r t) \tag{2.6}$$

to the same point target. Image 1 is processed around the Doppler centroid received at $t = 0\,\text{s}$. Image 3 acquired on channel 3 is also processed around the Doppler centroid of image 1, such that both images possess the same spectral bandwidth. The third channel receives the Doppler centroid of image 1 after a time delay $\Delta t$

$$f_D\left(-\frac{x_0 + B_{\text{ATI},13}}{2v_{\text{Sat}}} + \Delta t, x_0 + B_{\text{ATI},13}\right) = f_{DC,1} = f_D\left(-\frac{x_0}{2v_{\text{Sat}}}, x_0\right), \tag{2.7}$$

which is solved numerically using the analytical expression for instantaneous Doppler frequency (2.36) and the Newton-Raphson method. A large separation $x_0$ causes different Doppler rates with respect to transmission by Sentinel-1 and reception by Harmony. Fig. 2.4 illustrates the difference in Doppler frequency $\Delta f_D$, which must be overcome by the aft channel. Transmission contributes with $\Delta f_{D,S}$ to the reduction of $\Delta f_D$. This contribution is larger than the contribution from reception due to the different Doppler rates, which yields a decrease of $\Delta t$. This effect is later combined into a sensitivity loss factor.

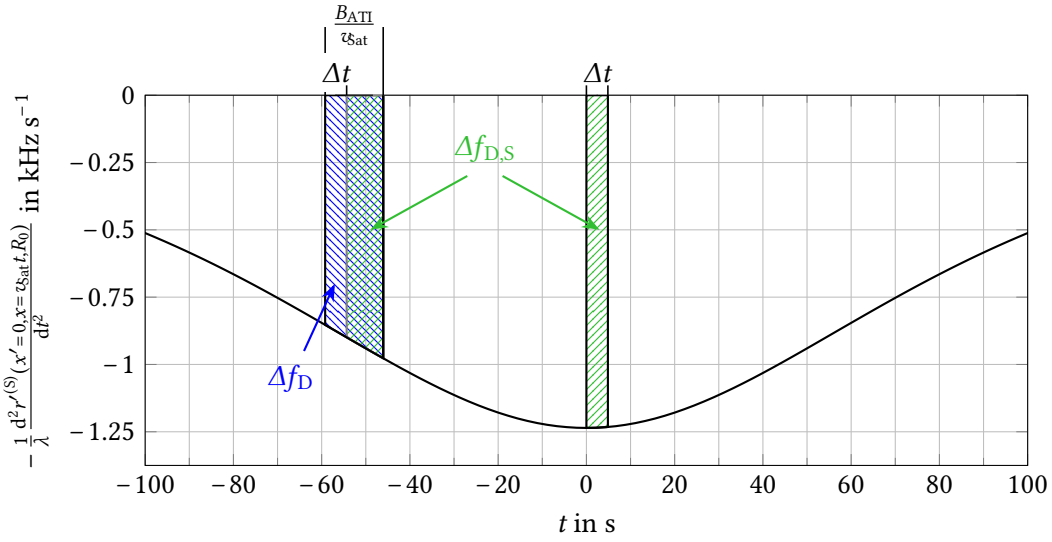


**Fig. 2.4:** Single way Doppler frequency rate and geometric interpretation of time delay between acquisitions and the Doppler loss factor. For demonstrative purposes, a bistatic geometry with $x_0 = 350\,\mathrm{km}$ and $B_{\mathrm{ATI}} = 100\,\mathrm{km}$ is used.

The phase difference or interferometric phase of the point target between the images is then given by the difference in electrical distance

$$\Delta\phi = \frac{2\pi}{\lambda}\Big[r_3(t=\Delta t) - r_1(t=0)\Big] = \frac{2\pi}{\lambda}\Big[\sqrt{v_{\mathrm{Sat}}^2\Delta t^2 + (R_0 + v_{\mathrm{r}}\Delta t)^2} + \sqrt{\big(x_0 + B_{\mathrm{ATI},13} - v_{\mathrm{Sat}}\Delta t\big)^2 + (R_0 + v_{\mathrm{r}}\Delta t)^2} - R_0 - \sqrt{x_0^2 + R_0^2}\Big] \tag{2.8}$$

and the phase sensitivity

$$\frac{\partial\Delta\phi}{\partial v_{\mathrm{r}}} = \frac{2\pi}{\lambda}\left(\frac{\Delta t(R_0 + r_{\mathrm{r}}\Delta t)}{\sqrt{v_{\mathrm{Sat}}^2\Delta t^2 + (R_0 + v_{\mathrm{r}}\Delta t)^2}} + \frac{\Delta t(R_0 + r_{\mathrm{r}}\Delta t)}{\sqrt{(x_0 + B_{\mathrm{ATI},13} - v_{\mathrm{Sat}}\Delta t)^2 + (R_0 + v_{\mathrm{r}}\Delta t)^2}}\right) \tag{2.9}$$

is approximately

$$\frac{\partial\Delta\phi}{\partial v_{\mathrm{r}}} \approx \frac{2\pi}{\lambda}\Delta t R_0\left(\frac{1}{R_0} + \frac{1}{\sqrt{x_0^2 + R_0^2}}\right) = \frac{2\pi}{\lambda}\Delta t\left(1 + \sqrt{\frac{R_0^2}{x_0^2 + R_0^2}}\right). \tag{2.10}$$

One sees, that the well known sensitivity of an ATI system [Gol87; Wol17; Lóp19a]

$$\frac{\partial\Delta\phi}{\partial v_{\mathrm{proj,surf}}} = \frac{2\pi B_{\mathrm{ATI},13}}{\lambda}\frac{1}{v_{\mathrm{Sat}}} \tag{2.11}$$

degrades for increasing separations $x_0$ due to two factors. Firstly, a geometrical loss factor

$$L_{\mathrm{g,r}} = \frac{1 + \sqrt{\frac{R_0^2}{x_0^2 + R_0^2}}}{2}, \tag{2.12}$$

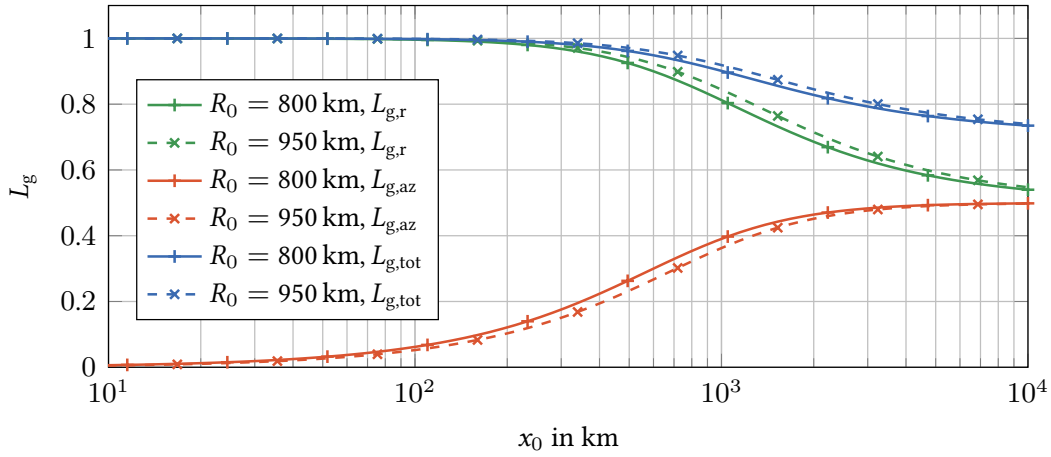


(a) Geometrical loss factor $L_g$

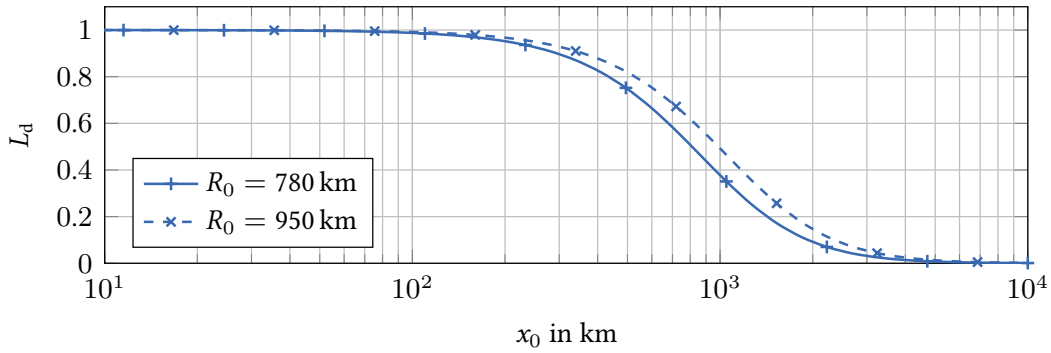


(b) Doppler frequency loss factor $L_d$

**Fig. 2.5:** Sensitivity geometrical loss factor $L_g$ and Doppler frequency loss factor $L_d$ over Sentinel-1 and Harmony separation for near and far ranges.

which is related to viewing angles of the Harmony satellite on the radial velocity component, depicted in Fig. 2.5 (a). For very large separations $x_0$, the sensitivity reduces to half of the maximum sensitivity, where only the broadside looking Sentinel-1 [Tor17] has a contribution to radial sensitivity. Secondly, a Doppler frequency related loss factor

$$L_d = \frac{\Delta t}{\max\{\Delta t\}} = \frac{\Delta t}{\frac{B_{ATI,13}}{2v_{Sat}}}, \tag{2.13}$$

which relates to different Doppler rates per channel due to the highly squinted bistatic geometry. This factor is shown in Fig. 2.5 (b).

The sensitivity for an azimuth velocity component is found similarly as done for the range component. The azimuth velocity component induces a shift of the point target in azimuth, due to an additional Doppler component from the target. This shift is small and is neglected, because the satellite velocity is several magnitudes larger than the maximum expected surface velocity. The phase difference shows a sensitivity with respect to an azimuth movement of the target $x = v_{az}t$, which is

approximately

$$\frac{\partial \Delta\phi}{\partial v_{\mathrm{az}}} \approx \frac{2\pi}{\lambda} \Delta t \sqrt{\frac{x_0^2}{x_0^2 + R_0^2}} = \frac{2\pi B_{\mathrm{ATI,13}}}{\lambda} \frac{1}{v_{\mathrm{Sat}}} L_{\mathrm{d}} L_{\mathrm{g,az}} \,, \tag{2.14}$$

where

$$L_{\mathrm{g,az}} = \frac{1}{2} \sqrt{\frac{x_0^2}{x_0^2 + R_0^2}} \,. \tag{2.15}$$

The sensitivity depends again on the same Doppler loss factor, which reduces the temporal delay between the acquisitions on channel 1 and 3. However, the geometrical loss factor is different for the azimuth velocity component, as depicted in Fig. 2.5 (a). An ATI system with a small separation of transmitter and receiver, i.e. TanDEM-X mission, has no sensitivity to the parallel azimuth velocity component. With the Harmony mission, a sensitivity in both azimuth and range velocity component is achieved. Using a fore and aft companion satellite allows then the inversion of interferometric phases to a two-dimensional velocity component. The maximum total sensitivity is defined by the magnitude of the gradient of the phase difference with respect to the two orthogonal velocity components

$$S_{\mathrm{ATI}} = \frac{\Delta\phi}{v_{\mathrm{proj,surf}}} = \sqrt{\left(\frac{\partial \Delta\phi}{\partial v_{\mathrm{r}}}\right)^2 + \left(\frac{\partial \Delta\phi}{\partial v_{\mathrm{az}}}\right)^2} = \frac{2\pi B_{\mathrm{ATI,13}}}{\lambda} \frac{1}{v_{\mathrm{Sat}}} L_{\mathrm{d}} L_{\mathrm{g,tot}} \,, \tag{2.16}$$

where

$$L_{\mathrm{g,tot}} = \sqrt{L_{\mathrm{g,r}}^2 + L_{\mathrm{g,az}}^2} = \sqrt{\frac{1}{2} + \frac{1}{2} \sqrt{\frac{R_0^2}{x_0^2 + R_0^2}}} \,. \tag{2.17}$$

For the Harmony mission, a separation of Sentinel-1 and Harmony of about 350 km [Rom20; Lóp19b] is desired, which yields negligible losses of total sensitivity $L_{\mathrm{g,tot}}$ by the observation geometry as shown in Fig. 2.5 (a). Hence, the interferometric signatures of surface velocities are not weakened by the geometrical loss and may be neglected in the performance evaluation later on. A disadvantage is the non-symmetrical sensitivity for azimuth and range components, which must be considered when inverting the interferometric phases. This will not be further investigated.

Fig. 2.5 also shows the dependency of both loss factors for the near and far slant ranges $R_0$, with the Doppler frequency loss factor decreasing already for lower separations in the near range case. Highly accurate ATI measurements need to consider this dependency.

A SAR system can not only observe and deal with isolated point-like scattering behavior as considered in the previous section, but its processing techniques make it suitable for complex and extensive scenes. Nonetheless, the sensitivity analysis remains valid [Gol87].

## 2.3 Imaging with a Single SAR Channel

This section describes the well-known SAR imaging principle for a single channel. The description is confined to only one line of data with constant range — a range line —, as it is implied in Fig. 2.1. More channels are later added to perform interferometric measurements, where each channel acquires

data as described in this section. Firstly, the impulse response of a single point target observed with mono- and bistatic channels is derived by describing the underlying physics of transmission, scattering and receiving of electromagnetic waves. This response might be interpreted as an impulse response function (IRF) for frozen or non-moving scenes [Has85; Bam98; Tom78] and it is interesting to know its Fourier transform, which is derived afterwards. Then, the IRF is applied to distributed frozen ocean scenes and a simulation procedure for raw SAR data is described. Following this, the noise contribution on the raw data is quantified. Finally, the SAR image is generated by focusing the raw data.

During the whole work, imaging is done only in stripmap mode, where the pointing of antennas remains fixed. Furthermore, a start-stop assumption is made and pulse travel times are neglected to simplify the mathematical description [Cum05, pp. 167].

### 2.3.1 Monostatic Impulse Response Function

A SAR channel depends on a variety of system parameters, i.e. antenna size, center frequency $f_\mathrm{T}$ of transmission and transmitted power. Within this section, the channel is described using simplified electromagnetic relations from antenna and wave propagation theory. During the derivation for a monostatic channel, a distinction between the transmitting and receiving case is made to distinguish their contributions, that allows an easier adaption to the bistatic channel later on.

In the Harmony mission case, only Sentinel-1 uses a monostatic SAR channel, see Fig. 2.1. The antenna onboard of Sentinel-1 transmits a time harmonic electromagnetic wave (time convention $\exp\{-\mathrm{j}2\pi f_\mathrm{T} t\}$ is used) in broadside direction towards the region of interest. The total electric field strength in the far-field region of the antenna along an arbitrary unit vector is then given by [Bal16, p. 773]

$$\boldsymbol{E} = \hat{\boldsymbol{e}}_\mathrm{E} E_\mathrm{max} C_\mathrm{Tx}(\vartheta, \varphi) r_0 \frac{\mathrm{e}^{-\mathrm{j}k_0 r}}{r} \mathrm{e}^{\mathrm{j}\psi_\mathrm{Tx}(\vartheta,\varphi)}, \tag{2.18}$$

where $k_0 = 2\pi/\lambda = 2\pi f_\mathrm{T}/c_0$ is the free space wavenumber and $c_0$ the speed of light, $\left|C_\mathrm{Tx}(\vartheta, \varphi)\right|$ denotes the transmitting antenna pattern and $\psi_\mathrm{Tx}(\vartheta, \varphi)$ defines the phase variation of the electric field on a sphere centered at the position of the transmitting antenna. By energy conservation, the maximum electric field amplitude $|E_\mathrm{max}|$ at a radius of $r_0$ is related to the radiated power

$$P_\mathrm{rad} = \int_{-\pi}^{\pi} \int_{0}^{\pi} \left|E_\mathrm{max} C_\mathrm{Tx}(\vartheta, \varphi)\right|^2 \frac{r_0^2}{2 Z_\mathrm{F0} r^2} r^2 \sin\vartheta \,\mathrm{d}\vartheta \,\mathrm{d}\varphi = \frac{2\pi |E_\mathrm{max}|^2 r_0^2}{D_\mathrm{Tx} Z_\mathrm{F0}}, \tag{2.19}$$

using the antenna directivity $D_\mathrm{Tx} = 4\pi / \iint \left|C_\mathrm{Tx}(\vartheta, \varphi)\right|^2 \sin\vartheta \,\mathrm{d}\vartheta \,\mathrm{d}\varphi$ [Bal16, p. 47]. Using a normalized wave amplitude $a_\mathrm{Tx} = \sqrt{2P_\mathrm{rad}/\eta_\mathrm{Tx}}$ with unit $[a_\mathrm{Tx}] = \sqrt{\mathrm{W}}$ to denote the transmitted electromagnetic wave at the local antenna port, one finds the free space electric field

$$\boldsymbol{E} = a_\mathrm{Tx} \sqrt{\frac{G_\mathrm{Tx} Z_\mathrm{F0}}{4\pi}} \left|C_\mathrm{Tx}(\vartheta, \varphi)\right| \mathrm{e}^{\mathrm{j}\psi_\mathrm{Tx}(\vartheta,\varphi)} \frac{\mathrm{e}^{-\mathrm{j}k_0 r}}{r} \hat{\boldsymbol{e}}_\mathrm{E}, \tag{2.20}$$

where IEEE gain $G_\mathrm{Tx} = \eta_\mathrm{Tx} D_\mathrm{Tx}$ was introduced, depending on the local excitation.

A point target is located at coordinates $(r', \vartheta', \varphi')^\mathrm{T}$, where $(\cdot)^\mathrm{T}$ denotes the matrix transpose, with respect to the spherical coordinate system of the antenna (highlighted in green in Fig. 2.1). The

electromagnetic wave is scattered from this point target towards a receiving antenna. In the monostatic case, the scattered electric field at the position of the phase center of the antenna is

$$\boldsymbol{E}_{\mathrm{sc}} = \frac{\Gamma}{\sqrt{4\pi}} \mathrm{e}^{\mathrm{j}\psi_{\mathrm{Rx}}(\vartheta',\varphi')} \frac{\mathrm{e}^{-\mathrm{j}k_0 r'}}{r'} \hat{\boldsymbol{e}}_{\mathrm{sc}} \|\boldsymbol{E}\| \, r_0' \,, \tag{2.21}$$

where $\Gamma = \sqrt{\sigma^0}\mathrm{e}^{\mathrm{j}\phi_{\mathrm{PT}}}$ denotes a complex reflection coefficient which is related to the scattering coefficient $\sigma^0$ of the target via its backscattered power

$$P_{\mathrm{sc}} = \int_{-\pi}^{\pi} \int_{0}^{\pi} \frac{\|\Gamma \boldsymbol{E}\|^2}{4\pi} \frac{r_0'^2}{2Z_{\mathrm{F0}} r^2} r^2 \sin\vartheta \, \mathrm{d}\vartheta \, \mathrm{d}\varphi = \frac{\sigma^0 \|\boldsymbol{E}\|^2 \, r_0'^2}{2Z_{\mathrm{F0}}} \,. \tag{2.22}$$

The scattering coefficient — also called radar cross section (RCS) — relates scattered power $P_{\mathrm{sc}}$ and incident power density $\|\boldsymbol{E}\|^2 / 2Z_{\mathrm{F0}}$, such that energy conservation between a target with physical extension and the virtual point target holds [War13, p. 454].

Using the reciprocity theorem and the effective area $A_{\mathrm{eff}} = G_{\mathrm{Rx}} \left| C_{\mathrm{Rx}}(\vartheta, \varphi) \right|^2 \lambda^2 / (4\pi)$ of the receiving antenna one finds the received normalized wave amplitude without polarization loss

$$b_{\mathrm{Rx}} = \sqrt{\frac{A_{\mathrm{eff}}}{Z_{\mathrm{F0}}}} \hat{\boldsymbol{e}}_{\mathrm{sc}} \cdot \boldsymbol{E}_{\mathrm{sc}} = a_{\mathrm{Tx}} \frac{\sqrt{G_{\mathrm{Tx}} G_{\mathrm{Rx}}} \left| C_{\mathrm{Tx}}(\vartheta', \varphi') C_{\mathrm{Rx}}(\vartheta', \varphi') \right| \lambda}{\sqrt{4\pi^3} r'^2} \Gamma \mathrm{e}^{\mathrm{j}\left[\psi_{\mathrm{Tx}}(\vartheta',\varphi') + \psi_{\mathrm{Rx}}(\vartheta',\varphi')\right]} \mathrm{e}^{-\mathrm{j}2kr'} \,. \tag{2.23}$$

For

$$P_{\mathrm{Rx}} = \frac{1}{2} |b_{\mathrm{Rx}}|^2 = P_{\mathrm{Tx}} \frac{\left( \sqrt{G_{\mathrm{Tx}} G_{\mathrm{Rx}}} \left| C_{\mathrm{Tx}}(\vartheta', \varphi') C_{\mathrm{Rx}}(\vartheta', \varphi') \right| \right)^2 \lambda^2}{(4\pi)^3 r'^4} \sigma^0 \,, \tag{2.24}$$

one finds the power relation as stated by the radar range equation.

Previous descriptions have been made with respect to a local antenna coordinate system. Now, a change to a global coordinate system is conducted, which eases the description of the imaging process. As the antenna moves together with the spacecraft, also the coordinates of the point targets change depending on the position of the spacecraft. In the following, a global cylindrical coordinate system (highlighted in blue in Fig. 2.1) is utilized. The position of the antenna is $\boldsymbol{r} = (R, \varphi, x)^{\mathrm{T}}$ and the point target is located at $\boldsymbol{r}' = (R', \varphi', x')^{\mathrm{T}}$. Using this coordinate system, one finds a transformation

$$r' = \sqrt{R'^2 + (x' - x)^2} \tag{2.25}$$

$$\vartheta' = \frac{\pi}{2} - \arctan\left( \frac{x' - x}{R'} \right) \tag{2.26}$$

$$\varphi' = \varphi \tag{2.27}$$

depending on SAR coordinates range $R$ and azimuth $x$. The elevation angle $\varphi = 0$ is measured from the plane spanned by main lobe direction and track direction. The track direction is given by $\theta = 0$. The range line highlighted in Fig. 2.1 might have slant range distance $R_0$ and $\varphi = 0$.

By inspecting the phase term $\exp\{-\mathrm{j}2k_0 r'\} = \exp\{-\mathrm{j}2\pi f_{\mathrm{T}} \cdot 2r'/c_0\}$ in (2.23), the monostatic point target response is delayed by $\tau = 2r'/c_0$ and weighted by a function

$$w_{\mathrm{m}}(R', x - x', \varphi') = \frac{\sqrt{P_{\mathrm{Tx}}} G \lambda}{\sqrt{4\pi^3} \left( R'^2 + (x - x')^2 \right)} \left| C\left( \frac{\pi}{2} - \arctan\frac{x' - x}{R'}, \varphi' \right) \right|^2 \mathrm{e}^{\mathrm{j}2\psi(\vartheta',\varphi')} \,. \tag{2.28}$$

The antenna pattern weighting for the slant range $R_0$ using a rectangular aperture is [Bal16, p. 658]

$$C(\vartheta', 0) = \operatorname{sinc}\left(\frac{L}{\lambda}\cos\vartheta'\right) \approx \operatorname{sinc}\left(\frac{L}{\lambda}\frac{x'-x}{R_0}\right), \tag{2.29}$$

where (2.26), $\operatorname{sinc} = \sin(\pi x)/\pi x$, $R_0 \gg x' - x$ and $\sin\arctan y \approx y$ for small arguments are applied and $L$ denotes the transmitting and receiving antenna azimuthal length. A possible phase center variation could be specified per sidelobe, to cover the most significant changes in phase center variation [Bal16, pp. 773–774]. More accurate positioning of phase centers can be taken from high precision calibration measurements [Gab14; Jäg14]. However, the phase term $\psi(\vartheta', \varphi')$ is not further required and will be omitted.

The SAR system is not continuously transmitting an electromagnetic wave, but sampling the scene with bandwidth-limited coherent pulses of shape $s(t)$. The pulse shape is not of relevance for the considerations and assumed to be Dirac delta shaped. Coherent pulses are necessary to sample the phase in (2.23) [Cum05, pp. 134–136]. The baseband pulse received after time $\tau$ is

$$h\left(R, x, R', x', \varphi'\right) = w_{\mathrm{m}}\left(R', x - x', \varphi'\right)\mathrm{e}^{\mathrm{j}2\psi\left(\vartheta', \varphi'\right)}\mathrm{e}^{-\mathrm{j}2kr'}\,s(t-\tau) \tag{2.30}$$

and exclusively in global cylindrical coordinates

$$\begin{aligned} h\left(R, x, \boldsymbol{r}'\right) &= w_{\mathrm{m}}\left(R', x - x', \varphi'\right)\mathrm{e}^{-\mathrm{j}2k\sqrt{R'^2+(x-x')^2}}\,s\left(\frac{c_0}{2}\left(R - r'\right)\right) \\ &= w_{\mathrm{m}}\left(R', x - x', \varphi'\right)\mathrm{e}^{-\mathrm{j}2k\sqrt{R'^2+(x-x')^2}}\,s_{\mathrm{r}}(R - r'). \end{aligned} \tag{2.31}$$

A proper description of range-related dependencies is not necessary to simulate azimuth ambiguities. Hence, the steps of up/down-conversion, time delay, range compression and correction of range cell migration (RCM) are not explained in detail, but can be found in the literature [Bam98; Tom78; Cum05]. Only the azimuth dependencies for a constant range distance are further modeled and investigated.

### 2.3.2 Bistatic Impulse Response Function

Fig. 2.3 also shows the bistatic instantaneous Doppler frequency, which varies significantly from the monostatic instantaneous Doppler frequency, because the Harmony satellite observes the targets under a high forward looking angle (squint). The position of a point target in a spherical coordinate system attached to a phase center on the Harmony satellite is

$$\boldsymbol{r}'^{(\mathrm{H})} = \begin{pmatrix} r'^{(\mathrm{H})} \\ \vartheta'^{(\mathrm{H})} \\ \varphi'^{(\mathrm{H})} \end{pmatrix} = \begin{pmatrix} \sqrt{R'^2 + (x - x_0 - x')^2} \\ \begin{cases} \vartheta_{\mathrm{sq}} + \frac{\pi}{2} - \arctan\left(\frac{x'-x+x_0}{R'}\right) & \text{for } \arctan\left(\frac{x'-x+x_0}{R'}\right) \geq \vartheta_{\mathrm{sq}} - \frac{\pi}{2} \\ \vartheta_{\mathrm{sq}} + \frac{3\pi}{2} - \arctan\left(\frac{x'-x+x_0}{R'}\right) & \text{for } \arctan\left(\frac{x'-x+x_0}{R'}\right) < \vartheta_{\mathrm{sq}} - \frac{\pi}{2} \end{cases} \\ \varphi + \begin{cases} 0 & \text{for } \arctan\left(\frac{x'-x+x_0}{R'}\right) \geq \vartheta_{\mathrm{sq}} - \frac{\pi}{2} \\ \pi & \text{for } \arctan\left(\frac{x'-x+x_0}{R'}\right) < \vartheta_{\mathrm{sq}} - \frac{\pi}{2} \end{cases} \end{pmatrix}, \tag{2.32}$$

where $x$ still denotes the position of Sentinel-1. The main lobe direction of the antennas on Harmony remains at $\vartheta' = 90°$, which requires a rotation of the local spherical coordinate system by a squint angle

$\vartheta_{\mathrm{sq}}$. The SAR coordinates of the point target $\boldsymbol{r}' = (R', 0, x')^{\mathrm{T}}$ remain unchanged. Eqs. (2.25)–(2.27) may be reused to describe the transmit case from Sentinel-1

$$\boldsymbol{r}'^{(\mathrm{S})} = \begin{pmatrix} r'^{(\mathrm{S})} \\ \vartheta'^{(\mathrm{S})} \\ \varphi'^{(\mathrm{S})} \end{pmatrix} = \begin{pmatrix} \sqrt{R'^2 + (x - x')^2} \\ \frac{\pi}{2} - \arctan\left(\frac{x'-x}{R'}\right) \\ \varphi \end{pmatrix}. \tag{2.33}$$

With this geometric description a simplified bistatic IRF for raw SAR data may be defined similarly to (2.50)

$$\bar{h}_{\mathrm{b}}\left(R', x - x', \boldsymbol{r}'\right) = w_{\mathrm{b}}\left(R', x - x', \varphi'\right) \mathrm{e}^{-\mathrm{j}k_0\left(r'^{(\mathrm{S})} + r'^{(\mathrm{H})}\right)} s_{\mathrm{r}}\left(R - r'^{(\mathrm{S})} - r'^{(\mathrm{H})}\right), \tag{2.34}$$

with the bistatic weighting function

$$\begin{aligned} w_{\mathrm{b}}(R', x - x', \varphi') = \frac{\sqrt{P_{\mathrm{Tx}}\eta_{\mathrm{S}}D_{\mathrm{S}}\eta_{\mathrm{H}}D_{\mathrm{H}}}\lambda}{\sqrt{4\pi}^3 r'^{(\mathrm{S})} r'^{(\mathrm{H})}} \left| C_{\mathrm{S}}\left(\vartheta'^{(\mathrm{S})}, \varphi'^{(\mathrm{S})}\right) C_{\mathrm{H}}\left(\vartheta'^{(\mathrm{H})}, \varphi'^{(\mathrm{H})}\right) \right| \\ \cdot \exp\left\{ \mathrm{j}\left( \psi_{\mathrm{S}}\left(\vartheta'^{(\mathrm{S})}, \varphi'^{(\mathrm{S})}\right) + \psi_{\mathrm{H}}\left(\vartheta'^{(\mathrm{H})}, \varphi'^{(\mathrm{H})}\right) \right) \right\}. \end{aligned} \tag{2.35}$$

From the bistatic range history $r'^{(\mathrm{S})} + r'^{(\mathrm{H})}$, one can now derive the instantaneous Doppler frequency as plotted in Fig. 2.3

$$\begin{aligned} f_{\mathrm{D}}(x = v_{\mathrm{Sat}}t, x', x_0) &= -\frac{1}{\lambda}\frac{\mathrm{d}}{\mathrm{d}t}\left(r'^{(\mathrm{S})} + r'^{(\mathrm{H})}\right) \\ &= -\frac{v_{\mathrm{Sat}}}{\lambda}\left[\left(v_{\mathrm{Sat}}t - x'\right)\left(\frac{1}{r'^{(\mathrm{S})}} + \frac{1}{r'^{(\mathrm{H})}}\right) + \frac{x_0}{2}\left(\frac{1}{r'^{(\mathrm{S})}} - \frac{1}{r'^{(\mathrm{H})}}\right)\right]. \end{aligned} \tag{2.36}$$

Fig. 2.3 shows, that the Doppler centroid is not within the range of the Nyquist frequency $\pm f_{\mathrm{PRF}}/2$. Using a PRF $f_{\mathrm{PRF}}$ of about 1.5 kHz, the main signal part is aliased due to sampling with the stable PRF. The simulation is simplified by down-modulation of the IRF such that the Doppler centroid is within $\pm f_{\mathrm{PRF}}/2$. This down-modulation circumvents unnecessary small sampling steps to compute the raw SAR data, because only a limited bandwidth about the Doppler centroid $f_{\mathrm{DC}}$ is of interest. Thereto, a modulation frequency of $lf_{\mathrm{PRF}}$ is used, which preserves the alignment of the spectrum with respect to the boundaries $\pm f_{\mathrm{PRF}}/2$. It is finally found the IRF for simulation of raw SAR data

$$\tilde{h}_{\mathrm{b}}\left(R', x - x', \boldsymbol{r}'\right) = \bar{h}_{\mathrm{b}}\left(R', x - x', \boldsymbol{r}'\right) \mathrm{e}^{-\mathrm{j}\frac{2\pi}{\Delta x}lx}, \tag{2.37}$$

where $l \in \mathbb{N}$ minimizes the difference of Doppler centroid $f_{\mathrm{DC}}$ and a multiple of the sampling frequency $\left|f_{\mathrm{DC}} - lf_{\mathrm{PRF}}\right|$. The factor $l$ might be found by

$$l = \left\lfloor \frac{f_{\mathrm{DC}}}{f_{\mathrm{PRF}}} + \frac{1}{2} \right\rfloor = \left\lfloor \frac{v_{\mathrm{Sat}}}{\lambda f_{\mathrm{PRF}}} \frac{x_0}{\sqrt{R'^2 + x_0^2}} + \frac{1}{2} \right\rfloor = \left\lfloor \frac{\Delta x}{\lambda} \frac{x_0}{\sqrt{R'^2 + x_0^2}} + \frac{1}{2} \right\rfloor, \tag{2.38}$$

where $f_{\mathrm{DC}} = f_{\mathrm{D}}\left(t = x'/v_{\mathrm{Sat}}\right)$ using (2.36).

To minimize the effect of the phase of the IRF in the presence of misregistration on the interferometric performance [Bar99; Scho0], the residual Doppler centroid $\left|f_{\mathrm{DC}} - l f_{\mathrm{PRF}}\right|$ is set to zero by choosing an appropriate separation $x_0$. This removes the linear phase term due to non-baseband signals. In case of the Harmony mission setup, this yields a separation of Sentinel-1 and Harmony of 348 km, for a targeted separation of about 350 km.

Ambiguities are introduced by allowing the down-modulated IRF to span beyond the Nyquist frequency $\pm f_{\mathrm{PRF}}/2$. With these results the raw SAR data received by Harmony can be simulated as in the monostatic case before.

### 2.3.3 Spectrum of Impulse Response Functions

Later analysis and computations in Section 2.4 and Chapter 4 require the knowledge of the Fourier transform of the IRF. A method for numerically calculating its spectrum based on the principle of stationary phase (POSP) [Cum05, pp. 72–75] is applied in this section. More details on POSP may be found in the literature [Won01, pp. 76–84].

Firstly, the IRF of the one-dimensional raw SAR data (2.37) with $x' = 0$ is Fourier transformed with respect to azimuth position $x$ to find its spectrum as function of wavenumber $k$

$$\begin{aligned}\tilde{H}_{\mathrm{b}}\left(R', k, \varphi'\right) &= \int_{-\infty}^{\infty} \tilde{h}_{\mathrm{b}}\left(R', x, \boldsymbol{r}'\right) \mathrm{e}^{-\mathrm{j}kx}\,\mathrm{d}x = \int_{-\infty}^{\infty} w_{\mathrm{b}}\left(R', x, \varphi'\right) \mathrm{e}^{-\mathrm{j}k_0\left(r'^{(\mathrm{S})}+r'^{(\mathrm{H})}\right)} \mathrm{e}^{-\mathrm{j}\frac{2\pi}{\Delta x}lx} \mathrm{e}^{-\mathrm{j}kx}\,\mathrm{d}x \\ &= \int_{-\infty}^{\infty} w_{\mathrm{b}}\left(R', x, \varphi'\right) \mathrm{e}^{-\mathrm{j}\phi\left(R', x\right)}\,\mathrm{d}x\,, \end{aligned} \tag{2.39}$$

where the fast varying phase of the integrand is combined into

$$\phi\left(R', x\right) = k_0\left(r'^{(\mathrm{S})} + r'^{(\mathrm{H})}\right) + \frac{2\pi}{\Delta x} lx + kx\,. \tag{2.40}$$

Throughout this work, capitalized functions denote the frequency domain representation of its lowercase equivalent. The magnitude weighting $W_{\mathrm{b}}\left(R', x, \varphi'\right)$ is only slowly varying compared to the phase, hence the POSP [Cum05, p. 72] may be applied. The principle states, that only stationary points of the phase

$$\frac{\mathrm{d}\phi\left(R', x\right)}{\mathrm{d}x} = 0 \tag{2.41}$$

contribute to the integral. The first derivative of the phase term is found to be

$$\frac{\mathrm{d}\phi\left(R', x\right)}{\mathrm{d}x} = \frac{2\pi}{\Delta x} l + k + \frac{\mathrm{d}k_0}{\mathrm{d}(v_{\mathrm{Sat}} t)}\left(r'^{(\mathrm{S})} + r'^{(\mathrm{H})}\right) = \frac{2\pi}{\Delta x} l + k - \frac{2\pi}{v_{\mathrm{Sat}}} f_{\mathrm{D}}\left(\frac{x}{v_{\mathrm{Sat}}}\right). \tag{2.42}$$

The function of Doppler frequency is only hardly invertible to find the position $x$ as a function of Doppler frequency. On the other side, only low orders of ambiguities are of interest, because of their dominant power. By applying a Taylor approximation to linearize the Doppler frequency around its Doppler centroid

$$f_{\mathrm{D}}\left(\frac{x}{v}\right) \approx f_{\mathrm{DC}} + (x + x_0/2)\frac{1}{v_{\mathrm{Sat}}} \left.\frac{\mathrm{d}f_{\mathrm{D}}(t)}{\mathrm{d}t}\right|_{t=-\frac{x_0}{2}/v_{\mathrm{Sat}}} = f_{\mathrm{DC}} + (x + x_0/2)\frac{1}{v_{\mathrm{Sat}}} \left.\dot{f}_{\mathrm{D}}(t)\right|_{t=-\frac{x_0}{2v_{\mathrm{Sat}}}}, \tag{2.43}$$

the stationary points result from the local Doppler frequency rate $\dot{f}_\mathrm{D}(t)$ by

$$x(k) = \frac{\frac{2\pi l}{\Delta x} + k - \frac{2\pi}{v_\mathrm{Sat}}\left(f_\mathrm{DC} + \frac{x_0}{2v_\mathrm{Sat}}\dot{f}_\mathrm{D}(t)\Big|_{t=-\frac{x_0}{2v_\mathrm{Sat}}}\right)}{\frac{2\pi}{v_\mathrm{Sat}^2}\dot{f}_\mathrm{D}(t)\Big|_{t=-\frac{x_0}{2v_\mathrm{Sat}}}} . \tag{2.44}$$

Using these approximations, one finds the Fourier transform of the IRF approximately as [Won01; Cum05]

$$\tilde{H}_\mathrm{b}\left(R', k, \varphi'\right) \approx \tilde{h}_\mathrm{b}\left(R', (x)(k), \boldsymbol{r}'\right) , \tag{2.45}$$

where a constant multiplicative factor and an additive phase $\pi/4$ were neglected, compare [Cum05, p. 72].

### 2.3.4 Imaging Distributed Scenes

So far, the azimuth IRF of a point target has been found. But, SAR remote sensing is used to image complex scenes, e.g. Earth's surface, which comprises different scattering behaviors than represented by just a single point target. However, by assuming linearity, which requires no multiple scattering and no attenuation (shadowing), the imaging process may be written as a two-dimensional convolution [Bam98; Tom78; Cum05]

$$r(x, R) = \iiint a\left(R', x', \varphi'\right) h\left(R, x, R', x', \varphi'\right) \mathrm{d}V' , \tag{2.46}$$

using a generalized two-dimensional IRF $h(R, x, R', x', \varphi')$, i.e. for mono- or bistatic channels. The object function $a\left(R', x', \varphi'\right)$ represents the imaged scene as seen by the SAR system, i.e. it can contain information about partially shadowed points or multiple reflections [Bam98]. This integral bases on Kirchhoff approximation or "physical optics", which linearizes the calculation of scattered fields from the incident field from complex and rough surfaces. The approximation is covered in the literature and of no further importance for this work [War13, pp. 450–455].

The SAR system samples raw SAR data in both azimuth $x$ and range $R$ direction. Sampling in range is not of interest for azimuth ambiguities, hence, the two-dimensional integral is now reduced to a single range line at $R' = R_0$. Received raw SAR data $r[n, R_0]$ is obtained every

$$\Delta x = \frac{v_\mathrm{Sat}}{f_\mathrm{PRF}} , \tag{2.47}$$

and the range line at $R_0$ is set to be in main lobe direction $\varphi' = 0$

$$r[n, R_0] = \int_{-\infty}^{\infty}\int_{-\infty}^{+\infty}\int_{0}^{2\pi} a\left(R', x', \varphi'\right) R' \,\mathrm{d}\varphi' h\left(R_0, x, R', x', 0\right) \mathrm{d}R' \,\mathrm{d}x' \Bigg|_{x=n\Delta x} . \tag{2.48}$$

Because only a single range line is collected, the inherent RCM [Cum05, pp. 194–199] may be removed from the simulated data by unifying the phase history in range, i.e. for the monostatic case

$$2k\sqrt{R'^2 + (x - x')^2} \approx 2k\left(R' - R_0 + \sqrt{{R_0}^2 + (x - x')^2}\right) , \tag{2.49}$$

and neglecting RCM $R - r' \approx R - R_0$ of the received pulse envelope $s(t)$. This yields a simplified IRF

$$\bar{h}\left(R_0, x - x', \boldsymbol{r}'\right) = W\left(R_0, x - x', \varphi'\right) \mathrm{e}^{-\mathrm{j}2k\sqrt{{R_0}^2 + (x-x')^2}}\, s_\mathrm{r}(R - R_0)\,, \tag{2.50}$$

which confines raw SAR data to one range line at $R_0$. Although, RCM is present in real scenarios and the IRF of focused aliases (azimuth ambiguities) might blur slightly, the acquired main signal and ambiguities of distributed scenes are still coherent between channels [Zon22]. Neglecting the RCM to simplify calculations does not worsen the simulated results compared to real scenarios.

The pulse waveform with a compressed pulse length $\Delta R$ allows to reduce the integration boundaries

$$r[n, R_0] = \int_{-\infty}^{\infty} \int_{R_0 - \frac{\Delta R}{2}}^{R_0 + \frac{\Delta R}{2}} \int_{0}^{2\pi} a\left(R', x', \varphi'\right) R'\, \mathrm{d}\varphi'\, \mathrm{e}^{-\mathrm{j}2k(R' - R_0)}\, \mathrm{d}R'\, \bar{h}\left(R, x - x', R_0, 0\right) \mathrm{d}x' \Bigg|_{x = n\Delta x}\,, \tag{2.51}$$

because only the scatterers within this boundary mainly contribute to the received data.

The contribution by the object function is collected into a function of complex reflection coefficients

$$\Gamma'(x', R_0) = \int_{R_0 - \frac{\Delta R}{2}}^{R_0 + \frac{\Delta R}{2}} \int_{0}^{2\pi} a(R', x', \varphi') R'\, \mathrm{d}\varphi'\, \mathrm{e}^{-\mathrm{j}2k\left(R' - R_0\right)}\, \mathrm{d}R\,, \tag{2.52}$$

which is imaged by the SAR system into the range line $R_0$. For ocean and sea surfaces, this function is randomly complex Gaussian distributed, because the overall scattered field is the result of scattering at many randomly distributed capillary waves inside the resolution cell [War13; Has85]. The random fluctuation of scattered power is also known as speckle effect [Bam98; Has85; Jus94]. The variance of the complex Gaussian distribution

$$\Gamma'(x', R_0) \sim \mathcal{CN}\left(0,\ \sigma^0 \frac{\Delta_R}{\sin(\varphi_\mathrm{inc})}\right) \tag{2.53}$$

accounts for scattering from a surface with surface scattering coefficient $\sigma^0$ and unit $\left[\sigma^0\right] = \mathrm{m^2/m^2}$. The electromagnetic wave incides on the surface under an angle $\varphi_\mathrm{inc}$ with the normal of the horizontal surface of the flattened Earth in Fig. 2.1. Note, pulse compression focuses the received energy of the uncompressed pulse [Cum05, pp. 80–86], hence, the energy contribution is defined by the uncompressed pulse length $\Delta_R$.

Using the randomly distributed function of complex reflection coefficients yields the multiplicative noise model [Has85]. The model describes the scene in a frozen state. By "freezing" the position of scatterers, the simulation model remains linear and computationally efficient with the use of the discrete Fourier transform (DFT). The phase information from scatterer motion required for interferometry is added in a start-stop-approximation into the reflectivity function and modeled in Section 2.4.

The integration over target position $x' = \kappa\Delta x/\chi$

$$r[n, R] = \int_{-\infty}^{\infty} \Gamma'(x', R_0)\, \bar{h}\left(R, x, R_0, x', 0\right) \mathrm{d}x' \Bigg|_{x = n\Delta x} \tag{2.54}$$

is now discretized and combined with sampling of the raw data $x = n\Delta x$ to

$$r[n, R] = \sum_{\kappa=-\infty}^{\infty} \bar{h}\big(R, R_0, (n - \kappa/\chi)\Delta x, 0\big)\Gamma\left(\kappa\frac{\Delta x}{\chi}, R_0\right), \tag{2.55}$$

with an oversampling of the scene by $\chi$ samples. The function of reflection coefficients $\Gamma'$ and the finite line element $\Delta x/\chi$ are combined into a new reflection coefficient

$$\Gamma \sim f(\Gamma|\sigma^0) = \mathcal{CN}\left(0,\ \sigma^0\frac{\Delta x}{\chi}\frac{\Delta_R}{\sin(\varphi_{\text{inc}})}\right). \tag{2.56}$$

One sees, that the function of scattering coefficients has again a unit of $\left[\left|\Gamma(x, R_0)\right|^2\right] = \text{m}^2$.

The final one-dimensional raw SAR data model

$$r[n, R_0] = \sum_{\kappa=-\infty}^{\infty} W\left(R_0, \left(n - \frac{\kappa}{\chi}\right)\Delta x, 0\right)\text{e}^{-\text{j}2k\sqrt{{R_0}^2+\left(n-\frac{\kappa}{\chi}\right)^2\Delta x^2}}\Gamma\left(\kappa\frac{\Delta x}{\chi}, R_0\right) \tag{2.57}$$

is used to simulate received raw SAR data. The model for bistatic raw data is derived equivalently.

Numerical calculation of this data is done by, firstly, convolving oversampled Gaussian distributed scene data $\Gamma$ with the IRF of raw data $\bar{h}$ and, secondly, by picking only each $\chi$-th sample as received raw data sample. The convolution operation may also be implemented by using the DFT. Either procedure requires sufficient zero-padding to the output memory array.

### 2.3.5 Receive Noise and Signal-to-Noise-Ratio

The signal-to-noise-ratio (SNR) of a SAR system depends mainly on the reflectivity of the observed scene. For oceans and sea surfaces, only surface scattering is relevant. The received power while sensing a cluttered homogeneous area with surface scattering coefficient $\sigma^0$ is approximately given by [Cumo5, p. 8]

$$P_{\text{Rx}}(\sigma^0) = P_{\text{Tx}}G_{\text{Tx}}G_{\text{Rx}}\frac{\lambda^2}{(4\pi)^3{R_0}^4}\sigma^0 A, \tag{2.58}$$

where $A = R_0\lambda\Delta_R/L\sin(\varphi_{\text{inc}})$ is the illuminated area limited by beamwidth in azimuth and uncompressed pulse duration in range. The equation neglects the damping due to the antenna pattern, which results in a larger received power. This is corrected by using a factor

$$p_{0,\text{m}} = \frac{\int_{-\vartheta_{3\text{dB}}/2}^{\vartheta_{3\text{dB}}/2}\left|C(\vartheta + \pi/2, 0)\right|^4\,\text{d}\vartheta}{\int_{-\vartheta_{3\text{dB}}/2}^{\vartheta_{3\text{dB}}/2}\text{d}\vartheta} = \frac{L}{\lambda}\int_{-\lambda/2L}^{\lambda/2L}\text{sinc}\left(\frac{L}{\lambda}\sin\vartheta\right)^4\text{d}\vartheta$$

$$\approx \frac{L}{\lambda}\int_{-1/2}^{1/2}\frac{\lambda}{L}\,\text{sinc}(\nu)^4\,\text{d}\nu \approx 0.633\,22\,, \tag{2.59}$$

where $\sin\vartheta \approx \vartheta$ was used, in the monostatic case or in the bistatic case if one large antenna with azimuthal length $L_S$ determines the illuminated area

$$p_{0,b} = \frac{\int_{-\vartheta_{3dB}/2}^{\vartheta_{3dB}/2} \left|C(\vartheta + \pi/2, 0)\right|^2 \,\mathrm{d}\vartheta}{\int_{-\vartheta_{3dB}/2}^{\vartheta_{3dB}/2} \mathrm{d}\vartheta} = \frac{L_S}{\lambda} \int_{-\lambda/2L_S}^{\lambda/2L_S} \operatorname{sinc}\left(\frac{L_S}{\lambda}\sin\vartheta\right)^2 \mathrm{d}\vartheta$$

$$\approx \frac{L_S}{\lambda} \int_{-1/2}^{1/2} \frac{\lambda}{L_S} \operatorname{sinc}(\nu)^2 \,\mathrm{d}\nu \approx 0.773\,695\,. \quad (2.60)$$

The noise level of a SAR system is usually defined by relating to the (surface) scattering coefficient that achieves equal signal and noise power or unit SNR [Cal14; Cum05]

$$P_N = P_{Rx}(\sigma^0 = \sigma^0_{NE}) = p_0 P_{Tx} G_{Tx} G_{Rx} \frac{\lambda^3}{(4\pi)^3 R_0 ({R_0}^2 + x_0^2)} \frac{\Delta_R}{L \sin(\varphi_{inc})} \sigma^0_{NE}\,. \quad (2.61)$$

The corresponding (surface) scattering coefficient $\sigma^0_{NE}$ is called noise equivalent sigma nought (NESN).

The noise contribution is assumed to be additive white complex Gaussian distributed with variance $P_N$, because its main contribution is thermal noise [Bam98; Cum05; Tom78; Cal14].

### 2.3.6 Image Formation by Focusing

The SAR image is produced by focusing the raw and noisy data [Cum05, pp. 243–245]. In the point target case, the SAR system observes the Doppler history (2.45) during overflight. The spectrum or its time domain representation is comparable to a frequency chirp or frequency modulated signal. Focusing describes the technique of compressing this signal into a narrow pulse and might be performed in the spectrum by simple multiplication with $\tilde{H}^*_b(R', k, \varphi')$, see [Cum05; Tom78].

However, the observed spectrum (2.45) is not bandwidth limited and gets aliased when sampled by the SAR system. The aliased signal parts show a similar frequency chirp behavior compared to the non-aliased part, compare Fig. 2.3. Due to this similar characteristics, the aliased signals are (partially) matched to the focusing operator, which (partially) focuses them. These focused signal parts are called the azimuth ambiguities.

The following section combines the results of previous sections into a mathematical description of main and ambiguous signals for ATI with azimuth ambiguities, which are coherent between images.

## 2.4 Ambiguities in Along-Track Interferometry

Within this section, all previously introduced steps are combined to describe the complete interferometric signal with coherent ambiguities. Based on this description, a “transfer function" between signal and ambiguities is found, which finally leads to a complex azimuth-ambiguity-to-signal-ratio (CASR). This value is required for formulating the removal algorithm in Chapter 4.

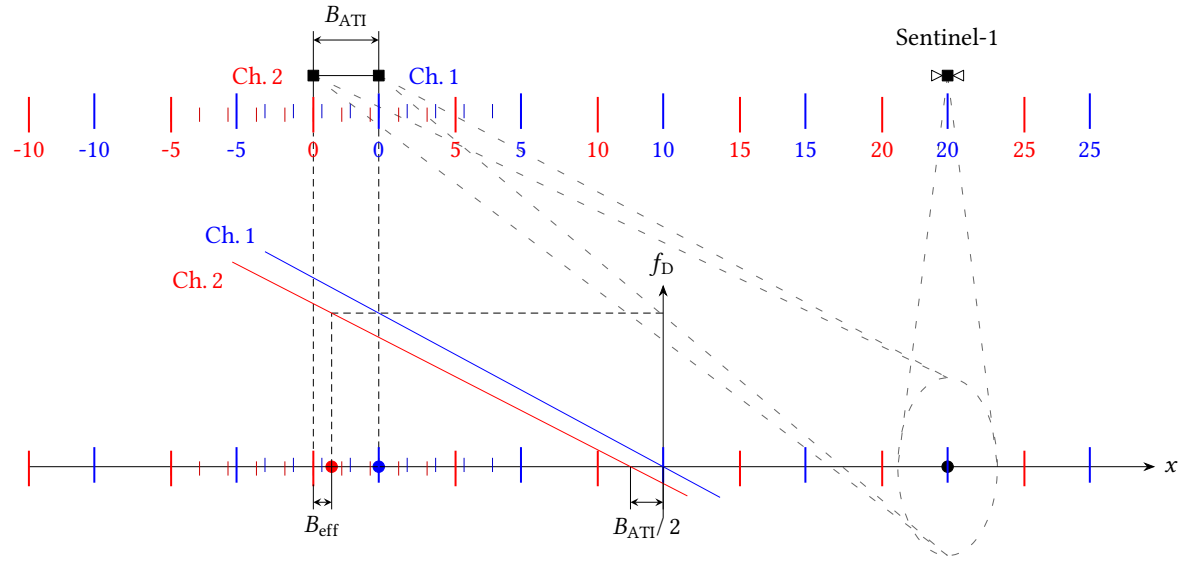


**Fig. 2.6**: Bistatic perceived Doppler frequency by channel 1 and 2 for a point target. Colored grid lines show an exemplary sampling with grids of channel 1 and 2 not being aligned and major grid illustrates every fifth pulse. The physical baseline is 2.25 times the sampling step, and Doppler rate is assumed constant but different for channel 1 and 2, resulting in $B_{\mathrm{eff}} \leq \frac{1}{2} B_{\mathrm{ATI}}$, where $B_{\mathrm{eff}}$ denotes the spatial shift within images for aligned grids.

### 2.4.1 Signal Block Diagram and Processing Steps

ATI requires at least two (bistatic) channels 1 and 2. The channels are arbitrarily denoted 1 and 2, but may use different combinations from the available antenna configuration depicted in Fig.2.2. The channels differ only in an along-track separation, which infers a time lag on channel 2 with respect to channel 1. Movement of the scene causes a phase change of the scene between channel 1 and 2, which is the new signal of interest and measured with ATI. The sampling is controlled by the Sentinel-1 satellite, whose transmitted pulses are simultaneously received by the antennas on Harmony, resulting each in a bistatic SAR channel. Because the antennas are spatially separated, the sampling per channel is not necessarily performed on the same grid, as depicted in Fig. 2.6. The received data is processed for both channels at the same Doppler frequency, which results in an focused point as shown exemplarily in Fig. 2.6.

### 2.4.2 Signal Description in Spectrum

The ATI signal model bases on the block diagram, as shown in Fig. 2.7. Its input is the proper complex Gaussian reflectivity scene $\Gamma_1(x)$ on channel 1 and $\Gamma_2(x)$ on channel 2, as derived in Section 2.3.4. The scenes differ due to motion of the surface and temporal de-correlation. However, the temporal delay between channel 1 and 2 is below the usual coherence time of sea and ocean surfaces [Car94; She93], which correlates the acquisitions. The sensing operation is denoted by two different transfer functions $H_1(k)$ and $H_2(k) \exp\{\mathrm{j}kB_{\mathrm{ATI}}/2\}$, and a sampling and digitization step, where amplitude quantization

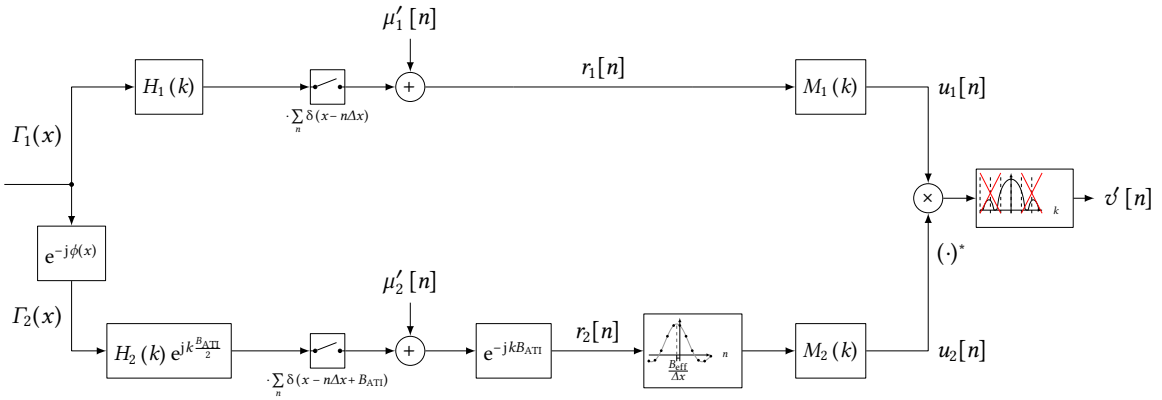


**Fig. 2.7**: Simplified signal processing and multiplicative noise simulation model for a bistatic ATI system.

is neglected. Those operations yield the received raw data per channel

$$R_1(k) = \sum_{i=-\infty}^{\infty} \Gamma_1\left(k - \frac{2\pi i}{\Delta x}\right) H_1\left(k - \frac{2\pi i}{\Delta x}\right) \tag{2.62}$$

$$R_2(k) = e^{-jkB_{ATI}} \left[\Gamma_2(k) H_2(k)\, e^{jk\frac{B_{ATI}}{2}} \circledast e^{j(k)B_{ATI}} \sum_{i=-\infty}^{\infty} \delta\left(k - \frac{2\pi i}{\Delta x}\right)\right] \tag{2.63}$$

$$= \sum_{i=-\infty}^{\infty} \Gamma_2\left(k - \frac{2\pi i}{\Delta x}\right) H_2\left(k - \frac{2\pi i}{\Delta x}\right) e^{-j\left(k - \frac{2\pi i}{\Delta x}\right)\frac{B_{ATI}}{2}}, \tag{2.64}$$

where $\circledast$ denotes the convolution operator and channel 2 needs an additional delay by $B_{ATI}$ to align the sampling grid with channel 1. The transfer functions for the sensing operation where derived in Section 2.3.2 and Fourier transformed in Section 2.3.3. The noise processes $\mu_1'[n]$ and $\mu_2'[n]$ add to the received signals and are parameterized according to Section 2.3.5. For further analytical calculations, one assumes a noise free system, because the interest is only in describing the effect of aliasing of the azimuth SAR signals on the interferogram.

In the next step, the raw data is focused at the Doppler centroid $k_{DC}$ of channel 1

$$U_1(k) = R_1(k) H_{m1}(k) = R_1(k) \sum_{l=-\infty}^{\infty} M_1\left(k - \frac{2\pi l}{\Delta x}\right) \Pi\left(\frac{k - k_{DC} - \frac{2\pi l}{\Delta x}}{k_{BW}}\right), \tag{2.65}$$

where a bandwidth $k_{BW} = 2\pi f_{BW}/v_{Sat}$ is processed and $\Pi(\cdot)$ is the rectangular function

$$\Pi(k) = \begin{cases} 1, & \text{if } |k| \le \frac{1}{2} \\ 0, & \text{if } |k| > \frac{1}{2} \end{cases}. \tag{2.66}$$

Channel 2 is additionally co-registered with channel 1 by interpolation, which reduces to a fractional shift [Cumo5, pp. 51–58]

$$U_2(k) = R_2(k) H_{m2}(k) \tag{2.67}$$

$$= R_2(k) \sum_{l=-\infty}^{\infty} M_2\left(k - \frac{2\pi l}{\Delta x}\right) e^{j\left(k - \frac{2\pi}{\Delta x}(l + l_{DC})\frac{B_{ATI}}{2}\right)} \Pi\left(\frac{k - k_{DC} - \frac{2\pi l}{\Delta x}}{k_{BW}}\right), \tag{2.68}$$

in the one-dimensional case. The fractional shift removes all linear phase slopes from the received data

$$U_2(k) = \sum_{i=-\infty}^{\infty} \sum_{l=-\infty}^{\infty} (\Gamma_2 H_2)\left(k - \frac{2\pi i}{\Delta x}\right) \mathrm{e}^{\mathrm{j}\frac{2\pi}{\Delta x}\frac{B_{\mathrm{ATI}}}{2}(i-l-l_{\mathrm{DC}})} M_2\left(k - \frac{2\pi l}{\Delta x}\right) \Pi\left(\frac{k - k_{\mathrm{DC}} - \frac{2\pi l}{\Delta x}}{k_{\mathrm{BW}}}\right). \tag{2.69}$$

The focusing kernels may be matched to the azimuth transfer function

$$M_1(k) = H_1^*(k) \tag{2.70}$$

$$M_2(k) = H_2^*(k)\,, \tag{2.71}$$

or phase only focusing with an additional windowing $W(k)$ of the maximum bandwidth $k_{\mathrm{BW}}$

$$M_1(k) = \frac{H_1^*(k)}{\left|H_1(k)\right|} W(k) \tag{2.72}$$

$$M_2(k) = \frac{H_2^*(k)}{\left|H_2(k)\right|} W(k)\,, \tag{2.73}$$

where $W(k) = |W(k)|$, and $H_1(k)$ and $H_2(k)$ may be found as described in Section 2.3.3. The purpose of window functions in this work is discussed later.

The samples of the images from channel 1 and 2 are interferometrically combined to form the interferogram

$$v[n] = u_1[n]u_2^*[n] = \frac{\Delta x}{2\pi} \int_{-\infty}^{\infty} V(k)\, \mathrm{e}^{\mathrm{j}kn\Delta x}\, \mathrm{d}k = \frac{\Delta x}{2\pi} \int_{-\frac{\pi}{\Delta x}}^{\frac{\pi}{\Delta x}} \left(U_1(k) \circledast U_2^*(-k)\right) \mathrm{e}^{\mathrm{j}kn\Delta x}\, \mathrm{d}k\,, \tag{2.74}$$

where the discrete spectrum is reduced to only one period of the periodic spectras, since $A(k) = A(k - 2\pi m/\Delta x)$ holds for $U_1(k)$ and $U_2(k)$ and therefore also for $V(k)$. The spectrum of the interferogram

$$\begin{aligned} V(k) &= U_1(k) \circledast U_2^*(-k) \\ &= \sum_{i_1,l_1,i_2,l_2} \mathrm{e}^{\mathrm{j}\frac{2\pi}{\Delta x}\frac{B_{\mathrm{ATI}}}{2}(l_2 - i_2 + l_{\mathrm{DC}})} \int_{-\infty}^{\infty} (\Gamma_1 H_1)\left(k' - \frac{2\pi i_1}{\Delta x}\right) M_1\left(k' - \frac{2\pi l_1}{\Delta x}\right) \Pi\left(\frac{k' - k_{\mathrm{DC}} - \frac{2\pi l_1}{\Delta x}}{k_{\mathrm{BW}}}\right) \\ &\qquad \cdot \left(\Gamma_2^* H_2^*\right)\left(k' - k - \frac{2\pi i_2}{\Delta x}\right) M_2^*\left(k' - k - \frac{2\pi l_2}{\Delta x}\right) \Pi\left(\frac{k' - k - k_{\mathrm{DC}} - \frac{2\pi l_2}{\Delta x}}{k_{\mathrm{BW}}}\right) \mathrm{d}k' \end{aligned} \tag{2.75}$$

is found by convolution of the two image spectra, where the summation is abbreviated by

$$\sum_{i_1,l_1,i_2,l_2} \equiv \sum_{i_1=-\infty}^{\infty} \sum_{l_1=-\infty}^{\infty} \sum_{i_2=-\infty}^{\infty} \sum_{l_2=-\infty}^{\infty}\,. \tag{2.76}$$

In a last step, the expected value of the interferogram samples is evaluated, to extract the interferometric information from the correlation of the random processes $\Gamma_1$ and $\Gamma_2$. It is started by evaluating the cross spectral density

$$P_{\mathrm{S},i_1,i_2}\left(k, k'\right) = \mathrm{E}\left[\Gamma_1\left(k' - \frac{2\pi i_1}{\Delta x}\right) \Gamma_2^*\left(k' - k - \frac{2\pi i_2}{\Delta x}\right)\right] \tag{2.77}$$

$$= \int_{-\infty}^{\infty} \int_{-\infty}^{\infty} \mathrm{E}\left[\Gamma_1(x_1)\Gamma_2^*(x_2)\right] \mathrm{e}^{-\mathrm{j}\left(k' - \frac{2\pi i_1}{\Delta x}\right)x_1} \mathrm{e}^{-\mathrm{j}\left(k - k' + \frac{2\pi i_2}{\Delta x}\right)x_2}\, \mathrm{d}x_1\, \mathrm{d}x_2\,, \tag{2.78}$$

where it is further assumed that the reflectivity scenes have a cross-correlation function [Has85; Bam98]

$$\mathrm{E}\left[\Gamma_1(x_1)\Gamma_2^*(x_2)\right] = \sigma^0(x_1)\left|\gamma(x_1)\right| \mathrm{e}^{\mathrm{j}\phi(x_1)}\,\delta(x_1 - x_2)\,. \tag{2.79}$$

Neighboring samples are not correlated due to random capillary waves on the sea surface with wavelengths in the order of the electrical wavelength $\lambda$ in C-band [Has85, p. 4660]. Because of the short temporal separation between channel 1 and 2, one can assume, that the scene is perfectly correlated, hence has a coherence

$$\left|\gamma(x_1)\right| = 1\,. \tag{2.80}$$

The interferometric properties, where $\sigma^0(x_1)$ is the scattering coefficient and $\phi(x_1)$ is the phase difference due to movement of the scene, must not be wide-sense stationary. Otherwise, there is no effect of bias by coherent ambiguities in the interferogram. Applying these assumptions, the cross spectral density reduces to

$$P_{\mathrm{S},i_1,i_2}\left(k,k'\right) = \int_{-\infty}^{\infty} \sigma^0(x_1)\,\mathrm{e}^{\mathrm{j}\phi(x_1)}\,\mathrm{e}^{-\mathrm{j}\left(k+\frac{2\pi}{\Delta x}(i_2-i_1)\right)x_1}\,\mathrm{d}x_1 = P_{\mathrm{S}}\left(k+\frac{2\pi}{\Delta x}(i_2-i_1)\right). \tag{2.81}$$

With use of the cross spectral density the expected interferometric samples are

$$\begin{aligned}\mathrm{E}\left[v[n]\right] = \frac{\Delta x}{2\pi}\sum_{i_1,l_1,i_2,l_2} \mathrm{e}^{\mathrm{j}\frac{2\pi}{\Delta x}\frac{B_{\mathrm{A}\Pi}}{2}(l_2-i_2+l_{\mathrm{DC}})} \int_{-\frac{\pi}{\Delta x}}^{\frac{\pi}{\Delta x}} P_{\mathrm{S}}\left(k+\frac{2\pi}{\Delta x}(i_2-i_1)\right)\\ \cdot \int_{-\infty}^{\infty} H_1\left(k'-\frac{2\pi i_1}{\Delta x}\right) M_1\left(k'-\frac{2\pi l_1}{\Delta x}\right)\Pi\left(\frac{k'-k_{\mathrm{DC}}-\frac{2\pi l_1}{\Delta x}}{k_{\mathrm{BW}}}\right) H_2^*\left(k'-k-\frac{2\pi i_2}{\Delta x}\right)\\ \cdot M_2^*\left(k'-k-\frac{2\pi l_2}{\Delta x}\right)\Pi\left(\frac{k'-k-k_{\mathrm{DC}}-\frac{2\pi l_2}{\Delta x}}{k_{\mathrm{BW}}}\right)\mathrm{d}k'\,\mathrm{e}^{\mathrm{j}kn\Delta x}\,\mathrm{d}k\,.\end{aligned} \tag{2.82}$$

Simplifying the formulation a last time, one finds for the expected interferometric sample value

$$\mathrm{E}\left[v[n]\right] = \frac{\Delta x}{2\pi}\sum_{i_1,m_1,i_2,m_2}\int_{-\frac{\pi}{\Delta x}}^{\frac{\pi}{\Delta x}} P_{\mathrm{S}}\left(k+\frac{2\pi}{\Delta x}(i_2-i_1)\right)F_{i_1,i_2,m_1,m_2}(k)\,\mathrm{e}^{\mathrm{j}kn\Delta x}\,\mathrm{d}k\,, \tag{2.83}$$

where a "transfer function"

$$\begin{aligned}F_{i_1,i_2,m_1,m_2}(k) = &\left(H_1\left(k-\frac{2\pi i_1}{\Delta x}\right)M_1\left(k-\frac{2\pi(i_1+m_1)}{\Delta x}\right)\Pi\left(\frac{k-k_{\mathrm{DC}}-\frac{2\pi(i_1+m_1)}{\Delta x}}{k_{\mathrm{BW}}}\right)\right)\\ &\circledast\left(H_2^*\left(-k-\frac{2\pi i_2}{\Delta x}\right)M_2^*\left(-k-\frac{2\pi(i_2+m_2)}{\Delta x}\right)\Pi\left(\frac{-k-k_{\mathrm{DC}}-\frac{2\pi(i_2+m_2)}{\Delta x}}{k_{\mathrm{BW}}}\right)\right)\mathrm{e}^{\mathrm{j}\frac{2\pi}{\Delta x}\frac{B_{\mathrm{A}\Pi}}{2}(m_2+l_{\mathrm{DC}})}\end{aligned} \tag{2.84}$$

for the expected interferometric signal $P_{\mathrm{S}}(k)$ and the ambiguity indices

$$m_1 = l_1 - i_1 \qquad\qquad m_2 = l_2 - i_2 \tag{2.85}$$

are introduced.

### 2.4.3 Complex Azimuth Ambiguity-to-Signal-Ratio from Signal Description

Eq. (2.83) contains the full information on the ambiguous interferogram for a scene cross spectral density

$$P_{\mathrm{S}}(k) = \int_{-\infty}^{\infty} \sigma^0(x)\, \mathrm{e}^{\mathrm{j}\phi(x)}\, \mathrm{e}^{-\mathrm{j}kx}\, \mathrm{d}x\,, \tag{2.86}$$

which is the Fourier transform of the interferometric properties along the azimuth direction $x$. The indices $i_1$ and $i_2$ in (2.83) describe the repetitiveness of the sampled spectrum. They are not of further interest and arbitrarily set to zero, because only the ratio of ambiguous signal to useful signal shall be investigated. Both, the ambiguous and useful signal, contain information on the scene $P_{\mathrm{S}}(k)$. Although, each signal part is weighted with a different wavenumber (frequency)-dependent function $F_{0,0,m,m}(k)$. The ratio of an ambiguous wavenumber component with index $m$ to its corresponding signal component

$$\begin{aligned}\alpha_m(k) &= \frac{F_{0,0,m,m}(k)}{F_{0,0,0,0}(k)} \\ &= \frac{H_1(k)M_1\left(k-\frac{2\pi m}{\Delta x}\right)\Pi\left(\frac{k-k_{\mathrm{DC}}-\frac{2\pi m}{\Delta x}}{k_{\mathrm{BW}}}\right) \circledast H_2^*(-k)M_2^*\left(-k-\frac{2\pi m}{\Delta x}\right)\Pi\left(\frac{-k-k_{\mathrm{DC}}-\frac{2\pi m}{\Delta x}}{k_{\mathrm{BW}}}\right) \mathrm{e}^{\mathrm{j}\frac{2\pi m}{\Delta x}\frac{B_{\mathrm{ATI}}}{2}}}{H_1(k)M_1(k)\,\Pi\left(\frac{k-k_{\mathrm{DC}}}{k_{\mathrm{BW}}}\right) \circledast H_2^*(-k)M_2^*(-k)\,\Pi\left(\frac{-k-k_{\mathrm{DC}}}{k_{\mathrm{BW}}}\right)}\end{aligned} \tag{2.87}$$

gives a wavenumber-dependent CASR, where the zero wavenumber component is

$$\alpha_m(0) = \alpha_m = \frac{\int_{k_{\mathrm{DC}}+\frac{2\pi m}{\Delta x}-\frac{k_{\mathrm{BW}}}{2}}^{k_{\mathrm{DC}}+\frac{2\pi m}{\Delta x}+\frac{k_{\mathrm{BW}}}{2}} H_1\left(k'\right)M_1\left(k'-\frac{2\pi m}{\Delta x}\right)H_2^*\left(k'\right)M_2^*\left(k'-\frac{2\pi m}{\Delta x}\right)\mathrm{d}k'}{\int_{k_{\mathrm{DC}}-\frac{k_{\mathrm{BW}}}{2}}^{k_{\mathrm{DC}}+\frac{k_{\mathrm{BW}}}{2}} H_1(k')M_1(k')H_2^*(k')M_2^*(k')\,\mathrm{d}k'}\, \mathrm{e}^{\mathrm{j}\frac{2\pi m}{\Delta x}\frac{B_{\mathrm{ATI}}}{2}}\,. \tag{2.88}$$

One sees an equivalence between this zero wavenumber component and the definition of azimuth-ambiguity-to-signal-ratio (AASR) for SAR images in the literature [Bay75; Li83]. The AASR is a ratio of aliased energy to signal energy, which can be found by integrating the energy from a certain angular portion of the antenna pattern. The equivalence with the introduced signal model holds only for homogeneous scenes with a Dirac-shaped Fourier transform

$$P_{\mathrm{S}}(k) = \int_{-\infty}^{\infty} \sigma^0\, \mathrm{e}^{\mathrm{j}\phi}\, \mathrm{e}^{-\mathrm{j}kx}\, \mathrm{d}x \propto \sigma^0\, \mathrm{e}^{\mathrm{j}\phi}\, \delta(k)\,, \tag{2.89}$$

because other wavenumber components experience a different ratio of ambiguous to signal magnitude, as defined by (2.87). Fig. 2.8 (a)–(c) depicts SAR images of typical scattering from oceans, that show a variation of scattering levels, called contrast [Vac92], and contradict a homogeneous assumption. Besides a very clutter-like appearance, which originates from speckle and thermal noise (especially in (a)) [Jus94], one can observe repetitive structures, which originate from modulation of the radar

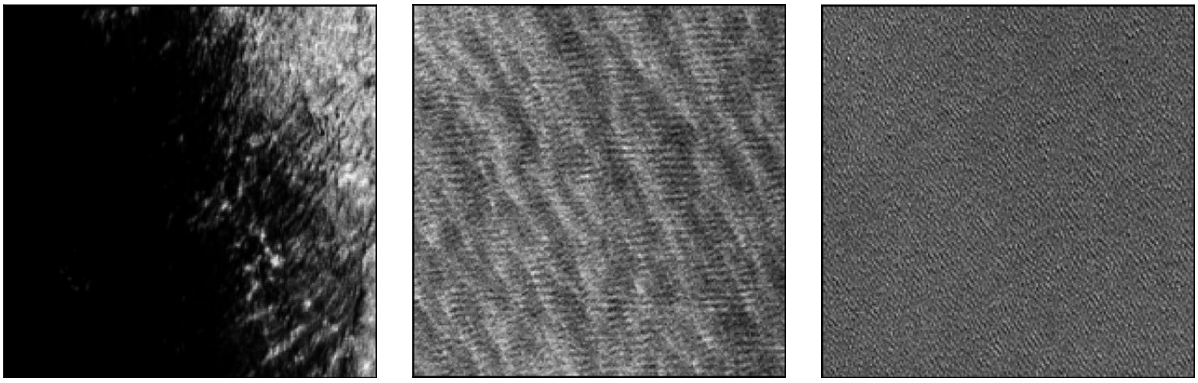

(a) Low wind sea (b) Wind waves (c) Pure ocean waves

**Fig. 2.8:** Sentinel-1 wave mode images of size of 20 km x 20 km and resolution of 5 m x 5 m showing exemplary sea types and their reflectivity signatures [Wan19].

scattering coefficient by waves. The most interesting case might be wind waves in (b), where surface wind acts on the sea surface and induces a modulation of the already wave-like scattering [Has85; War13; Vac92]. The analytic wavenumber-dependence of (2.87) is subject to analysis on real data, which is not covered within this work. Furthermore, it is assumed, as has been done throughout the literature [Li83; Lóp19a; Vil12], that AASR or CASR is a constant wavenumber-independent value. This assumption may be only valid for very narrow-banded cross spectral densities with slowly changing interferometric properties from waves with long wavelengths.

Eqs. (2.87) and (2.88) show an additional interferometric phase offset $\phi_{\mathrm{a},m} = 2\pi m B_{\mathrm{ATI}}/(2\Delta x)$, which adds and corrupts the interferometric phase per ambiguity. This phase offset is introduced due to the relative shift of images from channel 1 and 2. Note, each aliased signal contribution experiences this phase offset. Even the main signal of the Harmony mission, which has a Doppler centroid outside of $\pm f_{\mathrm{PRF}}/2$ and becomes aliased during observation. The offset may only be mitigated if channel 1 and 2 are sampling equal Doppler frequencies from the same positions in space, which requires the so called displaced phase center antenna (DPCA) condition [Dic91; Lig91]

$$\begin{aligned} & \frac{2\pi m}{\Delta x} B_{\mathrm{eff}} = 2\pi m m' \\ \Longleftrightarrow \quad & \frac{f_{\mathrm{PRF}}}{v_{\mathrm{Sat}}} B_{\mathrm{eff}} = m' \,, \end{aligned} \tag{2.90}$$

where $m'$ is the number of skipped pulses, to be fulfilled. This effect causes a loss of interferometric performance, when the DPCA condition is not fulfilled as observed in simulations [Lóp21].

### 2.4.4 Effective Baseline

Note, the spatial shift of images generated from channel 2 with respect to channel 1 is now denoted by an effective baseline

$$B_{\mathrm{eff}} = \Delta t v_{\mathrm{Sat}} = \frac{B_{\mathrm{ATI}}}{2} L_{\mathrm{d}} \,. \tag{2.91}$$

As introduced in Section 2.2, there is a reduction of the time delay between acquisitions for highly squinted bistatic setups. In the rectilinear geometry, there exists a proportionality between temporal

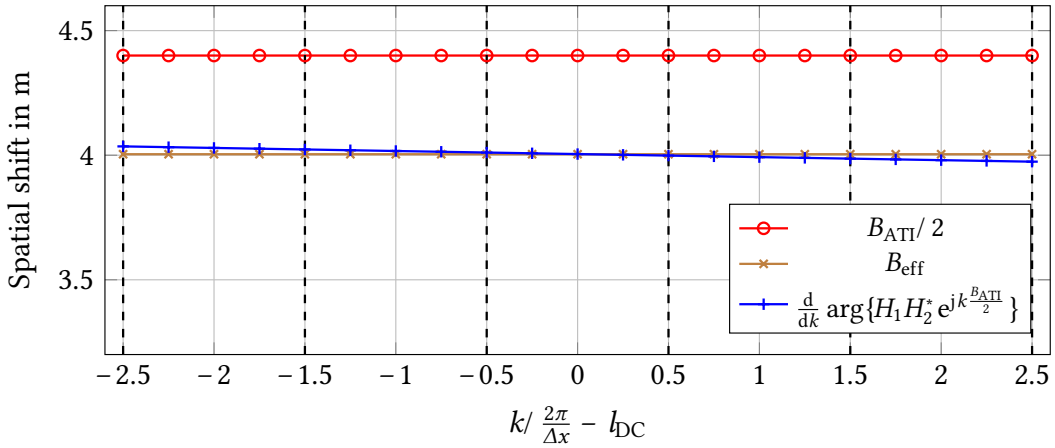


**Fig. 2.9:** Relative spatial shift of image from channel 2 with respect to image from channel 1 over normalized wavenumber.

delay and spatial shift with the satellite velocity being the proportionality constant [Cum05]. The spatial shift also shows a reduction by $L_{\mathrm{d}}$ as depicted in Fig. 2.9. The figure compares the spatial shift of the imaging transfer functions with aligned grids $H_1(k)$ and $H_2(k)\exp\{-\mathrm{j}kB_{\mathrm{ATI}}/2\}$, by means of a group delay calculation of the relative shift between the imaging transfer functions. Additionally, one observes by evaluating (2.87) or (2.88), that the Doppler loss factor also reduces the interferometric phase offset to $\phi_{\mathrm{a},m} = 2\pi m B_{\mathrm{eff}}/\Delta x$.

From Fig. 2.9 one finds, the spatial shift is varying with wavenumber. If the main signal part is perfectly co-registered, which means the spatial shift $B_{\mathrm{eff}}$ is completely removed, then, the ambiguities still posses an increasing misregistration with increasing ambiguity number. The misregistration related to azimuth resolution induces a loss of coherence [Han01, p. 46]. However, this relative misregistration is small for the first dominant ambiguities in the Harmony mission, because of an azimuth resolution of 20 m, which causes a negligible loss of coherence [Zon22].

The effective baseline is depending on range, because the Doppler loss factor is depending on range, as shown in Section 2.2. This effects the signal processing of the raw SAR data, which has to consider a range-dependent relative shift of the focused images. For instance, the co-registration or more specifically the focusing kernels, must know and compensate the range-dependent shift of the images generated from channel 1 and 2 during processing to avoid a loss of coherence [Han01, p. 46]. Another example is to fulfill the DPCA condition (2.90), which has to consider the range-dependent loss factor $L_{\mathrm{d}}$ when designing the phase center separation $B_{\mathrm{ATI}}$. Though, the DPCA condition may not be fulfilled over the whole swath, resulting in non-zero phase offsets per ambiguity $\phi_{\mathrm{a},m}$ and consequentially a decreased coherence [Lóp21]. Furthermore, removal algorithms will become more complex, i.e. IIR equalizer [Lóp19a], because the range-dependent additional interferometric phase offsets change over the swath extend and must be known, calculated, estimated or calibrated.

# 3 Simulation of Interferometric Performance

Interferometric performance quantifies the capability of an interferometric system to perform accurate measurements of the variable of interest. To evaluate this capability, one is interested in the distribution of the phase error

$$\phi_{\text{err}} = \left| \hat{\phi}_0 - \phi_0 \right| \tag{3.1}$$

as modulus deviation of the phase estimate $\hat{\phi}_0$ from its true value $\phi_0$. The true value and the scene follow prior distributions, which account for typical scene conditions to be observed by the Harmony mission. ATI estimates interferometric phases as a measurement of surface velocity, which are related by the ATI sensitivity (2.16). In this work, the error distribution

$$F(\Phi) = \Pr\left\{ \phi_{\text{err}} \leq \Phi \right\} \tag{3.2}$$

is evaluated under the influence of noise, coherent ambiguities and their suppression or removal by algorithms. Other error sources, i.e. system and processing errors [Cum05; Wol17], are excluded.

The analytic method of finding the error distribution requires marginalization of the conditional probability density function over prior distributions and a subsequent integration, which yields the error distribution. The conditional probability density function describes all imaging and signal processing steps and may not be found in a closed form. However, one can approximate the error distribution by means of a Monte Carlo simulation, where the desired distribution is estimated from discrete evaluations of the underlying mathematical model [Leh08, pp. 442–443]. For each evaluation, input parameters are sampled from their prior distributions and the resulting phase error is determined using the model as derived in Chapter 2. Such a Monte Carlo simulation is asymptotically efficient, meaning, that more evaluations achieve better accuracy [Leh08, pp. 442–443]. The simulations conducted showed, that a number of 2048 evaluations are sufficient for the purpose of this work and within reasonable computation effort. With 2048 evaluations, the Dvoretzky-Kiefer-Wolfowitz inequality states, that the maximum modulus deviation of the simulated error distribution from the true distribution is below 0.03 (3%) with a probability of 94.98% [Mas90]. Throughout this work, characterization and comparisons of interferometric performance are made on basis of two quantiles of the error distribution [Leh08]

$$\Phi_{68.2\%} = \left\{ \Phi \in \mathbb{R}_{\geq 0} \,\middle|\, F(\Phi) = 0.682 \right\} \tag{3.3}$$

$$\Phi_{95.4\%} = \left\{ \Phi \in \mathbb{R}_{\geq 0} \,\middle|\, F(\Phi) = 0.954 \right\}, \tag{3.4}$$

where $\mathbb{R}_{\geq 0}$ is the set of non-negative real numbers. These quantiles account for 68.2% and 95.4% of the phase error. Note, that the quantiles correspond to the $1\sigma$ and $2\sigma$ values of the error distribution, if $\hat{\phi}_0 - \phi_0$ is zero-mean normally distributed. Note further, that those values quantify the error in line-of-sight direction. The error on ground is found by inversion of the observation geometry using both Harmony satellites. This procedure depends on the current position within the swath and will only complicate the results. Hence, all performance analysis is done with respect to line-of-sight direction.

## 3.1 Monte Carlo Simulation Procedure

### 3.1.1 Model Setup

The simulation of interferometric performance uses the fact, that an ambiguity appears spatially shifted from the main signal [Ran87], to divide the simulated range line in several non-overlapping parts. Typical azimuth shifts for the Harmony mission are in the order of 3 km to 4 km for the first ambiguity, depending on system parameters. Each part is assigned an interferometric property from a set of $2M + 1$ interferometric properties

$$\boldsymbol{s} = \begin{bmatrix} \sigma_{-M}^{0}\, \mathrm{e}^{\mathrm{j}\phi_{-M}} \\ \vdots \\ \sigma_{0}^{0}\, \mathrm{e}^{\mathrm{j}\phi_{0}} \\ \vdots \\ \sigma_{M}^{0}\, \mathrm{e}^{\mathrm{j}\phi_{M}} \end{bmatrix} \in \mathbb{C}^{2M+1\times 1}\,. \tag{3.5}$$

The interferometric properties are assumed and modeled to be independent and identically distributed over their corresponding part. *Independent* relates to cross-correlation between elements of $\boldsymbol{s}$ and is assumed in order to evaluate the worst-case scenario. It only holds, if the displacement of ambiguities is in the order of length of ocean waves. *Identically* follows from the fact, that the sea state is valid over areas much larger than the displacement of ambiguities [War13, p. 20].

The analysis of system performance is confined to one part of this range line, with an extension in azimuth of 1.2 km. This extent is used as reference product resolution in the Harmony mission case [Rom20] and more stringent than analyzed for a similar study [Wol17].

The integer number $M$ denotes the highest considered ambiguity. In reality, $M$ takes a very large number of ambiguities, which contribute to the measured data. The number is smaller than infinity, due to the saturation of maximum Doppler frequency, compare Fig. 2.3. Additionally, the ambiguities loose their coherent property with increasing number $M$, because of increasing misregistration as discussed in Section 2.4.4 [Zon22]. For interferometric performance evaluations, only the first three ambiguities ($M = 3$) are considered, because the damping by the antenna pattern increases with larger deviation from the main beam and the computation requirements are kept at a reasonable level.

To verify the implemented SAR data model, the simulated interferometric performance is compared to an analytically derived reference performance. Under fully developed speckle by scattering from rough surfaces [War13, pp. 24, 289, 442–443], the phase error shows an analytical phase bias [Zon22]

$$\phi_{\mathrm{bias}\,|\,\boldsymbol{s}} = \arg\left\{ 1 + \sum_{m=-M,\, m\neq 0}^{M} \frac{\alpha_m \sigma_m^0}{\sigma_0^0}\, \mathrm{e}^{\mathrm{j}(\phi_m - \phi_0)} \right\} \tag{3.6}$$

using the CASR (2.88), and a phase variance [Tou94]

$$\sigma^2_{\phi\,|\,\boldsymbol{s}} = \frac{1}{N_{\mathrm{tot}}} \frac{1 - \left|\gamma(\boldsymbol{s})\right|^2}{2\left|\gamma(\boldsymbol{s})\right|^2}\,, \tag{3.7}$$

where $N_{\mathrm{tot}}$ samples are averaged and $|\gamma(\boldsymbol{s})|$ is the normalized cross-correlation coefficient (coherence) between the two channels. The expression for coherence is generalized from [Vil12] for arbitrary

many ambiguities

$$\left|\gamma(\boldsymbol{s})\right| = \frac{1}{1+\frac{\sigma^0_{\mathrm{NE}}}{\sum_{m=-M}^{M}\sigma^0_m|\alpha_m|}}\frac{1}{\sum_{m=-M}^{M}\sigma^0_m|\alpha_m|}\sqrt{\left(\sum_{m=-M}^{M}\sigma^0_m\alpha_m\,\mathrm{e}^{\mathrm{j}\phi_m}\right)\left(\sum_{m=-M}^{M}\sigma^0_m\alpha^*_m\,\mathrm{e}^{-\mathrm{j}\phi_m}\right)}. \tag{3.8}$$

Using the Monte Carlo simulation approach with 2048 evaluations, for each evaluation, firstly, $\boldsymbol{s}$ is sampled from prior distributions described in the next section, then a phase error estimate is sampled from a normal distribution [Tou94]

$$\hat{\phi}_{0,\mathrm{ref}} - \phi_0 \sim \mathcal{N}\left(\phi_{\mathrm{bias}\,|\,\boldsymbol{s}},\, \sigma^2_{\phi\,|\,\boldsymbol{s}}\right). \tag{3.9}$$

From all 2048 phase error estimates, the 68.2%- and 95.4%-quantiles are calculated.

To conclude this section, an exemplary range line from the simulation model with only the first left and right ambiguity in Fig. 3.1 is discussed. The figure shows also the expected values of interferometric phase and coherence calculated from (3.6) and (3.8). In this example, the interferometric properties are deliberately chosen such that the impact of coherent ambiguities and the additional interferometric phase offset per ambiguity $\phi_{\mathrm{a},m}$, here 284.5°, are highlighted. For the middle and right part of the range line, the interferometric phases of the main signal and the first left or right ambiguity are equal. This generates no loss in coherence and does not increase phase noise, although the signal parts are statistically independent. De-correlation in the right part occurs only due to constant additive thermal noise and a lower surface scattering coefficient, which leads to a smaller SNR. Contrary is the left part of the range line. The scattered power and the interferometric phase are identical to the right part. Though, one observes a phase bias and loss of coherence, which results in larger phase noise, because the interferometric phases of main and ambiguous signal are out of phase.

### 3.1.2 Prior Distributions

In this section, the prior distributions of surface scattering coefficient $\sigma^0_m$ and interferometric phase $\phi_m$ are introduced.

Ocean or sea surfaces comprise of two different wave types, which influence the scattering behavior. Capillary waves have rather small wavelength, much smaller than the size of a resolution cell for the Harmony mission. The incident electromagnetic wave interferes with these capillary waves and the resulting scattering coefficient becomes Gaussian distributed [Has85; War13]. On large scale observation of the averaged received power over many resolution cells, one observes a modulation of the surface scattering coefficient, which is induced by gravity waves. Their shape depends on wind speed, which determines the swell height and sea state [War13]. The modulation of surface scattering coefficient $\sigma^0_m$ by gravity waves is best described by a gamma distribution [War13]

$$\sigma^0_m \sim f(\sigma^0_m) = \frac{b^\nu}{\Gamma(\nu)}{\sigma^0_m}^{\nu-1}\mathrm{e}^{-b\sigma^0_m}, \tag{3.10}$$

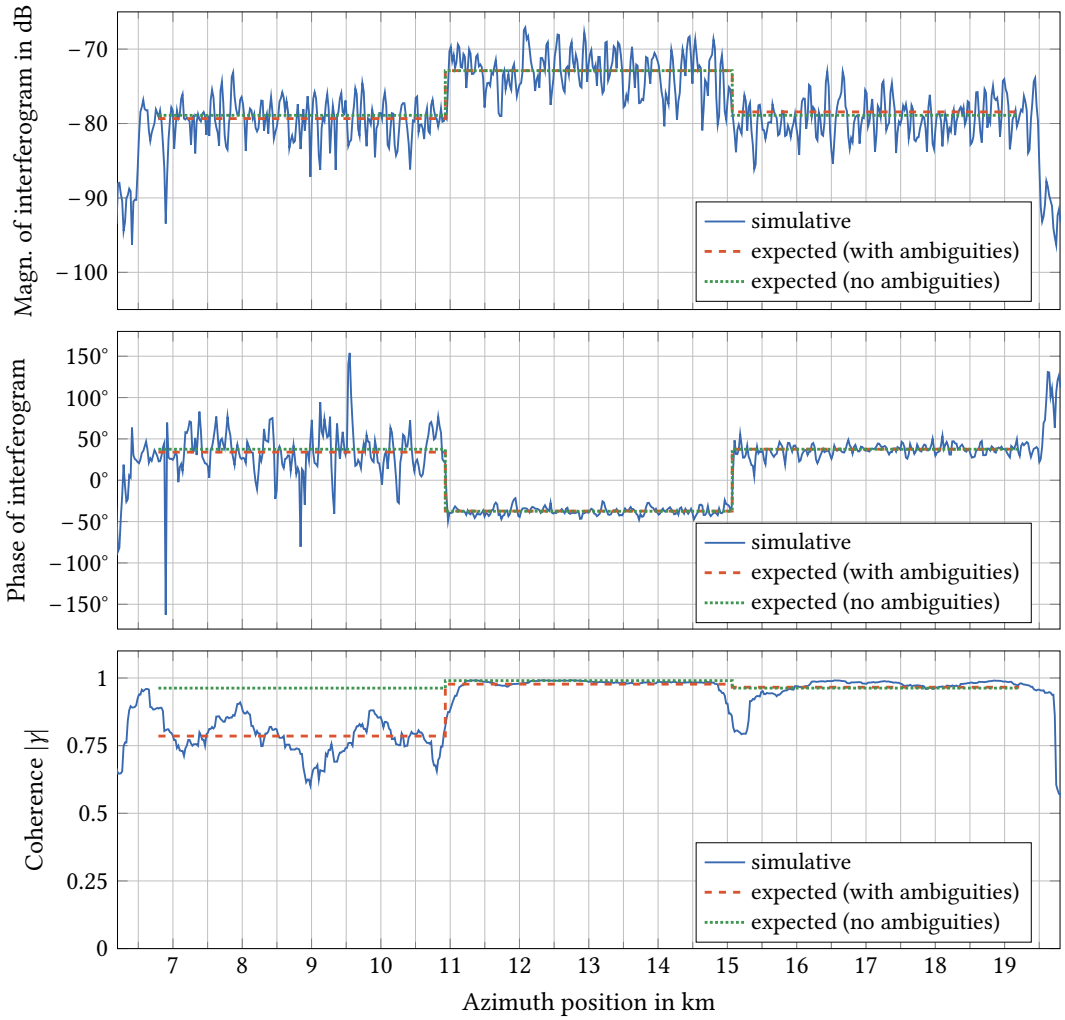


**Fig. 3.1:** Exemplary one-dimensional SAR interferogram (magnitude, phase and coherence) illustrating the effect of the first left and right ambiguity on phase noise and coherence at a NESN of −20 dB.

with shape parameter $\rho$, rate parameter $b$ and Gamma function $\Gamma(\cdot)$ [Papo2]. The first two moments

$$\mathrm{E}\left[\sigma^0\right] = \frac{\rho}{b} \qquad \rho = \frac{\mathrm{E}\left[\sigma^0\right]^2}{\mathrm{Var}\left[\sigma^0\right]} \tag{3.11}$$

$$\mathrm{Var}\left[\sigma^0\right] = \frac{\rho}{b^2} \qquad b = \frac{\mathrm{E}\left[\sigma^0\right]}{\mathrm{Var}\left[\sigma^0\right]} \tag{3.12}$$

are sufficient to fully characterize the gamma distribution [Papo2].

The gamma distribution of surface scattering coefficient depends on radar parameters (frequency, polarization, resolution, incidence angle), but also sea parameters (wind speed and direction, sea roughness). The prior distribution used for the evaluation of interferometric performance is taken from data measured by Sentinel-1. Tab. 3.1 shows the shape parameter and mean scattering coeffi-

**Tab. 3.1:** Sea clutter gamma distribution parameters from Sentinel-1 wave mode data for different wind conditions and Douglas sea states, as defined in [War13, p. 20]

| Douglas sea state | Wind speed in m/s | Mean E$[\sigma^0]$ in dB m²/m² | Shape $\nu$ | Rate $b$ in m²/m² | Variance Var$[\sigma^0]$ in dB m⁴/m⁴ |
|---|---|---|---|---|---|
| 2 | 3.78 | −19.7 | 2.6094 | 243.50 | −43.565 |
| 5 | 10.53 | −11.8 | 2.5829 | 39.093 | −27.721 |
| 6 | 15.23 | −5.9 | 3.4591 | 13.459 | −17.190 |

cient derived from the data. These parameters are sufficient for a complete characterization of the underlying gamma distribution [Pap02]. Sentinel-1 data may best represent the expected surface scattering coefficients, because Sentinel-1 is used as active satellite in the Harmony mission. The angle-dependency of the scattering coefficient for the bistatic Harmony mission is neglected [War13].

The distribution of possible interferometric phases $\phi_m$ is defined by requirements of the Harmony mission [Rom20]. A maximum of 90 cm/s must be observable. The observed interferometric phases are assumed to be uniformly distributed

$$\phi_m \sim f(\phi_m) = \mathcal{U}(-90\ \text{cm/s}\, S_{\text{ATI}}\,, 90\ \text{cm/s}\, S_{\text{ATI}})\,, \tag{3.13}$$

because there are no further restrictions.

## 3.2 Verification of the Simulation Model

In a first step, the uncorrected errors of simulated data are compared to theoretical errors to verify the simulation of biases by coherent ambiguity. The simulation model is configured with the Harmony parameter values given in Tab. A.1 in the Appendix. The curves in Fig. 3.2 show a good agreement between simulated and analytically evaluated interferometric performance. One sees influences from both, firstly, additive noise for low numbers of samples and secondly, coherent ambiguities for large numbers of samples. The second observation that is made is, that for decreasing SNR — starting at sea state 6 to sea state 5 and sea state 2 — more numbers of samples must be averaged to achieve equal error quantiles. Therefore, the Harmony mission targets product resolutions between 1 km² to 25 km² ($10^4$ to $25 \cdot 10^4$ samples) to achieve its observation accuracy requirements [Rom20]. Note, the boundary of 20 cm/s is only given as a reference. The true maximum error is below 20 cm/s, because the sensitivity reduces due to the projection of ground velocity into the line-of-sight plane.

In a second step, the sampling spacing is varied, which results in a not fulfilled DPCA condition. Fig. 3.3 depicts the expected performance deviation for a non-fulfilled DPCA condition, i.e. due to variation of the Doppler loss factor over the full swath. One sees, for a Doppler loss factor variation of −2.08% to 1.53% there is only negligible loss in interferometric performance, because the additional interferometric phase offset caused by this variation is small compared to the support of the prior phase distribution. The interferometric performance is mainly determined by this prior phase distribution. Further analysis is only made for the mid range case, where the DPCA condition is fulfilled. Fig. 3.3 does not include the effect of the antenna pattern variation over the swath. The gain of the antenna over elevation is reducing for near and far ranges [Bal16], which increases the NESN, due to a reduced signal level. Additionally, the shape of the antenna pattern changes over elevation [Bal16]. Both effects

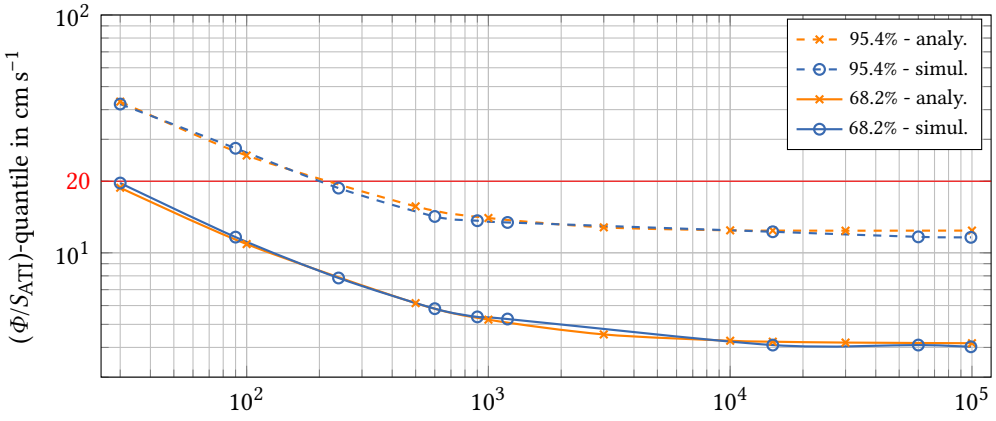


(a) Douglas sea state 6: Wind speed of 15.23 m/s, $\mathrm{E}\left[\sigma^0\right] = -5.9$ dB

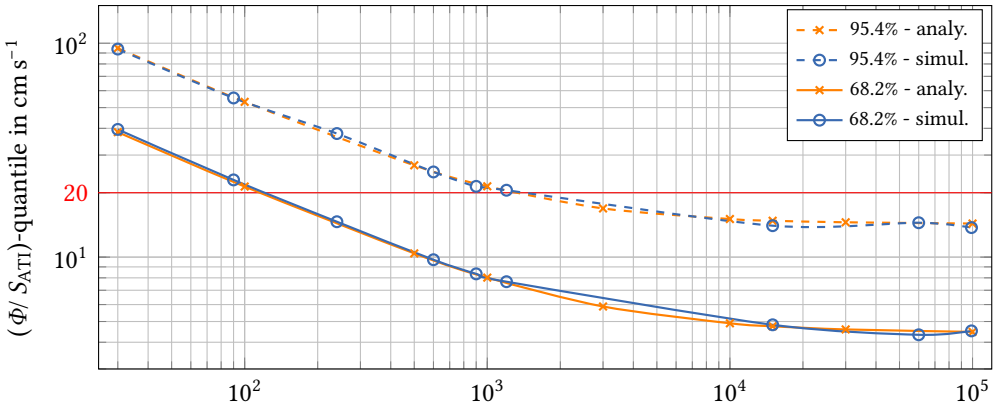


(b) Douglas sea state 5: Wind speed of 10.53 m/s, $\mathrm{E}\left[\sigma^0\right] = -11.8$ dB

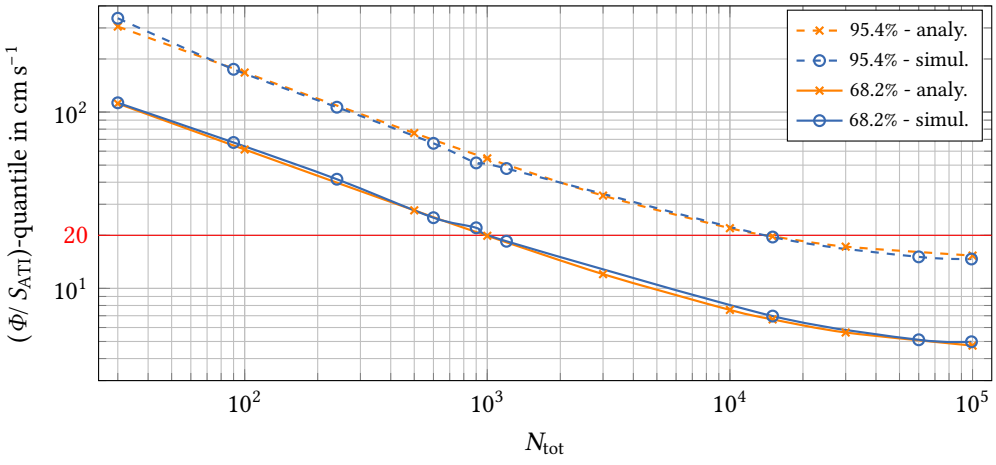


(c) Douglas sea state 2: Wind speed of 3.78 m/s, $\mathrm{E}\left[\sigma^0\right] = -19.7$ dB

**Fig. 3.2:** Analytical and simulated interferometric performance of ATI system without azimuth ambiguity removal.

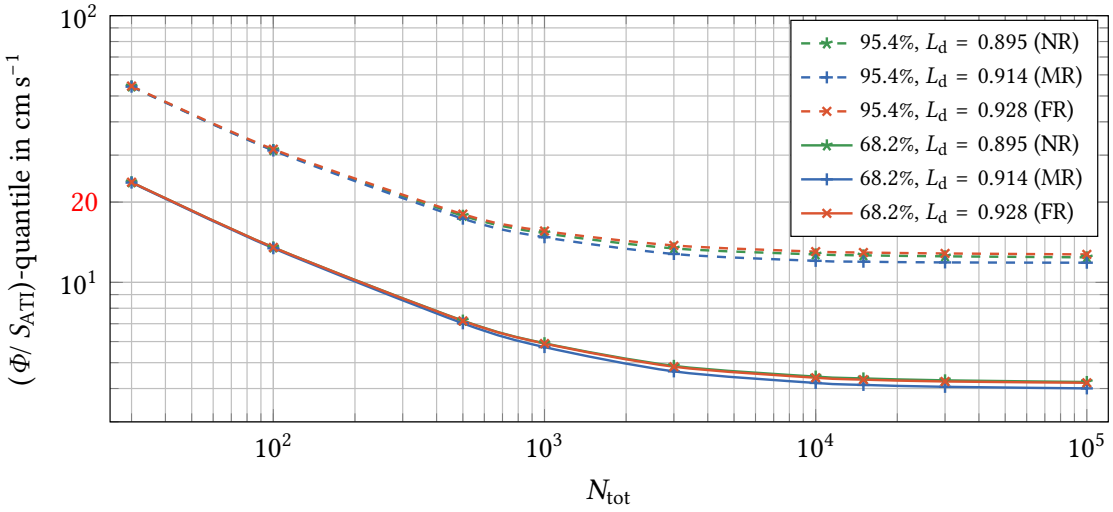


**Fig. 3.3:** Interferometric performance of ATI system without azimuth ambiguity removal for different Doppler loss factors, which correspond to expected losses in near range (NR), mid range (MR) and far range (FR) scenarios. DPCA condition is only fulfilled in mid range case.

can be modeled as shown in Chapter 2 and the interferometric performance may be evaluated, but they are not relevant when comparing different algorithms. This work skips a detailed analysis.

## 3.3 Model-Induced Biases without Coherent Ambiguities

Non-optimum processing, variation in Doppler rate per channel[2] and residual misregistration causes inherent residual biases in the simulation model. Also, the infinitely long IRF of the focused data contributes to biases at the ambiguous positions. For this work, it is not of interest which effect is limiting the simulated interferometric performance. But, it is of interest to quantify the model-induced biases, which are not related to coherent ambiguities. Simulations without additive noise show, that the 68.2%-quantile is limited to 0.0082° or 0.094 cm/s and the 95.4%-quantile is limited to 0.0258° or 0.296 cm/s. Fig. 3.4 depicts the lower limits over number of samples down to which coherent ambiguity biases and the corresponding removal algorithm can be simulated and evaluated.

2 Results in a non-flat (but linear) interferometric phase over the peak of the impulse response [Cumo5, pp. 82–87, p. 110]

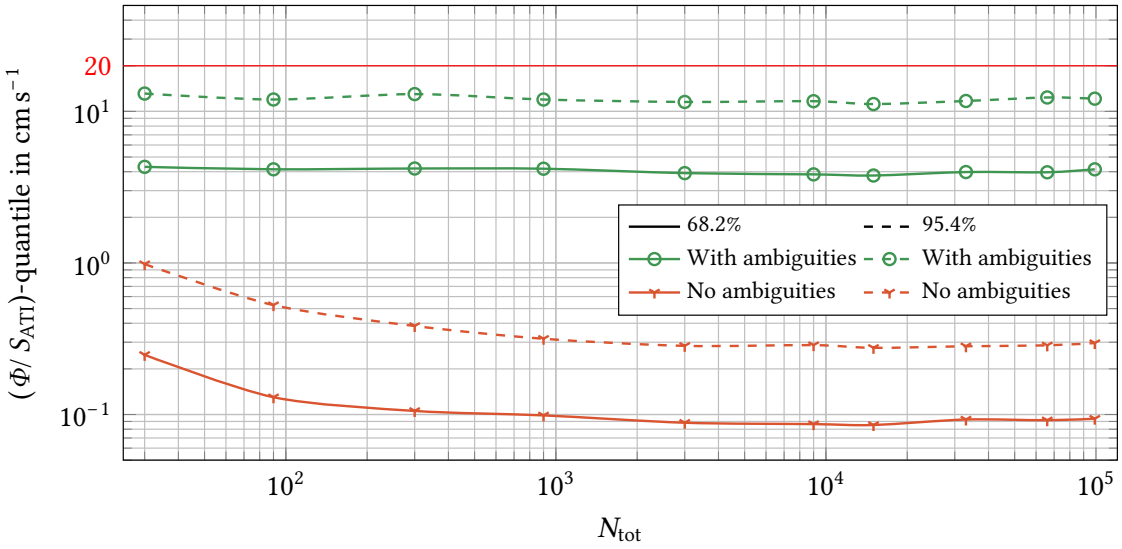


**Fig. 3.4**: Simulated interferometric performance of ATI system when DPCA condition is fulfilled without noise comparing the effect of azimuth ambiguities and model-induced biases.

# 4 Ambiguity Removal on Interferogram Level

In the following, a technique to remove azimuth ambiguities from the interferogram is introduced and later verified using simulated data. The following description aims on the investigation of the achievable performance of the technique. An implementation on real interferometric data must be done outside the scope of this work.

## 4.1 Modulation of Ambiguous and Main Signal by Looks

Fig. 4.1 shows a usual SAR system design. To minimize the ambiguous energy one usually places a zero of the antenna pattern such that it aligns with the Doppler centroid, i.e. Sentinel-1 [Tor17]. This might also be achieved by means of digital beamforming, where several SAR channels are combined to place a zero on receive. This technique and its application to SAR may be found in the literature [Kri03; You03]. The Harmony mission setup bears the potentials of forming new useful channels by two combinations, i.e. fore-middle or aft-middle. Interferograms might then be created from any original or combined channel, i.e. (fore-middle)-to-aft. The further analyzed system assumes the antenna pattern weighting as given in Fig. 4.1.

When applying a multi-look processing scheme in the frequency domain, the processed bandwidth is commonly divided into looks with partially overlapping spectral support, as shown in Fig. 4.2 [Por76; Moo79]. Besides a generation of partially independent images, multi-look processing modulates the CASR over the looks, due to bandpass-filtering of the ambiguities by the window functions. Tab. 4.1 gives the numerically evaluated magnitude of the CASR for the first three ambiguities for the exemplary antenna configuration in Fig. 4.1 and the Hamming window functions in Fig. 4.2.

The motion of the scene infers DCA, which results in a shift of the antenna pattern in Fig. 4.1 [Cum05, pp. 483–484]. This shift modifies the modulated CASR and will introduce estimation errors if not considered. An approximate estimate of this shift is found from the biased velocity estimate without coherent azimuth ambiguity removal. The remaining error on antenna pattern knowledge due to biased shifts may be tolerated [Ric22].

For white scenes or at least constant spectral power density per ambiguity, windowing modulates the power of main and ambiguous contribution according to the modulation of CASR, as shown in Tab. 4.1. A white scene holds for fully developed speckle on ocean and sea surfaces [War13; Has85]. Otherwise, the scene itself will contribute with an unknown modulation and deteriorate the removal capabilities of the technique. The known modulation of energies is further leveraged to estimate the main signal.

## 4.2 Removing Modulated Ambiguities

Each window function is applied to both channels to generate looks before interferometric combination according to the block diagram in Fig. 4.3. The pairs of generated looks form a time series of $B$

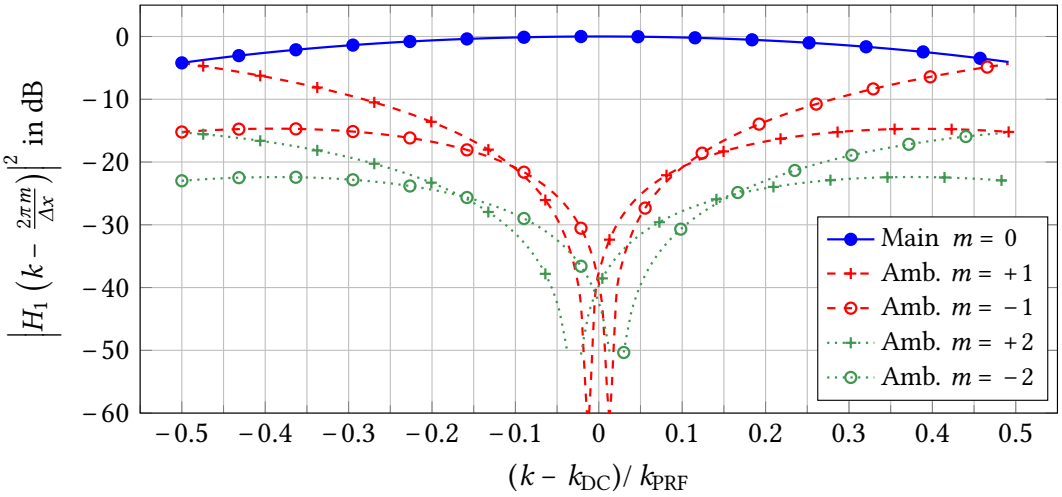


**Fig. 4.1:** Exemplary spectral magnitude of signal and aliases of a SAR system.

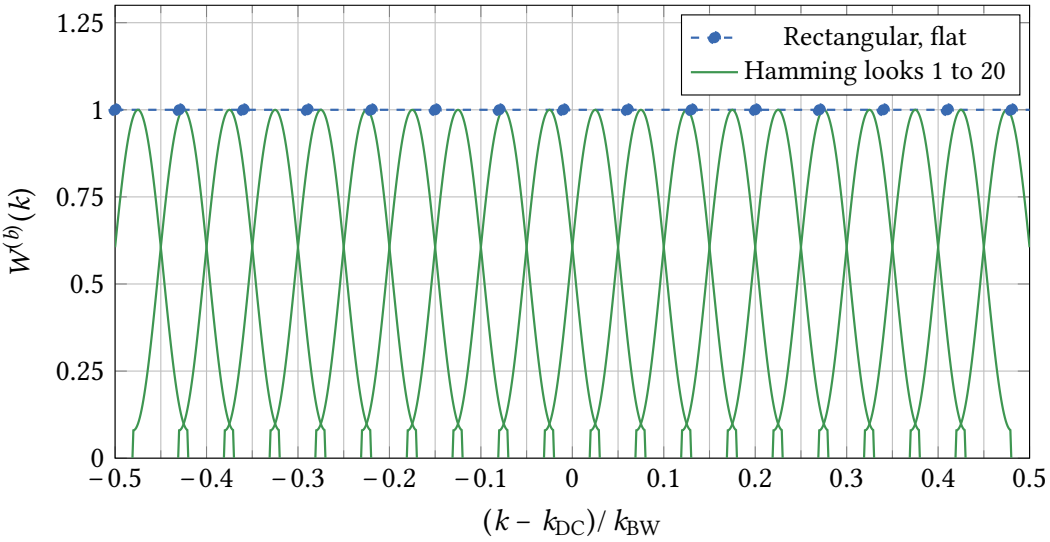


**Fig. 4.2:** Exemplary partially overlapping window functions with Hamming weighting for look generation over the full processed bandwidth.

interferograms, where, by design of the window functions, all interferograms can achieve the same sensitivity with respect to surface velocities. Under the assumption of a locally constant velocity — due to low surface acceleration or short acquisition time of the total processed Doppler bandwidth $k_{\mathrm{BW}}$ — the interferograms may be weighted by $t^{(b)}$ and coherently summed to remove biases and average speckle and non-coherent noise, while preserving the interferometric phase. The common multi-look processing scheme sums the looks with almost equal weights $\boldsymbol{t} \approx \mathbf{1}_B$, accounting only for the loss of SNR over the full processed Doppler bandwidth. This achieves optimum noise and speckle averaging and minimizes the estimation error if no coherent ambiguity biases are present [Por76; Cum05]. For high-performance missions or with worse CASR, the total estimation error of the interferometric

**Tab. 4.1:** Modulation of the CASR for the exemplary SAR system in Fig. 4.1 and 20 looks generated from Hamming window functions in Fig. 4.2

| Window function | Magnitude of CASR in dB | | | | | |
|---|---|---|---|---|---|---|
| | $\lvert\alpha_3\rvert$ | $\lvert\alpha_2\rvert$ | $\lvert\alpha_1\rvert$ | $\lvert\alpha_{-1}\rvert$ | $\lvert\alpha_{-2}\rvert$ | $\lvert\alpha_{-3}\rvert$ |
| Flat | −42.41 | −27.19 | −16.15 | −16.19 | −27.14 | −42.41 |
| Ham. look 1 | −33.58 | −20.31 | −8.88 | −14.92 | −25.55 | −33.58 |
| Ham. look 2 | −35.26 | −21.67 | −10.27 | −15.51 | −26.04 | −35.26 |
| Ham. look 3 | −37.25 | −23.27 | −11.86 | −16.25 | −26.67 | −37.25 |
| Ham. look 4 | −39.45 | −25.04 | −13.58 | −17.10 | −27.41 | −39.45 |
| Ham. look 5 | −41.99 | −27.07 | −15.49 | −18.11 | −28.31 | −41.99 |
| Ham. look 6 | −45.27 | −29.63 | −17.85 | −19.43 | −29.50 | −45.27 |
| Ham. look 7 | −49.45 | −32.79 | −20.63 | −21.05 | −30.94 | −49.45 |
| Ham. look 8 | −55.74 | −37.20 | −24.26 | −23.20 | −32.86 | −55.75 |
| Ham. look 9 | −66.71 | −45.37 | −30.04 | −26.45 | −35.67 | −66.71 |
| Ham. look 10 | −57.39 | −47.51 | −40.84 | −32.01 | −40.17 | −57.39 |
| Ham. look 11 | −52.60 | −39.18 | −32.35 | −41.12 | −49.61 | −52.60 |
| Ham. look 12 | −50.09 | −35.08 | −26.62 | −30.38 | −43.71 | −50.09 |
| Ham. look 13 | −48.61 | −32.45 | −23.31 | −24.46 | −36.44 | −48.61 |
| Ham. look 14 | −47.79 | −30.63 | −21.13 | −20.78 | −32.32 | −47.79 |
| Ham. look 15 | −47.42 | −29.25 | −19.50 | −17.97 | −29.30 | −47.42 |
| Ham. look 16 | −47.41 | −28.12 | −18.17 | −15.60 | −26.82 | −47.42 |
| Ham. look 17 | −47.76 | −27.25 | −17.14 | −13.67 | −24.85 | −47.76 |
| Ham. look 18 | −48.47 | −26.54 | −16.30 | −11.95 | −23.12 | −48.47 |
| Ham. look 19 | −49.66 | −25.94 | −15.56 | −10.31 | −21.55 | −49.66 |
| Ham. look 20 | −51.35 | −25.48 | −14.97 | −8.96 | −20.21 | −51.35 |

phase due to both speckle and noise as well as biases must be minimized, which results in optimum weights different from the commonly applied weights. In the following, the optimum weights that achieve a minimum total error are derived from a simplified interferometric data model and a linear minimum mean square error (LMMSE) technique.

The previous description may be realized in a simple way on stripmap scanned data, but does not restrict to this mode. For burst-based scanning modes, i.e. ScanSAR or TOPS, there is also a weighting in the spectrum due to the antenna pattern [Cumo5; De 06]. However, the removal algorithm must be adapted to fit to the scanning modes, i.e. removal must be specifically performed per burst and may depend on azimuth position. For TOPS, the generation of the looks must be integrated into the processing chain, when focusing is performed. Advantageously, the weighting by the antenna pattern is equal for all targets, but shifted in the spectrum [De 06]. Hence, if the window functions are correctly applied in the focusing step, the CASR becomes equal over the whole strip, as long as the antenna pattern is not deformed by the steering operation. A disadvantage is the shrinking of the antenna footprint due to active forward rotation of the steering, which corresponds to a virtually larger antenna length in a corresponding stripmap mode [De 06]. This might have an impact on the dynamic — difference in magnitude of largest to smallest CASR by modulation with windows — which is required for the proposed algorithm to work.

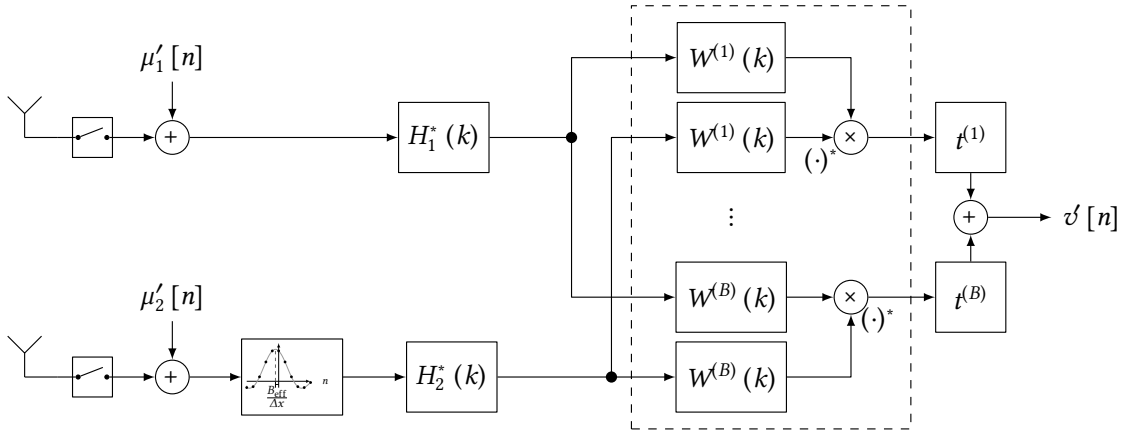


**Fig. 4.3:** Azimuth ambiguity removal with windowed interferograms, extends bistatic two-channel model in Fig. 2.7.

### 4.2.1 Along-Track Interferometric Signals with Modulations

The present section describes the signal model for the derivation of the algorithm under the previously made assumptions. Firstly, two SAR channels with a mutual along-track baseline are focused and the second channel is co-registered to the first channel as shown in Fig. 4.3. The azimuth spectra of the two images are separately weighted with different window functions $W^{(b)}(k)$. This produces a pair of images associated to each window function, i.e.,

$$\boldsymbol{u}^{(b)}[n] = \begin{bmatrix} u_1^{(b)}[n] + \mu_1^{(b)}[n] \\ u_2^{(b)}[n] + \mu_2^{(b)}[n] \end{bmatrix} = \beta_1^{(b)} \sum_{m=-M}^{M} \begin{bmatrix} \alpha_{1,m}^{(b)} \Gamma_m^{(b)}[n] \\ \beta_2^{(b)} \alpha_{2,m}^{(b)} \Gamma_m^{(b)}[n] \, \mathrm{e}^{-\mathrm{j}\phi_m} \end{bmatrix} + \begin{bmatrix} \mu_1^{(b)}[n] \\ \mu_2^{(b)}[n] \end{bmatrix}, \tag{4.1}$$

where $\mu_1[n]$ and $\mu_2[n]$ represent the noise contribution of the additive noise $\mu_1'[n]$ and $\mu_2'[n]$ after SAR processing, $m$ indexes the $2M+1$ different signal parts (with $m = 0$ being the main signal and $m \neq 0$ being the ambiguities), $\Gamma_m^{(b)}[n]$ denotes the complex reflectivity of the scene, $\phi_m$ is the interferometric phase, $\beta_1^{(b)}$ and $\beta_2^{(b)}$ are real-valued scaling factors and $\alpha_{1,m}^{(b)}$ and $\alpha_{2,m}^{(b)}$ are complex-valued factors such that $|\alpha_{1,m}^{(b)}|^2$ and $|\alpha_{2,m}^{(b)}|^2$ are ambiguity-to-signal-ratios of the $m$-th ambiguity for window function $b$ in images 1 and 2, respectively. How to find those scaling factors is summarized later in this section. Note, $\alpha_{1,m}^{(b)} \cdot \alpha_{2,m}^{(b)\,*} = \alpha_m^{(b)}$ as defined in (2.88), represents the CASR for window function $b$ in the interferogram

$$\upsilon^{(b)}[n] = \left( u_1^{(b)}[n] + \mu_1^{(b)}[n] \right) \left( u_2^{(b)}[n] + \mu_1^{(b)}[n] \right)^* . \tag{4.2}$$

From this interferogram, $2M$ ambiguities with their modulated ambiguity signature $\alpha_m^{(b)}$ shall be removed.

The scene signal is modeled as a zero-mean complex Gaussian process [War13, pp. 289–307], i.e.,

$$\Gamma_m^{(b)}[n] \sim \mathcal{CN}\left(0,\, \sigma_m^0\right), \tag{4.3}$$

with cross-correlation

$$\mathrm{E}\left[I_{m_1}^{(b_1)}[n_1] I_{m_2}^{(b_2)^*}[n_2]\right] = \sigma_{m_1}^0 \delta_{m_1 m_2} \delta_{b_1 b_2} \delta_{n_1 n_2} \tag{4.4}$$

$$\mathrm{E}\left[\mu_i^{(b_1)}[n_1] \mu_j^{(b_2)^*}[n_2]\right] = P_{\mathrm{N}_i}^{(b_1)} \delta_{ij} \delta_{b_1 b_2} \delta_{n_1 n_2}\,, \tag{4.5}$$

where the Kronecker delta $\delta_{ij}$ was used. The first condition related to $m_1$ and $m_2$ applies in general because of different spectral support of the ambiguities, that makes them uncorrelated [Has85]; the second condition only holds if the windows do not share any common spectral support; the last condition is true for white noise-like scenes and infinitely large processed Doppler bandwidth, that results in a Dirac delta shaped azimuth auto-correlation. The same is later applied to the range auto-correlation function as well. The two additive noise components are also zero mean proper complex Gaussian distributed with variances $P_{\mathrm{N}_1}^{(b)}$ and $P_{\mathrm{N}_2}^{(b)}$ and identical assumptions on cross-correlation. The third condition can not be fulfilled in general, because the Doppler bandwidth is always finite, which results in a sinc-shaped auto-correlation function. But, those assumptions simplify the algorithm formulation under negligible performance reduction, as shown later.

The algorithm combines samples from $B$ different interferograms. In general, the interferograms may have different azimuth resolutions $\Delta_b$ due to the windowing. For the sake of simplicity, an equalization of the azimuth resolution by applying a boxcar pre-averaging of $Q^{(b)}$ samples per range line is conducted.

Then, $N$ samples in range direction are stacked into an interferogram data vector

$$\boldsymbol{v}^{(b)}[n] = \frac{1}{Q^{(b)}} \sum_{q=1}^{Q^{(b)}} \begin{bmatrix} v^{(b)}[n + q\Delta_b, 1] \\ \vdots \\ v^{(b)}[n + q\Delta_b, N] \end{bmatrix} \in \mathbb{C}^{N\times 1}\,, \tag{4.6}$$

such that at most $N_{\mathrm{tot}} = N \max\left\{ Q^{(1)}, Q^{(2)}, \dots, Q^{(B)} \right\}$ samples are incorporated in the algorithm. Finally, all $B$ interferogram data vectors are stacked to form the total interferogram vector

$$\boldsymbol{v}[n] = \begin{bmatrix} \boldsymbol{v}^{(1)}[n] \\ \vdots \\ \boldsymbol{v}^{(B)}[n] \end{bmatrix} \in \mathbb{C}^{BN\times 1}\,. \tag{4.7}$$

The expected interferometric data

$$\mathrm{E}\left[\boldsymbol{v} \,\middle|\, \sigma^0, \phi\right] = \boldsymbol{A}\boldsymbol{s} \in \mathbb{C}^{BN\times 1} \tag{4.8}$$

consists of the ambiguity matrix

$$\boldsymbol{A} = \begin{bmatrix} {\beta_1^{(1)}}^2 \beta_2^{(1)} \alpha_{-M}^{(1)} & \cdots & {\beta_1^{(1)}}^2 \beta_2^{(1)} & \cdots & {\beta_1^{(1)}}^2 \beta_2^{(1)} \alpha_{M}^{(1)} \\ \vdots & & \vdots & & \vdots \\ {\beta_1^{(B)}}^2 \beta_2^{(B)} \alpha_{-M}^{(B)} & \cdots & {\beta_1^{(B)}}^2 \beta_2^{(B)} & \cdots & {\beta_1^{(B)}}^2 \beta_2^{(B)} \alpha_{M}^{(B)} \end{bmatrix} \otimes \mathbf{1}_N \in \mathbb{C}^{BN\times 2M+1}\,, \tag{4.9}$$

where $\otimes$ denotes the Kronecker product, and the vector of interferometric properties (3.5). The ambiguity matrix is composed of power factors and the CASR per interferogram. From $\boldsymbol{s}$ is only $\sigma_0^0\, \mathrm{e}^{\mathrm{j}\phi_0}$ of interest. The other parameters contain information about the interferometric parameters of all ambiguities.

### 4.2.2 Algorithm Formulation

The interferograms are combined in terms of a LMMSE estimator

$$\hat{\tilde{\boldsymbol{s}}} = \tilde{\boldsymbol{T}}\tilde{\boldsymbol{v}} + \tilde{\boldsymbol{m}} \in \mathbb{C}^{2(2M+1)\times 1}\,, \tag{4.10}$$

which minimizes the mean square error (MSE) [Wie49]

$$\tilde{\boldsymbol{T}}, \tilde{\boldsymbol{m}} = \arg\min_{\tilde{\boldsymbol{T}},\tilde{\boldsymbol{m}}} \mathrm{E}\left[\left\|\tilde{\boldsymbol{s}} - \tilde{\boldsymbol{T}}\tilde{\boldsymbol{v}} - \tilde{\boldsymbol{m}}\right\|^2\right] = \arg\min_{\tilde{\boldsymbol{T}},\tilde{\boldsymbol{m}}} \mathrm{E}\left[\left\|\tilde{\boldsymbol{s}} - \tilde{\boldsymbol{T}}\left(\tilde{\boldsymbol{A}}\tilde{\boldsymbol{s}} + \tilde{\boldsymbol{\nu}}\right) - \tilde{\boldsymbol{m}}\right\|^2\right], \tag{4.11}$$

where augmented vectors, i.e.,

$$\tilde{\boldsymbol{a}} = \begin{bmatrix} \boldsymbol{a} \\ \boldsymbol{a}^* \end{bmatrix} \tag{4.12}$$

are introduced to consider the improper (non-circular) distribution of the complex interferogram. Description and processing of such signals can be found in the literature [Sch10, pp. 31–40]. Within the definition of the MSE, the interferometric data is split into its expected value and variations of the data about its expected value due to thermal noise and speckle [Jus94]. All those variations are combined into an additive pseudo noise vector

$$\tilde{\boldsymbol{\nu}} = \tilde{\boldsymbol{v}} - \tilde{\boldsymbol{A}}\tilde{\boldsymbol{s}} \in \mathbb{C}^{2BN\times 1}\,. \tag{4.13}$$

The estimator is then found to be

$$\tilde{\boldsymbol{T}} = \tilde{\boldsymbol{C}}_{\tilde{s}\tilde{s}}\tilde{\boldsymbol{A}}^{\mathrm{H}}\left(\tilde{\boldsymbol{A}}\tilde{\boldsymbol{C}}_{\tilde{s}\tilde{s}}\tilde{\boldsymbol{A}}^{\mathrm{H}} + \tilde{\boldsymbol{C}}_{\tilde{\nu}\tilde{\nu}}\right)^{-1} \tag{4.14}$$

$$\tilde{\boldsymbol{m}} = \mathrm{E}[\tilde{\boldsymbol{s}}] - \tilde{\boldsymbol{T}}\tilde{\boldsymbol{A}}\,\mathrm{E}[\tilde{\boldsymbol{s}}]\,, \tag{4.15}$$

where $(\cdot)^{\mathrm{H}}$ denotes the matrix conjugate transpose or Hermitian transpose, and

$$\tilde{\boldsymbol{C}}_{\tilde{s}\tilde{s}} = \mathrm{E}\left[\left(\tilde{\boldsymbol{s}} - \mathrm{E}[\tilde{\boldsymbol{s}}]\right)\left(\tilde{\boldsymbol{s}} - \mathrm{E}[\tilde{\boldsymbol{s}}]\right)^{\mathrm{H}}\right] \in \mathbb{C}^{2(2M+1)\times 2(2M+1)} \tag{4.16}$$

is the covariance matrix for the vector of interferometric properties $\tilde{\boldsymbol{s}}$ and

$$\tilde{\boldsymbol{C}}_{\tilde{\nu}\tilde{\nu}} = \mathrm{E}\left[\tilde{\boldsymbol{\nu}}\tilde{\boldsymbol{\nu}}^{\mathrm{H}}\right] = \mathrm{E}\left[\mathrm{E}\left[\tilde{\boldsymbol{\nu}}\tilde{\boldsymbol{\nu}}^{\mathrm{H}} \mid \tilde{\boldsymbol{s}}\right]\right] \in \mathbb{C}^{2BN\times 2BN} \tag{4.17}$$

is the covariance matrix of the zero-mean pseudo noise vector $\tilde{\boldsymbol{\nu}}$ averaged over the prior distributions of the interferometric parameters $\tilde{\boldsymbol{s}}$.

The covariance matrix $\tilde{\boldsymbol{C}}_{\tilde{s}\tilde{s}}$ depends on characteristics of the sea state, i.e. shown in Tab. 3.1, and is found by calculating the second moments of the associated prior distributions

$$\tilde{\boldsymbol{C}}_{\tilde{s}\tilde{s}} = \begin{bmatrix} \mathrm{E}\left[\left|\sigma^0\,\mathrm{e}^{\mathrm{j}\phi} - \mathrm{E}[\sigma^0\,\mathrm{e}^{\mathrm{j}\phi}]\right|^2\right] & \mathrm{E}\left[\left(\sigma^0\,\mathrm{e}^{\mathrm{j}\phi} - \mathrm{E}[\sigma^0\,\mathrm{e}^{\mathrm{j}\phi}]\right)^2\right] \\ \mathrm{E}\left[\left(\sigma^0\,\mathrm{e}^{\mathrm{j}\phi} - \mathrm{E}[\sigma^0\,\mathrm{e}^{\mathrm{j}\phi}]\right)^2\right]^* & \mathrm{E}\left[\left|\sigma^0\,\mathrm{e}^{\mathrm{j}\phi} - \mathrm{E}[\sigma^0\,\mathrm{e}^{\mathrm{j}\phi}]\right|^2\right] \end{bmatrix} \otimes \boldsymbol{I}_{2M+1}\,, \tag{4.18}$$

where

$$\mathrm{E}\left[\left|\sigma^0\,\mathrm{e}^{\mathrm{j}\phi} - \mathrm{E}[\sigma^0\,\mathrm{e}^{\mathrm{j}\phi}]\right|^2\right] = \mathrm{Var}[\sigma^0] + \left(1 - \left|\mathrm{E}[\mathrm{e}^{\mathrm{j}\phi}]\right|^2\right)\mathrm{E}[\sigma^0]^2 \tag{4.19}$$

$$\mathrm{E}\left[\left(\sigma^0\,\mathrm{e}^{\mathrm{j}\phi} - \mathrm{E}[\sigma^0\,\mathrm{e}^{\mathrm{j}\phi}]\right)^2\right] = \mathrm{Var}[\sigma^0]\,\mathrm{E}[\mathrm{e}^{\mathrm{j}2\phi}] + \left(\mathrm{E}[\mathrm{e}^{\mathrm{j}2\phi}] - \mathrm{E}[\mathrm{e}^{\mathrm{j}\phi}]^2\right)\mathrm{E}[\sigma^0]^2 \tag{4.20}$$

and $\boldsymbol{I}_N$ is the $N \times N$ identity matrix. It is assumed, that all $2M + 1$ interferometric properties are identically independently distributed, following the same reasoning used in Chapter 3. A correlation between scattering coefficient $\sigma_m^0$ and interferometric phase $\phi_m$ of ambiguity $m$, due to the orbital motion of water particles because of swell [Has85], is neglected. This relation may later be leveraged to ease the estimation.

The averaged covariance matrix of the pseudo noise vector is first divided into block sub-matrices

$$\tilde{\boldsymbol{C}}_{\tilde{\boldsymbol{\nu}}\tilde{\boldsymbol{\nu}}} = \begin{bmatrix} \mathrm{Cov}\left[\boldsymbol{\nu}\boldsymbol{\nu}^{\mathrm{H}}\right] & \mathrm{Cov}\left[\boldsymbol{\nu}\boldsymbol{\nu}^{\mathrm{T}}\right] \\ \mathrm{Cov}\left[\boldsymbol{\nu}\boldsymbol{\nu}^{\mathrm{T}}\right]^* & \mathrm{Cov}\left[\boldsymbol{\nu}\boldsymbol{\nu}^{\mathrm{H}}\right]^* \end{bmatrix}. \tag{4.21}$$

To find the block sub-matrices, which requires the evaluation of the fourth moments of random variables, i.e. $\Gamma_m^{(b)}[n]$, Iserli's theorem is applied to reduce the total expectation into paired partitions of expectations. A summary may be found in [Bau14, pp. 713–717], here, one uses

$$\mathrm{E}[X_1X_2X_3X_4] = \mathrm{E}[X_1X_2]\,\mathrm{E}[X_3X_4] + \mathrm{E}[X_1X_3]\,\mathrm{E}[X_2X_4] + \mathrm{E}[X_1X_4]\,\mathrm{E}[X_2X_3] \tag{4.22}$$

and

$$\mathrm{E}[X_1X_2X_3] = 0\,, \tag{4.23}$$

where $X_1$ to $X_4$ are zero-mean complex Gaussian random variables and may have arbitrary conjugations, i.e. $X_3 = X_1^*$. After many algebraic reformulations and by using Iserli's theorem and the assumptions (4.4) and (4.5), one finds the sub-covariance matrices

$$\begin{aligned}\mathrm{Cov}[\boldsymbol{\nu}\boldsymbol{\nu}^{\mathrm{H}}] = &\left(\left\{\sum_{i=-M}^{M}\left[\sum_{m=-M}^{M}\mathrm{E}[\sigma_i^0\sigma_m^0]\begin{bmatrix} \frac{\beta_1^{(1)4}\beta_2^{(1)2}}{Q^{(1)}}\left|\alpha_{1,i}^{(1)}\right|^2\left|\alpha_{2,m}^{(1)}\right|^2 & \cdots & 0 \\ \vdots & \ddots & \vdots \\ 0 & \cdots & \frac{\beta_1^{(B)4}\beta_2^{(B)2}}{Q^{(B)}}\left|\alpha_{1,i}^{(B)}\right|^2\left|\alpha_{2,m}^{(B)}\right|^2 \end{bmatrix}\right]\right. \\ &\left. + \mathrm{E}[\sigma_i^0]\begin{bmatrix} \frac{\beta_1^{(1)2}}{Q^{(1)}}\left(\left|\alpha_{1,i}^{(1)}\right|^2 P_{\mathrm{N}_2}^{(1)} + \beta_2^{(1)2}\left|\alpha_{2,i}^{(1)}\right|^2 P_{\mathrm{N}_1}^{(1)}\right) & \cdots & 0 \\ \vdots & \ddots & \vdots \\ 0 & \cdots & \frac{\beta_1^{(B)2}}{Q^{(B)}}\left(\left|\alpha_{1,i}^{(B)}\right|^2 P_{\mathrm{N}_2}^{(B)} + \beta_2^{(B)2}\left|\alpha_{2,m}^{(B)}\right|^2 P_{\mathrm{N}_1}^{(B)}\right) \end{bmatrix}\right\} \\ &+ \begin{bmatrix} \frac{P_{\mathrm{N}_1}^{(1)}P_{\mathrm{N}_2}^{(1)}}{Q^{(1)}} & \cdots & 0 \\ \vdots & \ddots & \vdots \\ 0 & \cdots & \frac{P_{\mathrm{N}_1}^{(B)}P_{\mathrm{N}_2}^{(B)}}{Q^{(B)}} \end{bmatrix}\end{bmatrix} \otimes \boldsymbol{I}_N \end{aligned} \tag{4.24}$$

and

$$\mathrm{Cov}\left[\boldsymbol{\nu}\boldsymbol{\nu}^{\mathrm{T}}\right] = \sum_{i=-M}^{M}\sum_{m=-M}^{M} \mathrm{E}[\sigma_i^0\sigma_m^0]\,\mathrm{E}\left[\mathrm{e}^{\mathrm{j}(\phi_i+\phi_m)}\right] \begin{bmatrix} \frac{\beta_1^{(1)^4}\beta_2^{(1)^2}}{Q^{(1)}}\alpha_i^{(1)}\alpha_m^{(1)} & \cdots & 0 \\ \vdots & \ddots & \vdots \\ 0 & \cdots & \frac{\beta_1^{(B)^4}\beta_2^{(B)^2}}{Q^{(B)}}\alpha_i^{(B)}\alpha_m^{(B)} \end{bmatrix} \otimes \boldsymbol{I}_N\,. \tag{4.25}$$

In a last step, the parameters of the augmented covariance matrix, i.e. power factors, CASR and noise power must be found. They can be found from knowledge of the antenna pattern and system attitude parameters and must be refined from calibration measurements on ground and during operation. The following steps show, how they are found from antenna pattern and system attitude parameters, which provides full knowledge of those parameters for simulation. The influence of calibration and therefore not fully known parameters is neglected. The CASR was already derived in Section 2.4.3 and used in the derivation of (4.24) and (4.25). Similarly, one finds the ambiguity-to-signal-ratios on image level

$$\left|\alpha_{z,m}^{(b)}\right|^2 = \frac{\int_{k_{\mathrm{DC}}+\frac{2\pi m}{\Delta x}-\frac{k_{\mathrm{BW}}}{2}}^{k_{\mathrm{DC}}+\frac{2\pi m}{\Delta x}+\frac{k_{\mathrm{BW}}}{2}} \left|H_z\left(k'\right)M_z^{(b)}\left(k'-\frac{2\pi m}{\Delta x}\right)\right|^2 \mathrm{d}k'}{\int_{k_{\mathrm{DC}}-\frac{k_{\mathrm{BW}}}{2}}^{k_{\mathrm{DC}}+\frac{k_{\mathrm{BW}}}{2}} \left|H_z(k')M_z^{(b)}(k')\right|^2 \mathrm{d}k'}\,, \tag{4.26}$$

with $z$ indexing the respective channel. The power factors $\beta_1^{(b)}$ denote the radiometric sensitivity of the system for each interferogram, which may be related to the first window function $b = 1$

$$\beta_1^{(1)^2} = \frac{\mathrm{Var}\left[u_1^{(1)}[n]\,\middle|\,\sigma^0\right]}{\sigma^0\sum_{m=-\infty}^{\infty}\left|\alpha_{1,m}^{(1)}\right|^2} \tag{4.27}$$

by

$$\left(\frac{\beta_1^{(b)}}{\beta_1^{(1)}}\right)^2 = \frac{\int_{k_{\mathrm{DC}}+\frac{2\pi m}{\Delta x}-\frac{k_{\mathrm{BW}}}{2}}^{k_{\mathrm{DC}}+\frac{2\pi m}{\Delta x}+\frac{k_{\mathrm{BW}}}{2}} \left|H_1\left(k'\right)M_1^{(b)}\left(k'\right)\right|^2 \mathrm{d}k'}{\int_{k_{\mathrm{DC}}-\frac{k_{\mathrm{BW}}}{2}}^{k_{\mathrm{DC}}+\frac{k_{\mathrm{BW}}}{2}} \left|H_1(k')M_1^{(1)}(k')\right|^2 \mathrm{d}k'}\,, \tag{4.28}$$

if only the main signal is present. The power ratio between images 1 and 2 is found similarly

$$\beta_2^{(b)} = \frac{\int_{k_{\mathrm{DC}}+\frac{2\pi m}{\Delta x}-\frac{k_{\mathrm{BW}}}{2}}^{k_{\mathrm{DC}}+\frac{2\pi m}{\Delta x}+\frac{k_{\mathrm{BW}}}{2}} \left|H_2\left(k'\right)M_2^{(b)}\left(k'\right)\right|^2 \mathrm{d}k'}{\int_{k_{\mathrm{DC}}-\frac{k_{\mathrm{BW}}}{2}}^{k_{\mathrm{DC}}+\frac{k_{\mathrm{BW}}}{2}} \left|H_1(k')M_1^{(b)}(k')\right|^2 \mathrm{d}k'}\,. \tag{4.29}$$

The noise power equals the imaged power of a scene with scattering coefficient $\sigma^0_{\mathrm{NE}}$ for a reference flat window $b = 1$

$$P^{(1)}_{\mathrm{N}_1} = \mathrm{Var}\left[ u^{(1)}_1[n] \,\middle|\, \sigma^0 = \sigma^0_{\mathrm{NE}} \right] = {\beta^{(1)}_1}^2 \sigma^0_{\mathrm{NE}} \sum_{m=-\infty}^{\infty} \left| \alpha^{(1)}_{1,m} \right|^2 \tag{4.30}$$

and similarly for channel 2

$$P^{(1)}_{\mathrm{N}_2} = \mathrm{Var}\left[ u^{(1)}_2[n] \,\middle|\, \sigma^0 = \sigma^0_{\mathrm{NE}} \right] = \left( \beta^{(1)}_1 \beta^{(1)}_2 \right)^2 \sigma^0_{\mathrm{NE}} \sum_{m=-\infty}^{\infty} \left| \alpha^{(1)}_{2,m} \right|^2 . \tag{4.31}$$

If a different window function is used the noise power must be scaled by the ratio

$$\frac{P^{(b)}_{\mathrm{N}_z}}{P^{(1)}_{\mathrm{N}_z}} = \frac{\int_{k_{\mathrm{DC}}+\frac{2\pi m}{\Delta x}-\frac{k_{\mathrm{BW}}}{2}}^{k_{\mathrm{DC}}+\frac{2\pi m}{\Delta x}+\frac{k_{\mathrm{BW}}}{2}} \left| M^{(b)}_z\left(k' - \frac{2\pi m}{\Delta x}\right) \right|^2 \mathrm{d}k'}{\int_{k_{\mathrm{DC}}-\frac{k_{\mathrm{BW}}}{2}}^{k_{\mathrm{DC}}+\frac{k_{\mathrm{BW}}}{2}} \left| M^{(1)}_z(k') \right|^2 \mathrm{d}k'} , \tag{4.32}$$

because the additive noise is assumed to be white.

## 4.3 Interferometric Performance of Coherent Ambiguity Removal

The evaluation of the interferometric performance bases on the model configuration as given in Tab. A.1 in the Appendix, which yields the exemplary magnitude weighting as shown in Fig. 4.1.

### 4.3.1 Demonstration of LMMSE Look Combination

In this section, the improvement of interferometric performance by combining windowed interferograms under a LMMSE condition is discussed. Fig. 4.4 shows the interferometric performance of all single windowed interferograms and after combination using the LMMSE technique, as well as the CRB (3.7) as a reference of optimum performance with completely removed biases.

The best performing single interferogram uses a window function ($b = 10$ or $b = 11$) centered at the Doppler centroid, where the best CASR is achieved as shown in Tab. 4.1. However, it does not process the complete available bandwidth and has therefore less independent samples for noise averaging. This results in a loss of interferometric performance by a factor of 3.75 at 100 samples compared to the performance of the uncorrected interferogram. The uncorrected interferogram, which is generated with a flat window function over the full processed Doppler bandwidth, achieves best results for low numbers of samples, but has a worse CASR than the best performing windowed interferogram at large numbers of samples.

The LMMSE technique combines the information from all windowed interferograms. For low numbers of samples, the interferometric performance is equal to the performance of the uncorrected interferogram. One finds by observing the weights $\boldsymbol{t}$, that the LMMSE algorithm is only multi-look processing the interferogram [Por76]. The biases by coherent ambiguities come into relevance for larger numbers of samples, because random errors by noise are suppressed. One observes varying levels

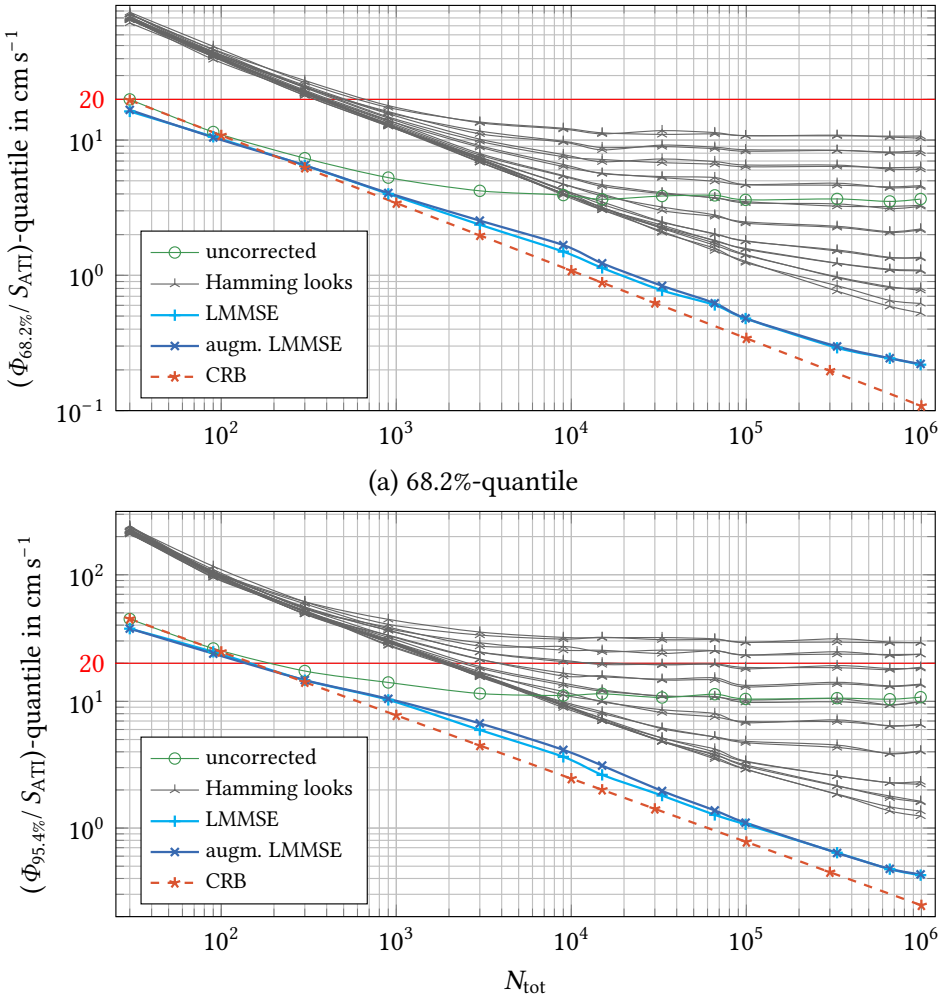


**Fig. 4.4**: Velocity estimation error for ocean in Douglas sea state 6 using interferograms with applied window functions and the LMMSE combination of interferograms to multi-look and remove biases by ambiguities. The CRB for the unbiased phase estimator is given as reference.

of biases in the single interferograms, due to the modulation of the CASR by the applied windows. The LMMSE algorithm adapts the weights $\boldsymbol{t}$, to trade-off systematic and random errors, such that the MSE is minimal. The trade-off is experienced at a slight deterioration from the CRB above of $10^3$ samples, because the adaptation of weights $\boldsymbol{t}$ to remove biases occurs at the expense of less averaging of the inherent noise.

At 990 000 samples, the effect of simulation model-induced biases is observable, compare Fig. 3.4. An analysis of the algorithms beyond these numbers of samples is not possible.

From simulations with different overlapping and non-overlapping window functions, it is found, that the CRB for low numbers of samples is achieved by non-overlapping window functions. Overlapping window functions increase the interferometric phase error, because their samples are partially correlated, which was not considered in the algorithm derivation. However, the simulations showed,

**Tab. 4.2:** Improvement of interferometric performance related to the uncorrected interferogram by coherent ambiguity removal algorithms on interferogram level for reference product resolution of Harmony 1.2 km×1.2 km (15 000 samples)

| Douglas | IIR equalizer | | LMMSE | | augm. LMMSE | |
|---|---|---|---|---|---|---|
| sea state | 68.2% | 95.4% | 68.2% | 95.4% | 68.2% | 95.4% |
| 6 | 4.05 | 5.53 | 3.22 | 4.37 | 2.97 | 3.69 |
| 5 | 2.34 | 2.62 | 2.04 | 2.36 | 1.91 | 1.97 |
| 2 | 1.14 | 1.17 | 1.07 | 1.10 | 1.16 | 1.19 |

that the trade-off may be reduced with overlapping window functions at larger numbers of averaging samples. The choice of window functions is subject to detailed analysis, when implementing the algorithm on real data.

### 4.3.2 Algorithm comparison

The prior information incorporated in the LMMSE algorithm achieves an advantage in the case of low SNR (low sea state) and low numbers of samples. However, the interferometric phase error exceeds the requirements and can not contribute to achieving this goal. Note, that the 20 cm/s are errors on ground and the interferometric performance is with respect to line-of-sight direction. The Harmony mission targets product resolutions between 1 $km^2$ to 25 $km^2$ ($10^4$ to $25 \cdot 10^4$ samples) to achieve the scientific requirements [Rom20]. In this range, coherent azimuth ambiguities show a biasing effect on interferometric performance. Both, the IIR equalizer and the presented LMMSE algorithm can remove this effect. However, the CRB, representing the optimum (best achievable) performance, is not achieved by any of both. The IIR algorithm scales the thermal noise by adding shifted versions of the interferogram, resulting in a lower coherence and larger phase variance. One sees, that the LMMSE algorithm can not achieve the performance of the IIR equalizer, especially in the case where biases are dominant. I.e., in the highest simulated sea state 6 and 15 000 samples, the LMMSE algorithm needs a factor of 1.61 times more samples to achieve the interferometric performance of the IIR equalizer. For high sea states, compare Fig. 4.5 (a), the augmented LMMSE algorithm shows a small deviation to the simpler LMMSE algorithm in the range of 900 to 66 000 samples. This may be a result of the assumptions and simplifications made when developing the algorithms, whereby most of the correlations between samples are neglected. One may use the LMMSE algorithm for these numbers of samples and when the DPCA condition is fulfilled. For 990 000 samples and high sea states, the model-induced biases impact the estimation for both the IIR equalizer and the LMMSE technique.

Tab. 4.2 summarizes the simulated interferometric performance improvement for the reference product resolution, corresponding to 15 000 samples. In a sea state 6 case, the interferometric performance of the (augmented) LMMSE is worse than the performance of the IIR equalizer, due to the bias-variance trade-off. For the lowest simulated sea state 2, the performance is comparable or better, because the effect of coherent ambiguities is not the dominating error source and only random errors must be minimized. To achieve a similar performance improvement in sea states 2 and 5 compared to sea state 6 at reference product resolution, there are 603 891 and 65 920 samples required, respectively. This improvement may be realized for sea state 5, but for sea state 2, more samples are needed, than offered by the available product resolution range of the Harmony mission.

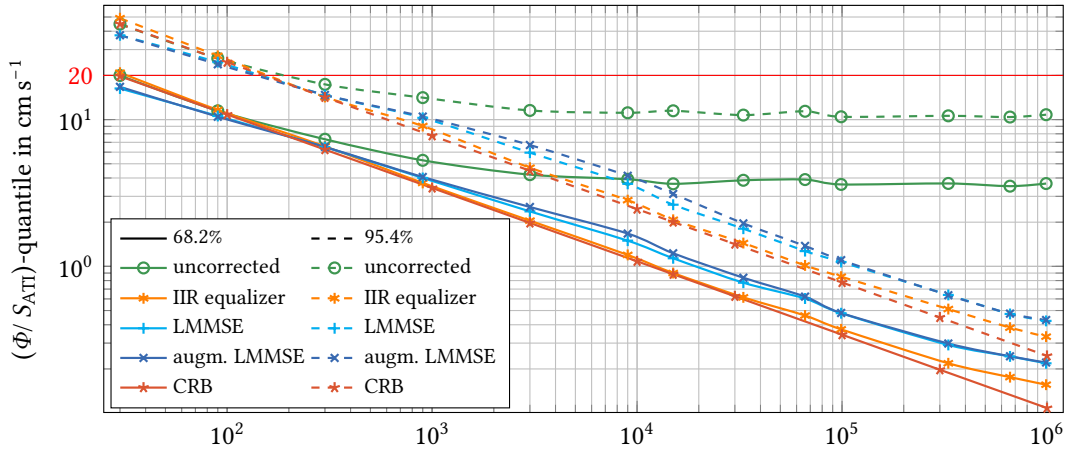


(a) Douglas sea state 6: Wind speed of 15.23 m/s, $\mathrm{E}\left[\sigma^0\right] = -5.9$ dB

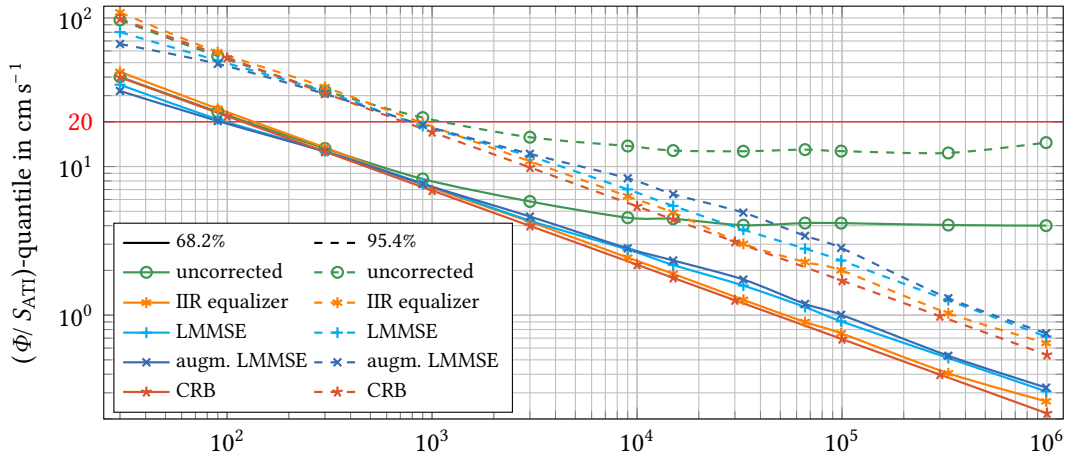


(b) Douglas sea state 5: Wind speed of 10.53 m/s, $\mathrm{E}\left[\sigma^0\right] = -11.8$ dB

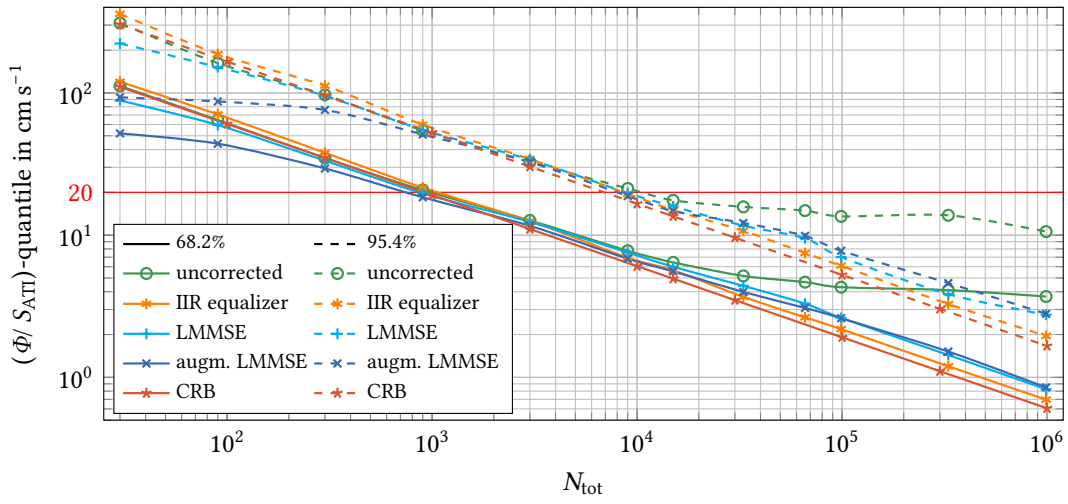


(c) Douglas sea state 2: Wind speed of 3.78 m/s, $\mathrm{E}\left[\sigma^0\right] = -19.7$ dB

**Fig. 4.5**: Interferometric performance of ATI system with azimuth ambiguity removal by LMMSE combination of looks over number of averaged samples and a noise level of $\sigma^0_{\mathrm{NE}} = -20.5$ dB.

Fig. 4.6 shows results for a 97.5% and 75.0% fulfilled DPCA condition. The augmented LMMSE algorithm is least impacted by a not fulfilled DPCA condition. The algorithm leverages the non-circular property of the interferometric data samples to separate ambiguous and main signal components. Especially in the 75% case, the probability distributions of the main part and the two first ambiguities are maximally separated due to the ±90° additional interferometric phase offset per ambiguity. The loss of coherence due to coherent ambiguities [Vil12], which is observable for the IIR equalizer and the unbiased CRB, is circumvented by the augmented LMMSE algorithm. The simulation shows, that it achieves better interferometric performance than the IIR equalizer, although it has to trade off bias and variance.

The overall degradation of the CRB with deviation from the DPCA condition validates the assumption from Section 2.4.3 and observations [Lóp21], that the interferometric phase bias should be zero to minimize the loss of coherence and improve the interferometric performance. However, the DPCA condition may not always be fulfilled, i.e. over the full swath. In those cases, the augmented LMMSE algorithm should be utilized.

The sensitivity of IIR equalizer and (augmented) LMMSE algorithms concerning calibration errors of baseline and antenna pattern is analyzed in an associated paper [Ric22]. The results are not stated again, but considered for drawing conclusions at the end of this work.

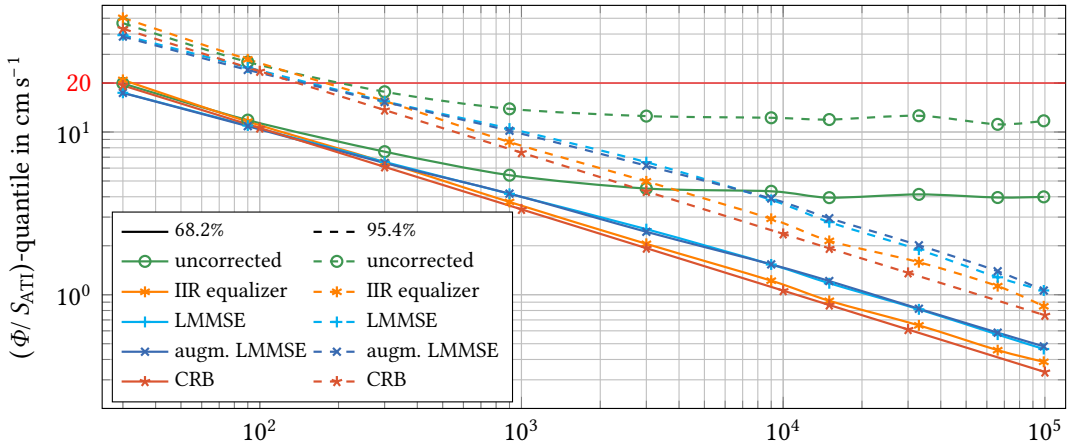


(a) Douglas sea state 6: Wind speed of 15.23 m/s, $\mathrm{E}\left[\sigma^0\right] = -5.9$ dB and 97.5% of DPCA condition fulfilled

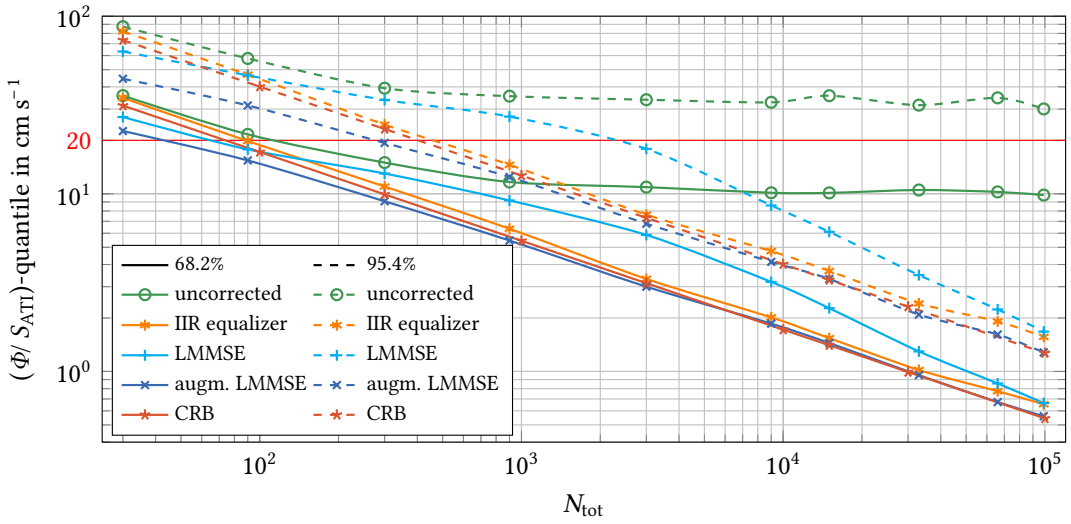


(b) Douglas sea state 6: Wind speed of 15.23 m/s, $\mathrm{E}\left[\sigma^0\right] = -5.9$ dB and 75.0% of DPCA condition fulfilled

**Fig. 4.6**: Interferometric performance of ATI system over number of averaged samples and a noise level of $\sigma^0_{\mathrm{NE}} = -20.5$ dB with not fulfilled DPCA condition.

# 5 Multi-Channel Estimation

The Harmony satellites will carry three antennas with independent hardware, hence three channels can be formed, which feature mutual along-track baselines, compare Fig. 2.2. A pair of images generated from those channels can be interferometrically processed and ambiguities removed as described in the previous chapter. Since the Harmony mission shall perform highly accurate measurements of scientific parameters, a goal is to increase interferometric performance with all observed data. In this chapter, the improvement made with multi-channel measurements is theoretically analyzed and algorithms for ambiguity removal based on harmonic analysis are described and evaluated. Of course, one could implement algorithms that are based on minimizing the MSE as done for two channels. But, any algorithm using the scheme from Chapter 4 requires accurate knowledge of each modulated CASR. This chapter focuses on techniques, i.e. similar to a Fourier transform, that can estimate the main signal component without depending on this knowledge. Such techniques are already applied in tomographic processing to separate different scattering phase center positions, i.e. multiple signal classification (MUSIC) and minimum variance distortionless response (MVDR) [Fre10], and are analyzed with respect to their ambiguity removal capabilities.

## 5.1 Optimum Estimation Performance of Multi-Channel Acquisitions

Before introducing the algorithms, the optimum performance for estimating interferometric phases from multi-channel acquisitions (> 2 channels) is of interest. In this section, an equation for the unbiased[3] CRB using $Z$ channels as shown in Fig. 5.1 is derived. With this result, the expected reduction of the CRB using multiple channels is given in general and discussed with respect to the Harmony mission.

### 5.1.1 General Expression of Optimum Estimation Performance

Multi-channel acquisitions of fully developed speckle of ocean and sea surfaces yields jointly complex Gaussian distributed images $\boldsymbol{u}$ with probability density function [War13, pp. 289–307] [Has85]

$$f\left(\boldsymbol{u}[n] \,\middle|\, v_\mathrm{r}\right) = \frac{1}{\pi \det\left(\boldsymbol{C}(v_\mathrm{r})\right)} \mathrm{e}^{-\boldsymbol{u}^\mathrm{H}[n]\boldsymbol{C}^{-1}(v_\mathrm{r})\boldsymbol{u}[n]}, \tag{5.1}$$

where $v_\mathrm{r}$ is the constant radial velocity of the scene and $\boldsymbol{u}[n]$ being samples from the $Z$ focused and co-registered images and $\det\left(\boldsymbol{C}(v_\mathrm{r})\right)$ is the determinant of the covariance matrix

$$\boldsymbol{C}(v_\mathrm{r}) = \mathrm{E}\left[\boldsymbol{u}[n]\boldsymbol{u}^\mathrm{H}[n]\right] = \begin{bmatrix} \sigma_1^2 & \gamma_{12}\sigma_1\sigma_2 & \cdots & \gamma_{1Z}\sigma_1\sigma_Z \\ \gamma_{12}^*\sigma_1\sigma_2 & \sigma_2^2 & \cdots & \gamma_{2Z}\sigma_2\sigma_Z \\ \vdots & \vdots & \ddots & \vdots \\ \gamma_{1Z}^*\sigma_1\sigma_Z & \gamma_{2Z}^*\sigma_2\sigma_Z & \cdots & \sigma_Z^2 \end{bmatrix}, \tag{5.2}$$

3 In this context, *unbiased* refers to an underlying signal model without the presence of coherent ambiguities

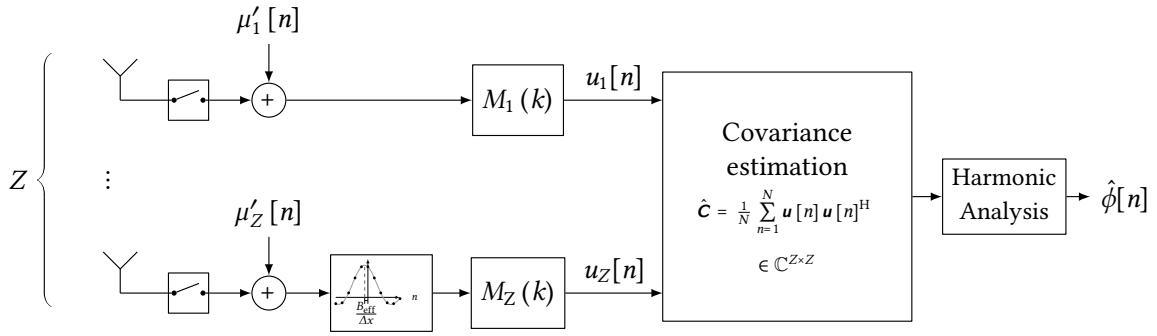


**Fig. 5.1**: Interferometric phase estimation and ambiguity removal from multi-channel acquisitions.

where $\sigma_z^2$ denotes the power of channel $z$. The cross-correlation coefficients between arbitrary ATI channels $i$ and $j$ are of the form [Gol87]

$$\gamma_{ij} = \left|\gamma_{ij}\right| \mathrm{e}^{\mathrm{j}\frac{2\pi}{\lambda} B_{\mathrm{ATI},ij} L_{\mathrm{d}} L_{\mathrm{g,tot}} \frac{v_{\mathrm{r}}}{v_{\mathrm{Sat}}}}, \tag{5.3}$$

using the previously derived sensitivity (2.16) and assuming the loss factors to be independent of the channels. In a last step, all interferometric phases are referenced to the most sensitive interferometric measurement $i = 1$, $j = Z$, which yields

$$\gamma_{ij} = \left|\gamma_{ij}\right| \mathrm{e}^{\mathrm{j}\frac{B_{\mathrm{ATI},ij}}{B_{\mathrm{ATI},1Z}}\phi} = \left|\gamma_{ij}\right| \mathrm{e}^{\mathrm{j}b_{ij}\phi}, \tag{5.4}$$

where the interferometric phase $\phi = \frac{2\pi}{\lambda} B_{\mathrm{ATI},1Z} L_{\mathrm{d}} L_{\mathrm{g,tot}} \frac{v_{\mathrm{r}}}{v_{\mathrm{Sat}}}$ was introduced and relative baselines $b_{ij}$ are depicted in Fig. 2.2 for $Z = 3$. The estimation variance of the interferometric phase $\phi$ from $N$ independent samples is lower bounded by the CRB [Leho8, pp. 504–505]

$$\sigma_{\mathrm{CRB},Z}^2 = \frac{1}{N I_{\mathrm{F}}^{(Z)}(\phi)}, \tag{5.5}$$

with the Fisher Information being [Leho8, pp. 484–487]

$$I_{\mathrm{F}}^{(Z)}(\phi) = -\mathrm{E}\left[\frac{\partial^2 \ln f(\boldsymbol{u}[n] \mid \phi)}{\partial \phi^2}\right]. \tag{5.6}$$

The double derivative in the Fisher Information evaluates to

$$\begin{aligned}\frac{\partial^2 \ln f(\boldsymbol{u}[n] \mid \phi)}{\partial \phi^2} &= \frac{\partial^2}{\partial \phi^2}\left(-\ln\det(\boldsymbol{C}) - \boldsymbol{u}^{\mathrm{H}}[n]\boldsymbol{C}^{-1}\boldsymbol{u}[n]\right) \\ &= -\frac{\partial}{\partial\phi}\frac{1}{\det(\boldsymbol{C})}\frac{\partial \det(\boldsymbol{C})}{\partial\phi} - \boldsymbol{u}^{\mathrm{H}}[n]\frac{\partial^2 \boldsymbol{C}^{-1}}{\partial\phi^2}\boldsymbol{u}[n] \\ &= -\mathrm{tr}\left\{\boldsymbol{C}^{-1}\frac{\partial^2 \boldsymbol{C}}{\partial\phi^2}\right\} - \mathrm{tr}\left\{\frac{\partial \boldsymbol{C}^{-1}}{\partial\phi}\frac{\partial \boldsymbol{C}}{\partial\phi}\right\} - \boldsymbol{u}^{\mathrm{H}}[n]\frac{\partial^2 \boldsymbol{C}^{-1}}{\partial\phi^2}\boldsymbol{u}[n], \end{aligned} \tag{5.7}$$

where the trace operator $\mathrm{tr}\{\cdot\}$ and the identities [Dhr13, pp. 149–170]

$$\frac{\partial \det(\boldsymbol{C})}{\partial \phi} = \det(\boldsymbol{C}) \,\mathrm{tr}\left\{ \boldsymbol{C}^{-1} \frac{\partial \boldsymbol{C}}{\partial \phi} \right\} \tag{5.8}$$

$$\frac{\partial^2 \det(\boldsymbol{C})}{\partial \phi^2} = \det(\boldsymbol{C}) \left[ \mathrm{tr}\left\{ \boldsymbol{C}^{-1} \frac{\partial^2 \boldsymbol{C}}{\partial \phi^2} \right\} + \mathrm{tr}\left\{ \boldsymbol{C}^{-1} \frac{\partial \boldsymbol{C}}{\partial \phi} \right\}^2 - \mathrm{tr}\left\{ \frac{\partial \boldsymbol{C}^{-1}}{\partial \phi} \frac{\partial \boldsymbol{C}}{\partial \phi} \right\} \right] \tag{5.9}$$

$$\frac{\partial \boldsymbol{C}^{-1}}{\partial \phi} = -\boldsymbol{C}^{-1} \frac{\partial \boldsymbol{C}}{\partial \phi} \boldsymbol{C}^{-1} \tag{5.10}$$

have been used. After applying the expectation operator

$$\begin{aligned} \mathrm{E}\left[ \frac{\partial^2 \ln f\left(\boldsymbol{u}[n] \mid \phi\right)}{\partial \phi^2} \right] &= -\mathrm{tr}\left\{ \boldsymbol{C}^{-1} \frac{\partial^2 \boldsymbol{C}}{\partial \phi^2} \right\} - \mathrm{tr}\left\{ \frac{\partial \boldsymbol{C}^{-1}}{\partial \phi} \frac{\partial \boldsymbol{C}}{\partial \phi} \right\} - \mathrm{E}\left[ \mathrm{tr}\left\{ \frac{\partial^2 \boldsymbol{C}^{-1}(\phi)}{\partial \phi^2} \boldsymbol{u}[n] \boldsymbol{u}^{\mathrm{H}}[n] \right\} \right] \\ &= -\mathrm{tr}\left\{ \boldsymbol{C}^{-1} \frac{\partial^2 \boldsymbol{C}}{\partial \phi^2} + \frac{\partial \boldsymbol{C}^{-1}}{\partial \phi} \frac{\partial \boldsymbol{C}}{\partial \phi} + \frac{\partial^2 \boldsymbol{C}^{-1}}{\partial \phi^2} \boldsymbol{C} \right\} \end{aligned} \tag{5.11}$$

and using the third identity to reformulate the double derivative of the inverse covariance matrix, one finds the Fisher Information for $Z$ channels as

$$I_{\mathrm{F}}^{(Z)}(\phi) = \mathrm{tr}\left\{ \boldsymbol{C}^{-1} \frac{\partial^2 \boldsymbol{C}}{\partial \phi^2} + \frac{\partial \boldsymbol{C}^{-1}}{\partial \phi} \frac{\partial \boldsymbol{C}}{\partial \phi} \right\} - \mathrm{tr}\left\{ \frac{\partial \boldsymbol{C}^{-1}}{\partial \phi} \frac{\partial \boldsymbol{C}}{\partial \phi} + \frac{\partial}{\partial \phi} \left( \frac{\mathrm{d}\boldsymbol{C}}{\mathrm{d}\phi} \boldsymbol{C}^{-1} \right) \right\} \tag{5.12}$$

$$= -\mathrm{tr}\left\{ \frac{\partial \boldsymbol{C}^{-1}}{\partial \phi} \frac{\partial \boldsymbol{C}}{\partial \phi} \right\} = \mathrm{tr}\left\{ \boldsymbol{C}^{-1} \frac{\partial \boldsymbol{C}}{\partial \phi} \boldsymbol{C}^{-1} \frac{\partial \boldsymbol{C}}{\partial \phi} \right\}. \tag{5.13}$$

The former expression is used for analytical derivation of the CRB for 2 and 3 channels and the latter is better suited for numerical calculations.

### 5.1.2 Optimum Bounds of 2- and 3-Channel Interferometry

The CRB for 2-channel interferometry is well known [Tou94], but can also be easily derived using the multi-channel covariance matrix (5.2) and the first expression of the Fisher Information (5.13). Applying this procedure yields the same result as given in the literature [Tou94] and what was used before in (3.7)

$$\sigma^2_{\mathrm{CRB},2} = \frac{1}{2N} \frac{1 - |\gamma_{13}|^2}{|\gamma_{13}|^2}. \tag{5.14}$$

The analytical expression of the CRB for 3-channel interferometry is similarly found from (5.2) and (5.13), where the inverse of the covariance matrix is calculated using Cramer's rule. After many reformulations, one finds its CRB

$$\sigma^2_{\mathrm{CRB},3} = \frac{1}{2N} \frac{1 - |\gamma_{12}|^2 - |\gamma_{23}|^2 - |\gamma_{13}|^2 + 2\mathrm{Re}\left\{ \gamma_{12}\gamma_{23}\gamma_{13}^* \right\}}{b_{12}^2 |\gamma_{12}|^2 + b_{23}^2 |\gamma_{23}|^2 + |\gamma_{13}|^2 - 2(b_{12} + b_{23} - b_{12}b_{23})\mathrm{Re}\left\{ \gamma_{12}\gamma_{23}\gamma_{13}^* \right\}}. \tag{5.15}$$

Fig. 5.2 shows the improvement in terms of relative reduction of the CRB when introducing a third middle channel. The middle channel does not improve the estimation variance in highest

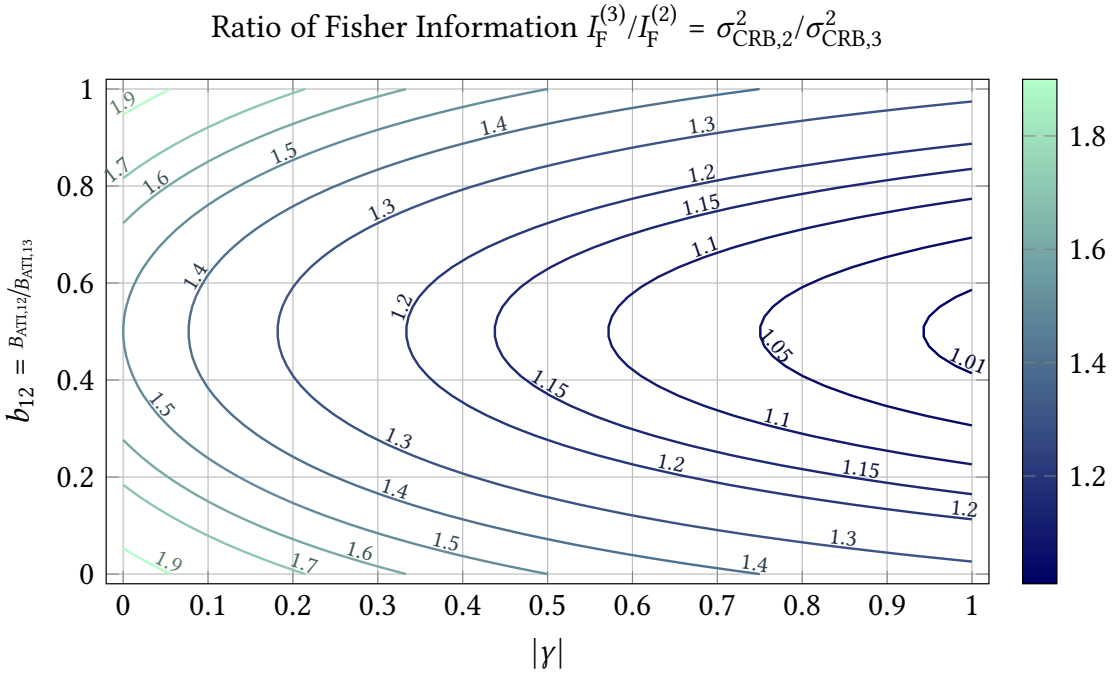


**Fig. 5.2:** Improvement of Fisher Information with middle channel compared to only the outermost channels over position of the middle antenna $b_{23} = 1 - b_{12}$ and coherence, assuming equal coherence between channels $|\gamma| = |\gamma_{12}| = |\gamma_{23}| = |\gamma_{13}|$.

coherence regions and a symmetric positioning $b_{12} = 0.5$. An improvement is observable for decreasing coherence up to a maximum of 2.0, in cases with no coherence and a fully asymmetrical middle antenna positioning ($b_{12} = 0$ or $b_{12} = 1$). From mechanical and structural limitations, the middle antenna that generates this channel, may only be located in a close to symmetrical position. Hence, the improvement in CRB may be negligible. However, all three channels can be used to suppress or completely remove azimuth ambiguities. This capability is analyzed in the following section.

## 5.2 Multi-Channel Harmonic Analysis

### 5.2.1 Algorithm Description

The focused and co-registered one-dimensional azimuth SAR image from $Z$ channels, compare Fig. 5.1, may be modeled as

$$\boldsymbol{u}[n] = \begin{bmatrix} u_1[n] \\ u_1[n] \\ \vdots \\ u_Z[n] \end{bmatrix} = \boldsymbol{u}'[n] + \boldsymbol{\mu}[n]\,, \tag{5.16}$$

where $\boldsymbol{u}'[n] \in \mathbb{C}^{Z\times 1}$ is the coherent signal part and $\boldsymbol{\mu}[n] \in \mathbb{C}^{Z\times 1}$ is the non coherent signal part, mainly due to noise but also scene de-correlation over time [Bam98]. In interferometry, one is interested in

the cross-correlation information between images, which is provided by the coherent signal part. This part does not only consist of the main signal contribution but also the coherent ambiguities. One may express the SAR images

$$\boldsymbol{u}[n] = \sum_{m=-M}^{M} \boldsymbol{h}\left(\phi_m\right)\Gamma_m[n] + \boldsymbol{\mu}[n] = \boldsymbol{H}\left(\phi_{-M}, \phi_{-M+1}, \dots, \phi_M\right)\boldsymbol{\Gamma}[n] + \boldsymbol{\mu}[n] \tag{5.17}$$

with $2M$ coherent ambiguities and a matrix containing the harmonic signatures of their interferometric phases

$$\boldsymbol{H}\left(\phi_{-M}, \phi_{-M+1}, \dots, \phi_M\right) = \begin{bmatrix}\boldsymbol{h}(\phi_{-M}) & \boldsymbol{h}(\phi_{-M+1}) & \dots & \boldsymbol{h}(\phi_M)\end{bmatrix} = \boldsymbol{H}_M \in \mathbb{C}^{Z\times 2M+1}\,. \tag{5.18}$$

The model is restricted to a maximum of $2M$ ambiguities, because the effect of even higher order ambiguities are dominated by the effect of noise, and their biases are neither observable nor distinguishable. A motion of the surface results in a phase change of the coherent signal part for short baselines. For a constant surface velocity during acquisition, the vector

$$\boldsymbol{h}\left(\phi\right) = \begin{bmatrix} 1 \\ \mathrm{e}^{\mathrm{j}\frac{B_{\mathrm{ATI},12}}{B_{\mathrm{ATI},1Z}}\phi} \\ \mathrm{e}^{\mathrm{j}\frac{B_{\mathrm{ATI},13}}{B_{\mathrm{ATI},1Z}}\phi} \\ \vdots \\ \mathrm{e}^{\mathrm{j}\phi} \end{bmatrix} = \begin{bmatrix} 1 \\ \mathrm{e}^{\mathrm{j}\,b_{12}\phi} \\ \mathrm{e}^{\mathrm{j}\,b_{13}\phi} \\ \vdots \\ \mathrm{e}^{\mathrm{j}\phi} \end{bmatrix} \in \mathbb{C}^{Z\times 1} \tag{5.19}$$

shows a Vandermonde structure [Dhr13, p. 56] and the problem formulation shows similarities to direction of arrival estimation with antenna arrays. This description holds in general for stripmap, ScanSAR, TOPS and other scanning modes. However, one must consider, that the matrix $\boldsymbol{H}_M$ might be depending on azimuth position for especially ScanSAR, because this mode images only parts of the Doppler spectrum, which varies with azimuth position [De 06].

The interferometric phases are frequencies of the complex exponential over the temporally separated images. To solve for the interferometric phases, one may apply methods from harmonic analysis, which are highly researched for finding direction of arrivals, i.e. MVDR — also known as Capon's algorithm — [Cap69; Ben05]

$$\hat{\phi}_{\mathrm{MVDR}} = \arg\max_{\phi} \frac{1}{\boldsymbol{h}^{\mathrm{H}}\left(\phi\right)\hat{\boldsymbol{C}}_{\boldsymbol{uu}}^{-1}\boldsymbol{h}\left(\phi\right)}\,, \tag{5.20}$$

where the sample covariance matrix

$$\hat{\boldsymbol{C}}_{\boldsymbol{uu}} = \frac{1}{N_{\mathrm{tot}}}\sum_{i=1}^{N_{\mathrm{tot}}} \boldsymbol{u}[n+i]\boldsymbol{u}^{\mathrm{H}}[n+i] \tag{5.21}$$

is used, or MUSIC [Sch86]

$$\hat{\phi}_{\mathrm{MUSIC}} = \arg\max_{\phi} \frac{1}{\boldsymbol{h}^{\mathrm{H}}\left(\phi\right)\hat{\boldsymbol{U}}_2\hat{\boldsymbol{U}}_2^{\mathrm{H}}\boldsymbol{h}\left(\phi\right)}\,. \tag{5.22}$$

MUSIC requires the singular value decomposition of the sample covariance matrix

$$\hat{\boldsymbol{C}}_{\boldsymbol{uu}} = \begin{bmatrix} \hat{\boldsymbol{U}}_1 & \hat{\boldsymbol{U}}_2 \end{bmatrix} \hat{\boldsymbol{\Sigma}} \hat{\boldsymbol{V}}^{\mathrm{H}}, \tag{5.23}$$

which is introduced in basic vector algebra or statistical signal processing textbooks. The ambiguity removal problem has one major difference, which is the usually wide matrix $\boldsymbol{H}_M$, due to many coherent ambiguities. The precise number of coherent ambiguities depends on the SAR system and geometry, as discussed in Chapters 2 and 3. In direction of arrival estimation, the matrix $\boldsymbol{H}_M$ is tall with $Z > 2M + 1$. Then, the signal sub-space is distinguishable from the noise sub-space and MUSIC may be applied [Sch86]. For a wide matrix $\boldsymbol{H}_M$, there exists no pure noise sub-space. However, from the Karhunen-Loève transform it is known, that eigenvectors of a covariance matrix align with the principal directions of variation of the data samples, where the eigenvector assigned to the largest eigenvalue denotes the direction of highest variance [Hua98]. This eigenvector shows in direction of $\boldsymbol{h}(\phi_0)$, because the main signal usually has the highest power due to damping of ambiguities by the antenna pattern. To apply MUSIC, the signal sub-space is approximated by the eigenvectors of largest eigenvalues and it is assumed that the sub-space spanned by remaining eigenvectors is free of signal. Using this approximation yields a biased estimate, because the signal can not be perfectly reconstructed by the truncated signal sub-space. In the Harmony mission case using three antennas, best results are achieved by a two-dimensional signal sub-space, which reduces the MUSIC algorithm to the method of Pisarenko [Pis73].

MUSIC requires the noise to be non-isotropic and white, here, a noise whitening technique [Bie83; Pau86; Sto97] may be applied while processing real data. For the conducted simulations, noise whitening can be simply achieved by a multiplication

$$\boldsymbol{u}' = \boldsymbol{W}\boldsymbol{u}, \tag{5.24}$$

with the inverse of the known noise covariance matrix

$$\boldsymbol{W} = \mathrm{E}\left[\boldsymbol{\mu}[n]\boldsymbol{\mu}^{\mathrm{H}}[n]\right]^{-1}. \tag{5.25}$$

### 5.2.2 Interferometric Performance with Multiple Channels

The evaluation of the interferometric performance bases on the model configuration as given in Tab. A.1 in the Appendix.

As expected, 3 antennas show a negligibly small improvement in noise averaging compared to the two antenna case, which becomes observable in Fig. 5.3 (c) by comparing the algorithm performance with respect to the CRB for 2 channels. But, 3 channels can be used to reduce the impact of coherent ambiguities. For example, the 95.4%-quantile of velocity error in high signal power scenarios in Fig. 5.3 (a) reduces by a factor of 9.79 at 99 000 samples. For increasing numbers of samples between the targeted 1 km$^2$ to 25 km$^2$ ($10^4$ to $25 \cdot 10^4$ samples), the velocity error does not further decrease with MUSIC and MVDR, but is limited due to residual biases of the estimators. MUSIC and MVDR can only suppress the biases by coherent ambiguities. The estimators are not optimum for removal of coherent ambiguities with multiple channels, because the error is not decreasing with more independent samples. Also, if an ambiguity $m$ contains different power over channels due to different antenna sizes per channel, the suppression capability gets qualitatively reduced. Reason is, that the data model assumes a vector $\boldsymbol{h}\left(\phi\right)$, according to (5.19), with equal power per channel.

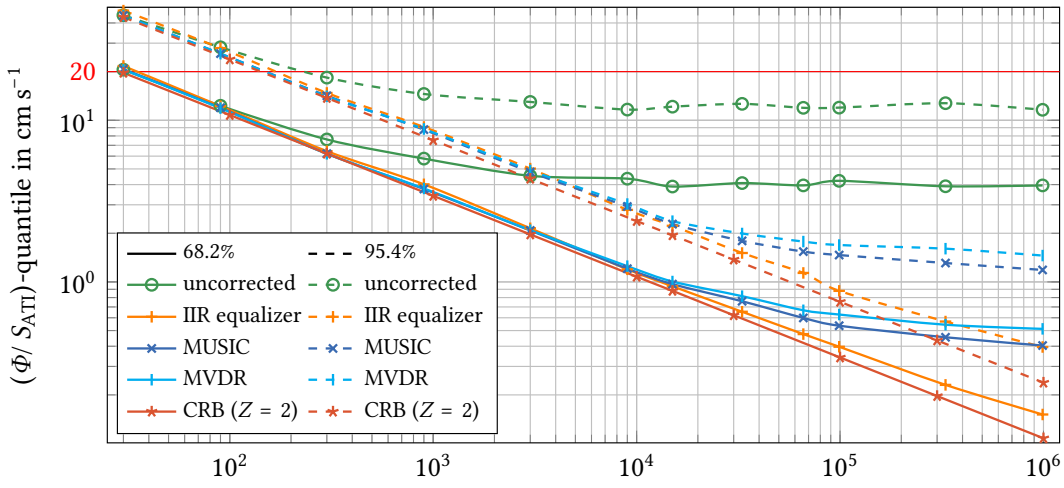


(a) Douglas sea state 6: Wind speed of 15.23 m/s, $\mathrm{E}\left[\sigma^0\right]$ = −5.9 dB

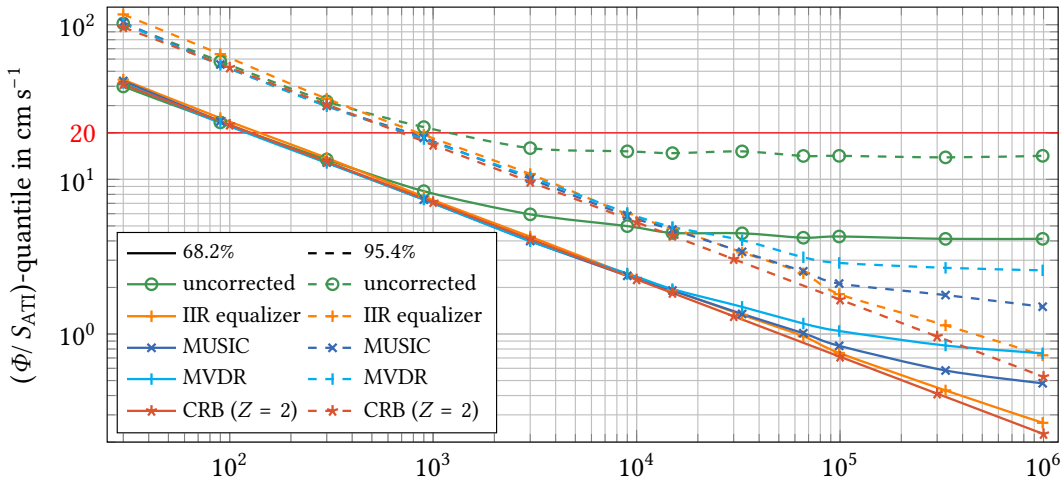


(b) Douglas sea state 5: Wind speed of 10.53 m/s, $\mathrm{E}\left[\sigma^0\right]$ = −11.8 dB

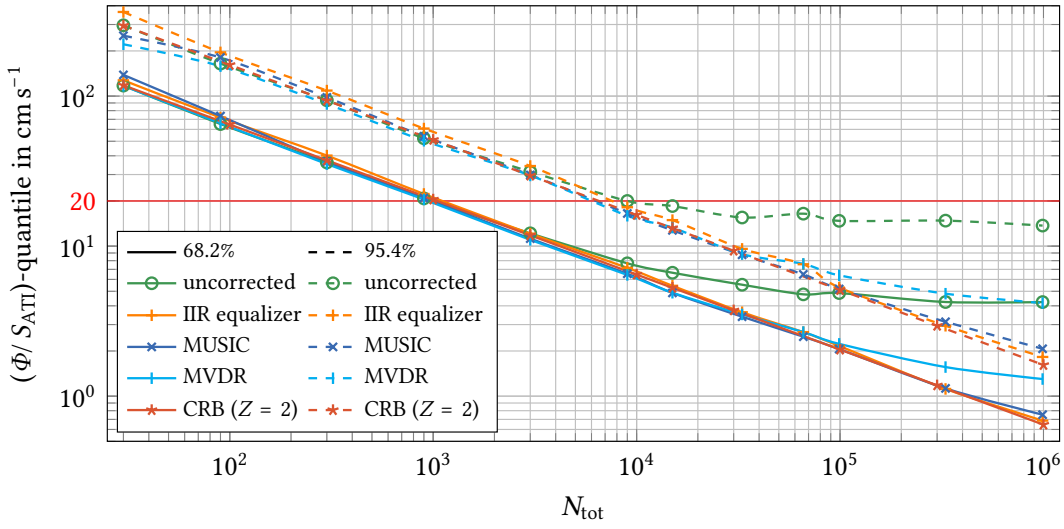


(c) Douglas sea state 2: Wind speed of 3.78 m/s, $\mathrm{E}\left[\sigma^0\right]$ = −19.7 dB

**Fig. 5.3**: Interferometric performance of three channel ATI system and ambiguity removal algorithms over number of samples at a noise level of $\sigma^0_{\mathrm{NE}}$ = −22.0 dB.

**Tab. 5.1**: Improvement of interferometric performance related to the uncorrected interferogram by coherent ambiguity removal with multi-channel algorithms for reference product resolution of Harmony 1.2 km × 1.2 km (15 000 samples)

| Douglas | IIR equalizer | | MUSIC | | MVDR | |
|---|---|---|---|---|---|---|
| sea state | 68.2% | 95.4% | 68.2% | 95.4% | 68.2% | 95.4% |
| 6 | 4.14 | 5.45 | 4.02 | 5.32 | 3.87 | 5.11 |
| 5 | 2.35 | 3.05 | 2.36 | 3.13 | 2.31 | 3.00 |
| 2 | 1.22 | 1.24 | 1.36 | 1.45 | 1.36 | 1.39 |

Tab. 5.1 summarizes the simulated interferometric performance improvement for the reference product resolution, corresponding to 15 000 samples. In sea state 6, the interferometric performance of MUSIC and MVDR is worse than the performance of the IIR equalizer, due to the residual biases. For lower sea states 2 and 5, the performance is comparable or better due to the third channel. To achieve a similar performance improvement using the IIR equalizer in sea states 2 and 5 compared to sea state 6 at reference product resolution, there are 482 798 and 68 989 samples required, respectively. Using the MUSIC algorithm, there are 495 800 and 69 871 samples required, respectively. The improvement may be realized for sea state 5, but for sea state 2, more samples are needed than offered by the maximum product resolution of the Harmony mission. The MVDR algorithm exceeds the maximum number of samples for the Harmony mission to achieve similar improvement, due to increasing residual biases with decreasing SNR.

# 6 Conclusion

## 6.1 Overall Algorithm Comparison

In this work, several techniques for removal of coherent ambiguity biases or estimation of a main signal in noise and coherent ambiguities were derived and their interferometric performance was analyzed. Tab. 6.1 gives a summary on benefits and drawbacks of the investigated algorithms.

Because the IIR equalizer uses the ambiguous positions to estimate the ambiguous signals from its corresponding main signal, the CASR must be known precisely, i.e. effective baseline. Otherwise, biases are introduced from imperfectly removed ambiguities. The (augmented) LMMSE algorithm can tolerate an absolute error, i.e. from an estimation error in the effective baseline. This error will bias the estimate of the ambiguities, but, only the estimate of the main signal is of interest, and ambiguity estimates are discarded. This effect is shown in an associated publication [Ric22].

## 6.2 General Conclusion and Outlook

The effect of coherent azimuth ambiguities limits the achievable interferometric performance, which becomes worse the less azimuth ambiguities are suppressed by the antenna pattern. A complete removal of their systematic error is only achieved by algorithms that consider the biasing effect by coherent ambiguities. Especially, systems with low azimuth ambiguity suppression capabilities or systems with high interferometric performance requirements need those algorithms. The Harmony mission and its ATI mode was exemplarily studied during this work.

The IIR equalizer algorithm achieves the best interferometric performance if the DPCA condition is fulfilled. However, the simulations were performed on frozen scenes without modeling true wave dynamics, which would have resulted in residual biases. The (augmented) LMMSE algorithm circumvents the dependency on scene dynamics and reduces calibration requirements, by disregarding the information on ambiguous positions. It achieves removal of coherent ambiguity biases at a slight loss of interferometric performance, i.e., a factor of 1.61 more samples are required to achieve similar performance on an ocean in sea state 6. To draw a final conclusion on the remaining residual biases due to scene dynamics, ambiguous and main interferometric signals must be analyzed and compared using real data. Also, the (augmented) LMMSE algorithm must be applied to real data to show its feasibility. Further theoretical analysis must be done regarding number, shape and spectral support of window functions, minimum required dynamic of modulated CASR and consideration of correlated samples, and the effect on bias-variance trade-off. For both algorithms, IIR equalizer and (augmented) LMMSE, it is necessary to adaptively choose the number of averaged samples. Instead of the LMMSE combination one may also apply a simpler maximum likelihood (ML) estimator, that does not base on prior interferometric information and hence, is less limited to this knowledge. But, the ML estimator must know the distribution of the interferometric data samples, which has to be estimated as well. The LMMSE estimator needs only a coarse estimate of the sea state and its prior distributions for

**Tab. 6.1:** Summary of coherent ambiguity removal and suppression algorithms

| Algorithm | Channels | Parametrization and calibration | Interferometric performance | Processing requirements |
|---|---|---|---|---|
| IIR equalizer | 2 | Absolute CASR and coherence | ⊖ Requires stationary scene<br>surface acceleration<br>orbital particle motion<br>breaking waves<br>unknown coherence<br>⊖ Susceptible to absolute calibration errors<br>⊕ Removes bias completely | Arithmetic operations |
| (augm.) LMMSE | 2 | Inter-look modulation of CASR and power factors, absolute knowledge of $\sigma^0_{\mathrm{NE}}$ | ⊖ Bias-variance trade-off<br>⊖ No full resolution capability<br>⊖ DC anomaly shifts spectrum<br>⊕ Less susceptible to not fulfilled DPCA condition | One FFT per look<br>Arithmetic operations |
| MUSIC | ≥ 3 | Noise whitening | ⊖ Residual biases<br>⊕ More channels (at low SNR) | Matrix decomposition |
| MVDR | ≥ 3 | - | ⊖ Residual biases, increasing with decreasing SNR<br>⊕ More channels (at low SNR) | Matrix inversion |

implementation, that can be taken from empirical knowledge or the biased measured data.

To evaluate the improvement made with more than two channels, a general equation for the unbiased CRB in ATI was derived. Using the results in the three channel case, it is found, that only asymmetrical antenna placement or low coherence achieve improvements of the CRB, compared to common two-channel interferometry. It remains interesting to find an analytic description of the biased CRB, where more than one coherent signal component — main and ambiguous — is present.

Multiple channels enable the use of harmonic analysis to estimate the main interferometric phase. The implemented MVDR and MUSIC algorithms show similar coherent ambiguity suppression capabilities, while not depending on prior knowledge of scene and system parameters, i.e. CASR or power factors. This makes the algorithms easier to implement, because IIR equalizer and (augmented) LMMSE algorithm require this knowledge, and must cope with their variation over the full swath width. The interferometric performance of MUSIC and MVDR is limited by residual biases. Nonetheless, an improvement of interferometric performance by a factor of 9.79 makes them available for application in the Harmony mission. Further improvements must consider a removal of the residual biases, such that only random errors limit the interferometric performance. To apply the harmonic analysis to real scenarios, an adaptive estimation of the covariance matrix from the non-stationary scene is necessary. A different, but interesting discussion is, how the DCA estimator performs with multiple channels and coherent ambiguities.

The algorithms were tested and evaluated using a simple interferometric SAR data model on a frozen multiplicative noise scene. To project the performance of an algorithm in real scenarios, i.e. dynamic ocean scenes, a sophisticated (forward) model of the ocean dynamics and SAR imaging is required. This will help to identify and improve appropriate techniques and evaluate their performance under defined conditions.

# A Model Parameter Values

**Tab. A.1:** Simulation model parameterization used for interferferometric performance evaluation

| Parameter | Description | Harmony mission Chapter 3 and 5 | Customized Chapter 4 |
|---|---|---|---|
| $R_0$ | slant range | 700 km | 700 km |
| $x_0$ | Harmony-Sentinel separation | 348 km | 260 km |
| $v_{\text{Sat}}$ | satellite velocity | 7600 m/s | 7600 m/s |
| $\phi_{\text{inc}}$ | incidence angle | 40° | 40° |
| $f_{\text{PRF}}$ | pulse repetition frequency | 1.5 kHz | 1.17 kHz |
| $f_{\text{BW}}$ | processed bandwidth | 350 Hz | 700 Hz |
| $\vartheta_{\text{sq}}$ | Harmony squint | 26.43° | 20.38° |
| $L_{\text{d}}$ | Doppler loss factor | 0.8334 | 0.905 |
| $f_0$ | carrier frequency | 5.45 GHz | 5.45 GHz |
| $\Delta_R$ | uncompr. range pulse width | 7475 m | 7475 m |
| $L_{\text{H},1}$ | fore antenna length in azimuth | 4 m | 4 m |
| $L_{\text{H},2}$ | mid. antenna length in azimuth | 2 m | not used |
| $L_{\text{H},3}$ | aft antenna length in azimuth | 4 m | 4 m |
| $B_{\text{ATI},13}$ | physical fore-aft-baseline | 12.16 m | 14.36 m |
| $b_{12}$ | relative middle baseline | 0.5 | not used |
| $\sigma^0_{\text{NE}}$ | noise equivalent sigma nought | −20 dB | −20 dB |
| $P_{\text{Tx}}$ | transmit power | 10 kW | 10 kW |
| $A_{\text{eff}}$ | effective antenna size | $L \cdot 12$ m | $L \cdot 12$ m |
| $\chi$ | oversampling factor | 16 | 16 |

# Bibliography


[Bal16] C. A. Balanis: *Antenna Theory: Analysis and Design*, 4th ed. Hoboken, NJ, USA: John Wiley & Sons, Feb. 2016.

[Bam98] R. Bamler and P. Hartl, "Synthetic aperture radar interferometry", *Inverse Problems*, vol. 14, no. 4, R6–R27, Jan. 1998.

[Bar99] R. Bara, R. Scheiber, and A. Broquetas: "Interferometric SAR signal analysis in the presence of squint", in *IEEE 1999 International Geoscience and Remote Sensing Symposium (IGARSS)*, Hamburg, Germany, Jun. 1999, pp. 257–259.

[Bau14] P. Baudin: *Wireless Transceiver Architecture: Bridging RF and Digital Communications*. Wiley Online Library: John Wiley & Sons, Oct. 2014.

[Bay75] R. W. Bayma and P. A. McInnes: "Aperture size and ambiguity constraints for a synthetic aperture radar", in *IEEE 1975 International Radar Conference (RADAR)*, Arlington, VA, USA, Apr. 1975, pp. 499–504.

[Ben05] J. Benesty, J. Chen, and Y. Huang, "A generalized MVDR spectrum", *IEEE Signal Processing Letters*, vol. 12, no. 12, pp. 827–830, Nov. 2005.

[Bie83] G. Bienvenu and L. Kopp, "Optimality of high resolution array processing using the eigensystem approach", *IEEE Transactions on Acoustics, Speech, and Signal Processing*, vol. 31, no. 5, pp. 1235–1248, Oct. 1983.

[Cal14] D. Calabrese and R. Episcopo: "Derivation of the SAR noise equivalent sigma nought", in *10th European Conference on Synthetic Aperture Radar (EUSAR)*, Berlin, Germany, Jun. 2014, pp. 1–4.

[Cap69] J. Capon, "High-resolution frequency-wavenumber spectrum analysis", *Proceedings of the IEEE*, vol. 57, no. 8, pp. 1408–1418, Aug. 1969.

[Car94] R. E. Carande, "Estimating ocean coherence time using dual-baseline interferometric synthetic aperture radar", *IEEE Transactions on Geoscience and Remote Sensing*, vol. 32, no. 4, pp. 846–854, Jul. 1994.

[Cra11] A. P. Cracknell: *Remote Sensing Applications in Marine Science and Technology*. Dordrecht, The Netherlands: Springer, Dec. 2011.

[Cum05] I. G. Cumming and F. H. Wong: *Digital Processing of Synthetic Aperture Radar Data: Algorithms and Implementation*. Norwood, MA, USA: Artech House, Jan. 2005.

[De 06] F. De Zan and A. Monti Guarnieri, "TOPSAR: Terrain observation by progressive scans", *IEEE Transactions on Geoscience and Remote Sensing*, vol. 44, no. 9, pp. 2352–2360, Aug. 2006.

[Dhr13] P. J. Dhrymes: *Mathematics for Econometrics*, 4th ed. New York, NY, USA: Springer, Sep. 2013.

[Dic91] F. Dickey, M. Labitt, and F. Staudaher, "Development of airborne moving target radar for long range surveillance", *IEEE Transactions on Aerospace and Electronic Systems*, vol. 27, no. 6, pp. 959–972, Nov. 1991.

[Doh10] K. Dohan and N. Maximenko, "Monitoring ocean currents with satellite sensors", *Oceanography*, vol. 23, no. 4, pp. 94–103, Dec. 2010.

[ESA17] ESA European Space Agency. (2017). "Level 2 OCN surface radial velocity (RVL) component", [Online]. Available: https://sentinels.copernicus.eu/web/sentinel/technical-guides/sentinel-1-sar/products-algorithms/level-2/products/surface-radial-velocity-component (visited on 02/28/2022).

[Fre10] O. Frey and E. Meier: "Analyzing tomographic SAR data of a forest with respect to frequency, polarization, and focusing technique", in *2010 IEEE International Geoscience and Remote Sensing Symposium (IGARSS)*, Honolulu, HI, USA, Jul. 2010, pp. 150–153.

[Gab14] B. Gabler, R. Horn, M. Jäger, and A. Reigber: "Accurate antenna characterization for wideband synthetic aperture radar processing", in *German Microwave Conference (GeMiC)*, Aachen, Germany, Mar. 2014, pp. 1–4.

[Gat94] F. Gatelli, A. Monti Guamieri, F. Parizzi, P. Pasquali, C. Prati, and F. Rocca, "The wavenumber shift in SAR interferometry", *IEEE Transactions on Geoscience and Remote Sensing*, vol. 32, no. 4, pp. 855–865, Jul. 1994.

[Gol87] R. M. Goldstein and H. A. Zebker, "Interferometric radar measurement of ocean surface currents", *Nature*, vol. 328, no. 6132, pp. 707–709, Aug. 1987.

[Han01] R. F. Hanssen: *Radar Interferometry: Data Interpretation and Error Analysis*, 2nd ed. Dordrecht, The Netherlands: Kluwer Academic Publishers, Apr. 2001.

[Has85] K. Hasselmann, R. K. Raney, W. J. Plant, W. Alpers, R. A. Shuchman, D. R. Lyzenga, C. L. Rufenach, and M. J. Tucker, "Theory of synthetic aperture radar ocean imaging: A MARSEN view", *Journal of Geophysical Research*, vol. 90, no. C3, pp. 4659–4686, May 1985.

[Hua98] Y. Hua and W. Liu, "Generalized Karhunen-Loeve transform", *IEEE Signal Processing Letters*, vol. 5, no. 6, pp. 141–142, Jun. 1998.

[Jäg14] M. Jäger, B. Gabler, and A. Reigber: "High precision antenna characterisation for broadband synthetic aperture radar processing", in *8th European Conference on Antennas and Propagation (EuCAP)*, The Hague, The Netherlands, Apr. 2014, pp. 3216–3220.

[Jus94] D. Just and R. Bamler, "Phase statistics of interferograms with applications to synthetic aperture radar", *Applied Optics*, vol. 33, no. 20, pp. 4361–4368, Jul. 1994.

[Kri03] G. Krieger and A. Moreira: "Potential of digital beamforming in bi- and multistatic SAR", in *2003 IEEE International Geoscience and Remote Sensing Symposium (IGARSS*, Toulouse, France, Jul. 2003, pp. 527–529.

[Leh08] E. L. Lehmann and J. P. Romano: *Testing Statistical Hypotheses*, 3rd ed. New York, NY, USA: Springer, Aug. 2008.

[Li83] F. K. Li and W. T. K. Johnson, "Ambiguities in spaceborne synthetic aperture radar systems", *IEEE Transactions on Aerospace and Electronic Systems*, vol. AES-19, no. 3, pp. 389–397, May 1983.

[Lig91] L. Lightstone, D. Faubert, and G. Rempel: "Multiple phase centre DPCA for airborne radar", in *Proceedings of the 1991 IEEE National Radar Conference (NRC)*, Los Angeles, CA, USA, Mar. 1991, pp. 36–40.

[Liu19] B. Liu, Y. He, Y. Li, H. Duan, and X. Song, "A new azimuth ambiguity suppression algorithm for surface current measurement in coastal waters and rivers with along-track InSAR", *IEEE Transactions on Geoscience and Remote Sensing*, vol. 57, no. 6, pp. 3148–3165, Dec. 2019.

[Lóp21] P. López-Dekker, B. Chapron, and H. Johnsen: "Observations of sea surface winds and sea surface deformation with the Harmony mission", in *13th European Conference on Synthetic Aperture Radar (EUSAR)*, online, Mar. 2021, pp. 1–4.

[Lóp19a] P. López-Dekker, Y. Li, L. Iannini, P. Prats-Iraola, and M. Rodríquez-Cassola: "On azimuth ambiguities suppression for short-baseline along-track interferometry: The STEREOID case", in *2019 IEEE International Symposium on Geoscience and Remote Sensing (IGARSS)*, Yokohama, Japan, Aug. 2019, pp. 110–113.

[Lóp19b] P. López-Dekker, H. Rott, P. Prats-Iraola, B. Chapron, K. Scipal, and E. D. Witte: "Harmony: An Earth Explorer 10 mission candidate to observe land, ice, and ocean surface dynamics", in *2019 IEEE International Geoscience and Remote Sensing Symposium (IGARSS)*, Yokohama, Japan, Jul. 2019, pp. 8381–8384.

[Mas90] P. Massart, "The tight constant in the Dvoretzky-Kiefer-Wolfowitz inequality", *The Annals of Probability*, vol. 18, no. 3, pp. 1269–1283, Jul. 1990.

[Mon05] A. Monti Guarnieri, "Adaptive removal of azimuth ambiguities in SAR images", *IEEE Transactions on Geoscience and Remote Sensing*, vol. 43, no. 3, pp. 625–633, Feb. 2005.

[Moo79] R. K. Moore, "Tradeoff between picture element dimensions and noncoherent averaging in side-looking airborne radar", *IEEE Transactions on Aerospace and Electronic Systems*, vol. AES-15, no. 5, pp. 697–708, Sep. 1979.

[Mor93] A. Moreira, "Suppressing the azimuth ambiguities in synthetic aperture radar images", *IEEE Transactions on Geoscience and Remote Sensing*, vol. 31, no. 4, pp. 885–895, Jul. 1993.

[Pae20] S. W. Paek, S. Balasubramanian, S. Kim, and O. de Weck, "Small-satellite synthetic aperture radar for continuous global biospheric monitoring: A review", *Remote Sensing*, vol. 12, no. 16, p. 2546, Aug. 2020.

[Pap02] A. Papoulis and S. U. Pillai: *Probability, Random Variables, and Stochastic Processes*, 4th ed. Boston, USA: McGraw-Hill, Dec. 2002.

[Pau86] A. Paulraj and T. Kailath, "Eigenstructure methods for direction of arrival estimation in the presence of unknown noise fields", *IEEE Transactions on Acoustics, Speech, and Signal Processing*, vol. 34, no. 1, pp. 13–20, Feb. 1986.

[Pis73] V. F. Pisarenko, "The retrieval of harmonics from a covariance function", *Geophysical Journal of the Royal Astronomical Society*, vol. 33, no. 3, pp. 347–366, Sep. 1973.

[Por76] L. J. Porcello, N. G. Massey, R. B. Innes, and J. M. Marks, "Speckle reduction in synthetic-aperture radars", *Journal of the Optical Society of America*, vol. 66, no. 11, pp. 1305–1311, Nov. 1976.

[Que86] S. Quegan and J. Lamont, "Ionospheric and tropospheric effects on synthetic aperture radar performance", *International Journal of Remote Sensing*, vol. 7, no. 4, pp. 525–539, May 1986.

[Ran87] R. K. Raney and G. J. Princz, "Reconsideration of azimuth ambiguities in SAR", *IEEE Transactions on Geoscience and Remote Sensing*, vol. GE-25, no. 6, pp. 783–787, Nov. 1987.

[Ric22] D. Richter, M. Rodríquez-Cassola, M. Zonno, and P. Prats-Iraola: "Coherent azimuth ambiguity removal based on linear optimum filtering of short along-track baseline SAR interferograms", in *14th European Conference on Synthetic Aperture Radar (EUSAR)*, Leipzig, Germany, Jul. 2022, submitted.

[Rom14] R. Romeiser, H. Runge, S. Suchandt, R. Kahle, C. Rossi, and P. S. Bell, "Quality assessment of surface current fields from TerraSAR-X and TanDEM-X along-track interferometry and Doppler centroid analysis", *IEEE Transactions on Geoscience and Remote Sensing*, vol. 52, no. 5, pp. 2759–2772, Jul. 2014.

[Rom20] B. Rommen and E. D. Witte: "Report for Assessment: Earth Explorer 10 Candidate Mission Harmony", European Space Agency (ESA), Noordwijk, The Netherlands, Technical Report, version 1.0, Nov. 2020.

[Sch00] R. Scheiber and A. Moreira, "Coregistration of interferometric SAR images using spectral diversity", *IEEE Transactions on Geoscience and Remote Sensing*, vol. 38, no. 5, pp. 2179–2191, Sep. 2000.

[Sch86] R. Schmidt, "Multiple emitter location and signal parameter estimation", *IEEE Transactions on Antennas and Propagation*, vol. 34, no. 3, pp. 276–280, Mar. 1986.

[Sch10] P. J. Schreier and L. L. Scharf: *Statistical Signal Processing of Complex-Valued Data: The Theory of Improper and Noncircular Signals*. Cambridge, MA, USA: Cambridge University Press, Feb. 2010.

[She93] L. Shemer and M. Marom, "Estimates of ocean coherence time by an interferometric SAR", *International Journal of Remote Sensing*, vol. 14, no. 16, pp. 3021–3029, Jul. 1993.

[Sto97] P. Stoica and M. Cedervall, "Detection tests for array processing in unknown correlated noise fields", *IEEE Transactions on Signal Processing*, vol. 45, no. 9, pp. 2351–2362, Sep. 1997.

[Tom78] K. Tomiyasu, "Tutorial review of synthetic-aperture radar with applications to imaging of the ocean surface", *Proceedings of the IEEE*, vol. 66, no. 5, pp. 563–583, May 1978.

[Tor17] R. Torres, S. Lokas, G. Di Cosimo, D. Geudtner, and D. Bibby: "Sentinel-1 evolution: Sentinel-1C and -1D models", in *2017 IEEE International Geoscience and Remote Sensing Symposium (IGARSS)*, Fort Worth, TX, USA, Jul. 2017, pp. 5549–5550.

[Tou94] R. Tough, D. Blacknell, and S. Quegan: "Estimators and distributions in single and multi-look polarimetric and interferometric data", in *Proceedings of 1994 IEEE International Geoscience and Remote Sensing Symposium (IGARSS)*, Pasadena, CA, USA, Aug. 1994, pp. 2176–2178.

[Vac92] P. Vachon and J. West, "Spectral estimation techniques for multilook SAR images of ocean waves", *IEEE Transactions on Geoscience and Remote Sensing*, vol. 30, no. 3, pp. 568–577, May 1992.

[Vel14] D. Velotto, M. Soccorsi, and S. Lehner, "Azimuth ambiguities removal for ship detection using full polarimetric X-band SAR data", *IEEE Transactions on Geoscience and Remote Sensing*, vol. 52, no. 1, pp. 76–88, Jan. 2014.

[Vil12] M. Villano and G. Krieger, "Impact of azimuth ambiguities on interferometric performance", *IEEE Geoscience and Remote Sensing Letters*, vol. 9, no. 5, pp. 896–900, Mar. 2012.

[Wan19] C. Wang, A. Mouche, P. Tandeo, J. E. Stopa, N. Longépé, G. Erhard, R. C. Foster, D. Vandemark, and B. Chapron, "A labelled ocean SAR imagery dataset of ten geophysical phenomena from Sentinel-1 wave mode", *Geoscience Data Journal*, vol. 6, no. 2, pp. 105–115, Jul. 2019.

[War13] K. Ward, R. Tough, and S. Watts: *Sea Clutter: Scattering, the K Distribution and Radar Performance*, 2nd ed. London, UK: Institution of Engineering and Technology, Apr. 2013.

[Wie49] N. Wiener: *Extrapolation, Interpolation and Smoothing of Stationary Time Series*. Cambridge, MA, USA: The MIT Press, Aug. 1949.

[Wol17] S. Wollstadt, P. López-Dekker, F. De Zan, and M. Younis, "Design principles and considerations for spaceborne ATI SAR-based observations of ocean surface velocity vectors", *IEEE Transactions on Geoscience and Remote Sensing*, vol. 55, no. 8, pp. 4500–4519, May 2017.

[Won01] R. Wong: *Asymptotic Approximations of Integrals*. Hong Kong, China: Academic Press, Aug. 2001.

[You03] M. Younis, C. Fischer, and W. Wiesbeck, "Digital beamforming in SAR systems", *IEEE Transactions on Geoscience and Remote Sensing*, vol. 41, no. 7, pp. 1735–1739, Aug. 2003.

[Zon22] M. Zonno, D. Richter, A. T. Prabhakaran, M. Rodríquez-Cassola, A. M. Zurita, J. D. C. Mena, and A. O. Garcia: "Impact of coherent ambiguities on InSAR performance for bistatic SAR missions. The Harmony mission case", in *14th European Conference on Synthetic Aperture Radar (EUSAR)*, Leipzig, Germany, Jul. 2022, submitted.